NUMERICAL INVESTIGATION OF FLOW CONTROL STRATEGIES ON DELTA WINGS

A THESIS SUBMITTED TO
THE GRADUATE SCHOOL OF NATURAL AND APPLIED SCIENCES
OF
MIDDLE EAST TECHNICAL UNIVERSITY

BY

ALPER YILDIRIM

IN PARTIAL FULFILLMENT OF THE REQUIREMENTS
FOR
THE DEGREE OF MASTER OF SCIENCE
IN
MECHANICAL ENGINEERING

SEPTEMBER 2019

Approval of the thesis:

NUMERICAL INVESTIGATION OF FLOW CONTROL STRATEGIES ON DELTA WINGS

submitted by **ALPER YILDIRIM** in partial fulfillment of the requirements for the degree of **Master of Science in Mechanical Engineering Department, Middle East Technical University** by,

Prof. Dr. Halil Kalıpçılar
Dean, Graduate School of **Natural and Applied Sciences** _____

Prof. Dr. M. A. Sahir Arıkan
Head of Department, **Mechanical Engineering** _____

Assoc. Prof. Dr. Cüneyt Sert
Supervisor, **Mechanical Engineering, METU** _____

Assoc. Prof. Dr. M. Metin Yavuz
Co-Supervisor, **Mechanical Engineering, METU** _____

Examining Committee Members:

Prof. Dr. Hakan Tarman
Mechanical Engineering Dept., METU _____

Assoc. Prof. Dr. Cüneyt Sert
Mechanical Engineering, METU _____

Assoc. Prof. Dr. M. Metin Yavuz
Mechanical Engineering Dept. METU _____

Assoc. Prof. Dr. Nilay Sezer Uzol
Aerospace Engineering Dept. METU _____

Assist. Prof. Dr. Onur Baş
Mechanical Engineering Dept., TED University _____

Date: 02.09.2019

I hereby declare that all information in this document has been obtained and presented in accordance with academic rules and ethical conduct. I also declare that, as required by these rules and conduct, I have fully cited and referenced all material and results that are not original to this work.

Name, Surname: Alper Yıldırım

Signature:

ABSTRACT

NUMERICAL INVESTIGATION OF FLOW CONTROL STRATEGIES ON DELTA WINGS

Yıldırım, Alper
Master of Science, Mechanical Engineering
Supervisor: Assoc. Prof. Dr. Cüneyt Sert
Co-Supervisor: Assoc. Prof. Dr. M. Metin Yavuz

September 2019, 108 pages

The use of Unmanned Aerial Vehicles (UAV), Unmanned Combat Aerial Vehicles (UCAV) and Micro Aerial Vehicles (MAV) have been increasing in recent years. The researchers aim to understand the complex flow structure around low sweep angle delta wings, which are frequently used in such vehicles.They are also interested in controlling the flight performance of these vehicles by various active and passive means. This study involves numerical simulations of flows around a delta wing with a sweep angle of 45^{o}at high angles of attack. Passive bleeding, which is a method based on the idea of transferring momentum from the pressure side of the flow to the suctions side by allowing air to pass through the bleed holes, is used as a flow control technique. Various bleed hole configurations are studied and the effects of the dimensions, locations and orientations of the holes on the flow fields are examined. Four design alternatives are proposed and tested at attack angles of 16°, 17° and 18° and Reynolds number of 75000. Results show that the performance of the passive bleeding method is highly affected by the geometrical parameters of the holes. It is seen that the newly proposed idea of using yaw angle, i.e. positioning the holes not parallel to the leading edge but with an angle, gives promising results. With appropriate bleeding hole sizing and positioning, it is observed that three-dimensional

flow separation is delayed and suction pressure is increased even at high angles of attack by the regeneration of vortical structures.

Keywords: Non-slender Delta Wing, Passive Flow Control, Bleeding, CFD

ÖZ

DELTA KANATLARINDA AKIŞ KONTROL STRATEJİLERİNİN SAYISAL İNCELENMESİ

Yıldırım, Alper
Yüksek Lisans, Makina Mühendisliği
Tez Danışmanı: Doç. Dr. Cüneyt Sert
Ortak Tez Danışmanı: Doç. Dr. M. Metin Yavuz

Eylül 2019, 108 sayfa

İnsansız Hava Araçları (UAV), İnsansız Muharebe Hava Araçları (UCAV) ve Mikro Hava Araçları (MAV)'nın kullanımı son yıllarda giderek artmaktadır. Araştırmacılar bu tarz araçlarda sıklıkla kullanılan ince olmayan delta kanatların etrafındaki karmaşık akış yapısını anlamayı amaçlamaktadır. Ayrıca, bu araçların uçuş performansını çeşitli aktif ve pasif yöntemlerle kontrol etmeyi hedeflemektedirler. Bu çalışma, 45 derece ok açısına sahip delta kanat etrafındaki akışın yüksek saldırı açılarındaki sayısal simulasyonlarını incelemektedir. Akış kontrol yöntemi olarak delikler vasıtası ile havanın kanadın basınç tarafından emiş tarafına doğru aktarılmasına izin vererek kanadın emiş tarafındaki akışa momentum aktarılması fikrine dayanan pasif akıtma yöntemi kullanılmıştır. Çeşitli akıtma deliği konfigürasyonları incelenmiş ve deliklerin boyutlarının, konumlarının ve yönlerinin akış alanı üzerindeki etkileri incelenmiştir. Dört tasarım alternatifi önerilmiş ve 16°, 17° ve 18° hücum açılarında ve Reynolds sayısı 75000'de incelenmiştir. Sonuçlar, pasif akıtma metodunun performansının, akıtma deliklerinin geometrik parametrelerinden yüksek ölçüde etkilendiğini göstermektedir. Yeni önerilen sapma açısının yani akıtma deliklerinin hücum kenarına paralel konumlandırılması yerine açılı konumlandırılmasının umut verici sonuçlar verdiği görülmüştür. Uygun akıtma deliği boyutu ve düzeninde, üç

boyutlu akış ayrılmasının geciktirildiği ve girdaplı yapıların yeniden oluşturulmasıyla emme basıncının yüksek hücum açılarında dahi yükseldiği gözlemlenmiştir

Anahtar Kelimeler: Düşük ok açılı delta kanatlar, Pasif akış kontrolü, Pasif akıtma, HAD

To my family

ACKNOWLEDGEMENTS

I would like to express my endless thanks and pay my respects to my Thesis Advisor Assoc. Prof. Dr. Cüneyt Sert for his guidance, support and selflessly help and to my Co-Supervisor Assoc. Prof. Dr. Mehmet Metin Yavuz for his valuable contributions, support and guidance.

I would like to express my gratitude and respect to my dear professor and colleague Prof. Dr. Nurten Vardar - who showed me the pleasure of doing research, broadened my horizon in my view of life and my profession, taught me the professional ethics and how to be a good person, and whose support and guidance I felt at any moment - for the opportunities, support and guidance she has provided me and I would like to express my honor to be a colleague with her.

I would like to thank my darling Damla Gürkök for her eternal love, trust and support. She is the one who beats the big drum and loves me wholeheartedly in every moment and every aspect of my life as well as her great patience, care and love during my graduate education and the writing process of this thesis. I know that she will keep supporting and loving me in the future as one of the most valuable people in my life, who puts my priorities before her own.

I would like to thank E. Karaismail, U. Ay, K. Peneklioğlu and my other colleagues with the necessary tolerance and guidance and also like to thank Figes Inc. and Numesys Inc.

Last but not least, I would like to thank my family, to my father Alparslan Yıldırım, to my mother N. Mukadder Yıldırım, to my aunt E. Müyesser Yavuz, to my uncle Y. Ahmet Yavuz, to my grandmother Meskure Yavuz, to my late grandfather Muhittin Yavuz and to all the family members whom I cannot mention here, who has given me eternal love and support throughout my life, for their everlasting trust and support.

TABLE OF CONTENTS

ABSTRACT v

ÖZ vii

ACKNOWLEDGEMENTS x

TABLE OF CONTENTS xi

LIST OF TABLES xiii

LIST OF FIGURES xiv

LIST OF ABBREVIATIONS xviii

LIST OF SYMBOLS xix

CHAPTERS

1. INTRODUCTION 1

1.1. The Motivation and Aim of the Study 11

1.2. Structure of the Thesis 12

2. LITERATURE SURVEY 15

2.1. Numerical Studies 15

2.2. Flow Control Techniques on Delta Wings 19

2.2.1. Active Flow Control 19

2.2.2. Passive Flow Control 23

3. SIMULATION MODEL 27

3.1. Geometrical Model 27

3.1.1. The Base Wing 27

3.1.2. Bleeding Wing used in Validation 28

3.1.3. Extra Bleeding Wings 29

3.2. Simulation Domain and Boundary Conditions 33
3.3. Simulation Parameters and Solver Settings 36
3.4. Mesh Generation 40
3.5. Mesh Independence Study 44
3.5.1. Mesh Independence for the Base Wing 44
3.5.2. Mesh Independence for the Bleeding Wing 51
4. VALIDATION STUDY 57
4.1. Comparison of the Base Wing Results 58
4.2. Comparison of the Bleeding Wing Results 60
4.3. Sensitivity of the Results 63
5. RESULTS OF NEW BLEED HOLE DESIGNS 67
5.1. Design-1: 5 Bleed Holes Delta Wing with 5.5° Yaw Angle 73
5.2. Design 2: 5 Bleed Holes with Variable Back Angle and 5.5° Yaw Angle 76
5.3. Design 3: Full Open Bleed Hole 81
5.4. Design 4: Full Open Bleed Hole with 5.5° Yaw Angle 84
5.5. Overview of All Designs 88
6. CONCLUSION 97
6.1. Summary and Conclusion 97
6.2. Future Work 99
REFERENCES 101

LIST OF TABLES

TABLES

Table 3-1. Boundary Conditions Details.....36
Table 3-2. Methods and Discretization Schemes Used.....37
Table 3-3. Details of the Boundary Layer Mesh.....43
Table 3-4. Meshes Used for the Base Wing (All sizes are in mm).....44
Table 3-5. Meshes Used for the Bleeding Wing (All sizes are in mm).....52
Table 5-1. Designs to be Tested.....68
Table 5-2. min/max $-C_p$ Values.....93
Table 5-3. Comparison of drag/lift forces of all designs 95

LIST OF FIGURES

FIGURES

Figure 1-1. Basic Geometric Characteristics of Delta Wings 2
Figure 1-2. Flow Structure Around a Typical Delta Wing [3] 3
Figure 1-3. Schematic Streamline Patterns for (a) Reattachment Over Non-Slender Wings and (b) with No Reattachment on Wing Surface on Slender 4
Figure 1-4. Variation of Root Mean Square Swirl Velocity Across the Vortex Core [11] 5
Figure 1-5. Illustration of Suction Effect of Vortex Structure 5
Figure 1-6. Illustration of Vortex Lift Contribution to Lift Coefficient According to Polhamus Vortex Lift Theory [12] 6
Figure 1-7. Illustration of Vortex Lift Contribution to Lift Coefficient for Different Sweep Angles[1] 7
Figure 1-8. Regions of a Shear Layer [16] 8
Figure 1-9. PIV Measurement Results of Shear Layer Sub-structures for a 38.7° Swept Delta Wing [15] 8
Figure 1-10. Illustration of Vortex Breakdown and Shear Layer Instabilities [18] ... 10
Figure 2-1. Effectiveness Comparison of Steady and Unsteady Blowing [2] 21
Figure 2-2. Comparison of Near-surface Streamline Patterns with Crossflow Topology for Trailing-edge Blowing at Values of Momentum Coefficients C_μ=0.4 and 1.63 at the Planes of Interest x/C=0.34 and 0.8 [89] 22
Figure 3-1. Dimensions of the Base Wing 28
Figure 3-2. Illustration of Bleeding Wing Dimensions used in the Validation Study [19] 29
Figure 3-3. Fully Open Bleeding Wing 30
Figure 3-4. Definition of Angle Ω 31

Figure 3-5. Modified versions of Five Hole and Fully Open Configurations Using $\Omega = 5.5°$ 31
Figure 3-6. Bleeding Wing with Gradually Changing Back Angles and $\Omega = 5.5°$ ...32
Figure 3-7. Dimensions of Flow Domain with Half Wing Inside.....34
Figure 3-8. Boundary Conditions.....35
Figure 3-9. Locations of Monitoring Points used for Convergence Check 38
Figure 3-10. Residuals and Convergence Monitors.....39
Figure 3-11. a) Tetrahedral Mesh b) Hybrid Hexahedral-Polyhedral Mesh c) All Polyhedral Mesh.....41
Figure 3-12. Refinement Regions used to Control Mesh Density 42
Figure 3-13. Boundary Mesh Examples at Different Locations a) Mesh Aroun the Leading Edge b) Mesh inside a Bleeding Hole.....43
Figure 3-14. Pressure Measurement Lines.....45
Figure 3-15. Negative Pressure Coefficient on the Upper Surface at x/C=0.3 (top), x/C=0.5 (middle), x/C=0.7 (bottom) ontained by Different Meshes 46
Figure 3-16. Shear Stress Lines at the Upper Surface Obtained by Different Meshes 47
Figure 3-17. Streamlines on Two Different Planes Parallel to the Upper Surface. Top two rows: 1mm, Bottom two rows: 3 mm Away from the Surface 48
Figure 3-18. u Velocity Contour on the Plane 3 mm Away from Top Surface. Gray Color Shows Negative u Zones.....49
Figure 3-19. Base Wing Drag Force Comparison with Relative Errors 50
Figure 3-20. Base Wing Lift Force Comparison with Relative Errors 50
Figure 3-21. Negative Pressure Coefficient on the Upper Surface of the Bleeding Wing at x/C=0.3 (top), x/C=0.5 (middle), x/C=0.7 (bottom) 53
Figure 3-22. Streamlines on two Different Planes Parallel to the Upper Surface of the Bleeding Wing. Top row: 1mm, Bottom row: 3 mm Away from the Surface 54
Figure 3-23. u Velocity Contour on the Plane 3 mm Away from Top Surface. Gray Color Shows Negative u Zones.....54
Figure 3-24. Bleeding Wing Drag Force Comparison with Relative Errors.....55

Figure 3-25. Bleeding Wing Lift Force Comparison with Relative Error 55
Figure 4-1. Comparison of Streamlines 3 mm Away from the Top Surface of the Base Wing at $\alpha = 18°$ 58
Figure 4-2. Comparison of Cross Plane Streamlines and Velocity Vectors for the Base Wing at $\alpha = 18°$ 59
Figure 4-3. Pressure Coefficient Comparison for the Base Wing at $\alpha = 18°$ 60
Figure 4-4. Comparison of Streamlines 3 mm Away from the Top Surface of the Bleeding Wing at $\alpha = 18°$ 61
Figure 4-5. Comparison of Cross Plane Streamlines and Velocity Vectors for the Bleeding Wing at $\alpha = 18°$ 61
Figure 4-6. Pressure Coefficient Comparison for the Base Wing at $\alpha = 18°$ 62
Figure 4-7. Pressure Coefficient Comparison for the Base Wing at $\alpha = 6°$ 63
Figure 4-8. Streamlines 0.5, 2 and 4 mm Away from the Top Surface of the Bleeding Wing at $\alpha = 17°$ 64
Figure 4-9. Streamlines 3 mm Away from the Top Surface of the Bleeding Wing at Different Angle of Attacks 65
Figure 4-10. Pressure Coefficient Comparison for the Bleeding Wing at $\alpha = 6°, 17°$ and $18°$ 66
Figure 5-1. Streamlines on the Plane 3 mm Away from Top Surface at $\alpha = 16°, 17°$ and $\alpha = 18°$ 69
Figure 5-2. Comparison of Cross Plane Streamlines for the Base Wing and RBW at $\alpha = 16°, 17°$ and $\alpha = 18°$ 70
Figure 5-3. -u Zone Contour on the Plane 3 mm Away from Top Surfacen of Base Wing and RBW. Gray Color Shows Negative u Zones 71
Figure 5-4. Pressure Coefficient Distributions of the Base Wing and RBW 72
Figure 5-5. Streamlines, Velocity Vectors and -u Zone on the Plane 3 mm Away from Top Surface of Design 1 74
Figure 5-6. Cross Plane Streamlines and Velocity Vectors for Design 1 75
Figure 5-7. Pressure Coefficient Distribution at Half Chord of Design 1 76

Figure 5-8. Streamlines, Velocity Vectors and -u Zone on the Plane 3 mm Away from Top Surface of Design 2 78
Figure 5-9. Cross Plane Streamlines and Velocity Vectors for Design 2 79
Figure 5-10. Pressure Coefficient Distribution at Half Chord of Design 2 80
Figure 5-11. Streamlines, Velocity Vectors and -u Zone on the Plane 3 mm Away from Top Surface of Design 3.....82
Figure 5-12. Cross Plane Streamlines and Velocity Vectors for Design 3 83
Figure 5-13. Pressure Coefficient Distribution at Half Chord of Design 3 84
Figure 5-14. Streamlines, Velocity Vectors and -u Zone on the Plane 3 mm Away from Top Surface of Design 4.....86
Figure 5-15. Cross Plane Streamlines and Velocity Vectors for Design 4 87
Figure 5-16. Pressure Coefficient Distribution at Half Chord of Design 4 88
Figure 5-17. Pressure Coefficient Distribution on Wing Surface 90
Figure 5-18. Comparison of $-C_p$ Distribution of All Designs 92
Figure 5-19. Comparison of 3D Streamlines 96

LIST OF ABBREVIATIONS

CFD	Computational fluid dynamics
AoA	Angle of attack
RANS	Reynolds-averaged Navier–Stokes
DES	Detached eddy simulation
SST	Shear stress transport
CC	Curvature correction
PIV	Particle image velocimetry

LIST OF SYMBOLS

Greek Symbols

α	Angle of attack
θ	Back angle
Ω	Yaw angle
Λ	Sweep angle
ρ	Fluid density

Latin Symbols

C	Chord length
C_p	Pressure coefficient
C_d	Drag coefficient
C_l	Lift Coeffcient
p	Surface pressure
p_∞	Free stream pressure
U_∞	Free stream velocity
Re	Reynolds number
u	Streamwise velocity
F	Force
A	Base wing suction surface area

CHAPTER 1

INTRODUCTION

Delta (triangular) shaped wing forms have attracted the attention of researchers from past to present. Delta wings, which date back to the beginning of aviation history, continue to be an area of interest today. The main reason for this interest is their useful features such as stability at high angles of attack, wide range of uses spreading from low subsonic to supersonic speeds and high manoeuvrability. Delta wings are used in both civil aviation and military. It is a very preferred wing form, especially in combat aircrafts. Today, Unmanned Air Vehicles (UAV), Mini-Micro Air Vehicles (MAV) and Unmanned Combat Air Vehicles (UCAV) have been added to the field of usage. Research and development activities are also increasing with the increase in the areas where delta wings are used.

Figure 1-1 shows the basic geometric characteristics of delta wings including chord length, span width, sweep angle, bevel angle and thickness. Chord length is the distance between the apex of the wing and the trailing edge. The bevel angle is the angle of the surface connecting the wing's leading edge and the pressure side. The thickness of the wing is the distance between the pressure side and the top side. Sweep angle is the angle between the lateral axis and the leading edge. Span of the wing is defined as the length of the trailing edge. Delta wings can be classified in different ways according to their geometric features. The main classification is made according to the sweep angle of the wing. Wings with a sweep angle greater than 55 degrees are called slender or low-swept. Those with sweep angle between 35 and 55 degrees are called non-slender or high-swept. There are many studies on slender delta wings in the literature. The studies date back to the 1960s [1]. The main reason for this is that slender delta wings have been used frequently in military aircraft from past to present.

On the other hand, studies on non-slender wings have been increasing in recent years. The number of flow control studies on non-slender wings is extremely low.

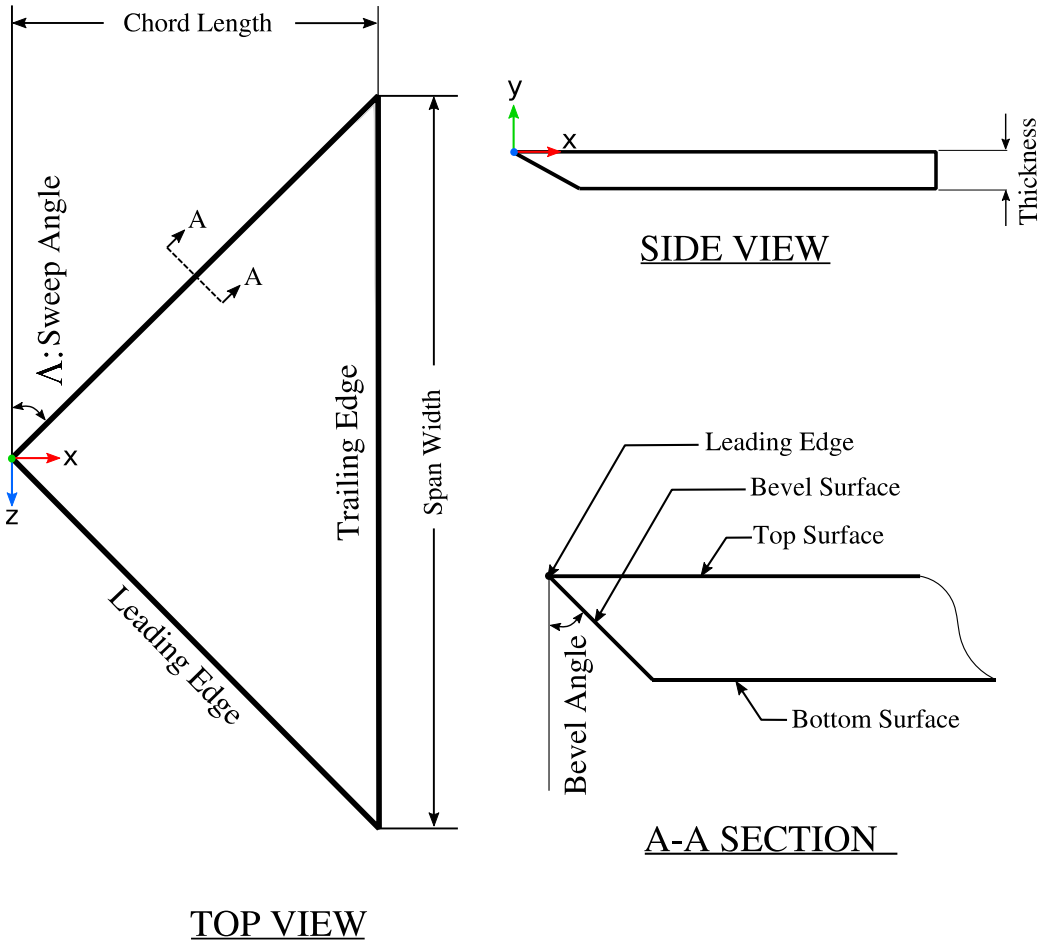

Figure 1-1. Basic Geometric Characteristics of Delta Wings

In Figure 1-2, the flow structure around a typical delta wing is illustrated. The main characteristic is that the flow separated from the leading edge creates counter-rotating vortices on the top surface [2]. In some cases, this vortex reattaches to the top surface at some point, and this may result in the formation of a secondary vortex. As a matter

of fact, new vortices can also be formed by each vortex reattaching to the wing's surface.

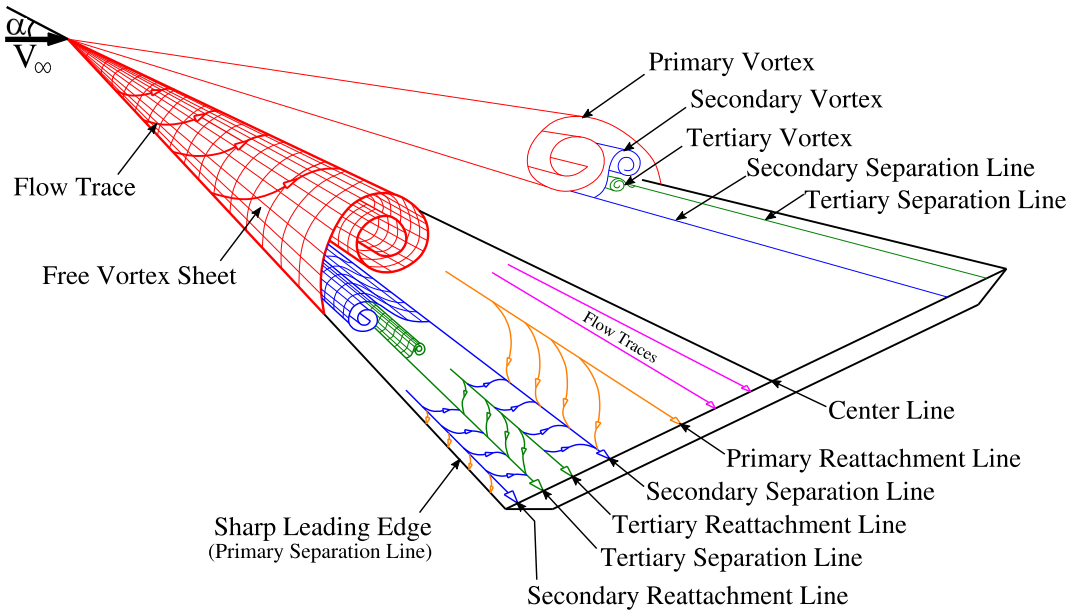

Figure 1-2. Flow Structure Around a Typical Delta Wing [3]

When the flow around non-slender delta wings and slender delta wings are compared, it is observed that the vortices are formed closer to the wing surface in non-slender wings. Studies have shown that the separated flow in slender wings reattaches to the upper surface only at very low angles of attack, which is visualized in Figure 1-3. Therefore, the interaction of vortices formed on non-slender delta wings with the boundary layer on the upper surface of the wing is much higher. The reattachment does not occur on the wing (on the platform) on slender wings, or if it does, it occurs on the symmetry line, which is the most extreme point on which it can occur. It is extremely difficult to control the reattachment for slender wings [4]. However, the separated flow in the non-slender delta wings reattaches onto the wing before reaching the symmetry line. According to Taylor and Gursul [4], reattachment line shifts

towards symmetry line along with the increasing of the angle of attack. Sheer layer's reattachment is the most important source of buffeting for non-slender delta wings [5,6]. Additionally, the increase in the interaction between the primary vortex approaching the surface and the boundary layer on the wing's surface causes a second vortex, called the second primary vortex, to rotate in the same direction. Dual vortex structure is observed only at low angles of attack and low Reynolds numbers, but not in slender delta wings [7–10].

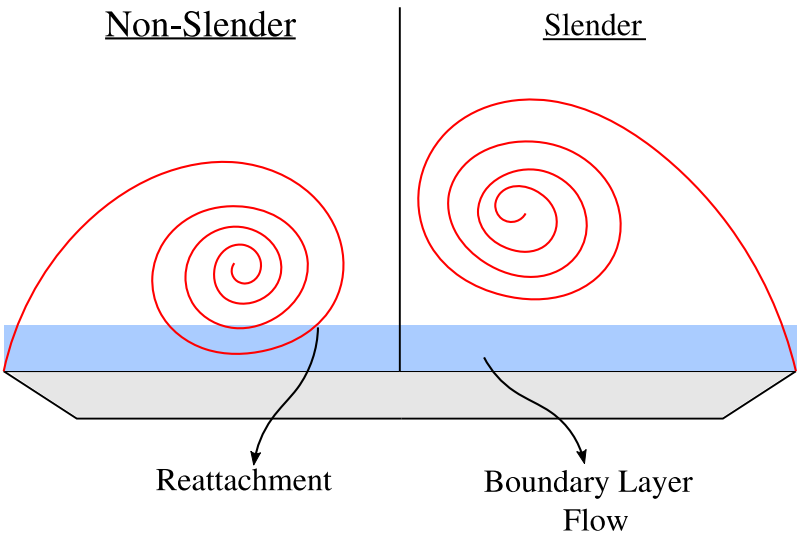

Figure 1-3. Schematic Streamline Patterns for (a) Reattachment Over Non-Slender Wings and (b) with No Reattachment on Wing Surface on Slender

The core velocity of these vortices on the top of the wing can reach up to 3 or even 5 times of the free stream velocity [4], as demonstrated in Figure 1-4. According to Bernoulli's principle, the velocity increase in the vortex core means that the pressure decreases in the same region. The low-pressure vortex core formed in the upper region of the wing creates a suction zone, increasing the lift force of generated by the wing (see Figure 1-5). Due to this low-pressure area on the wing, the upper side of the wing is called the suction side.

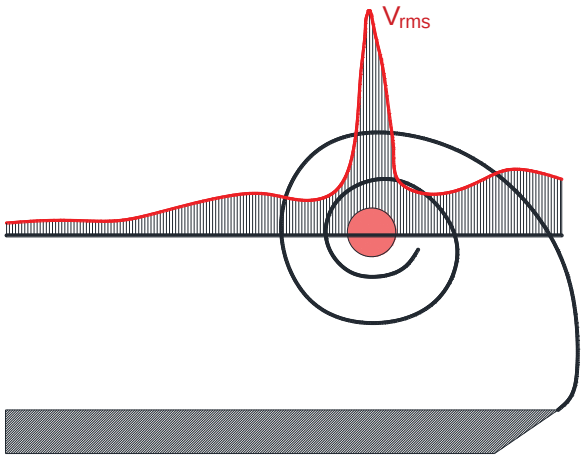

Figure 1-4. Variation of Root Mean Square Swirl Velocity Across the Vortex Core [11]

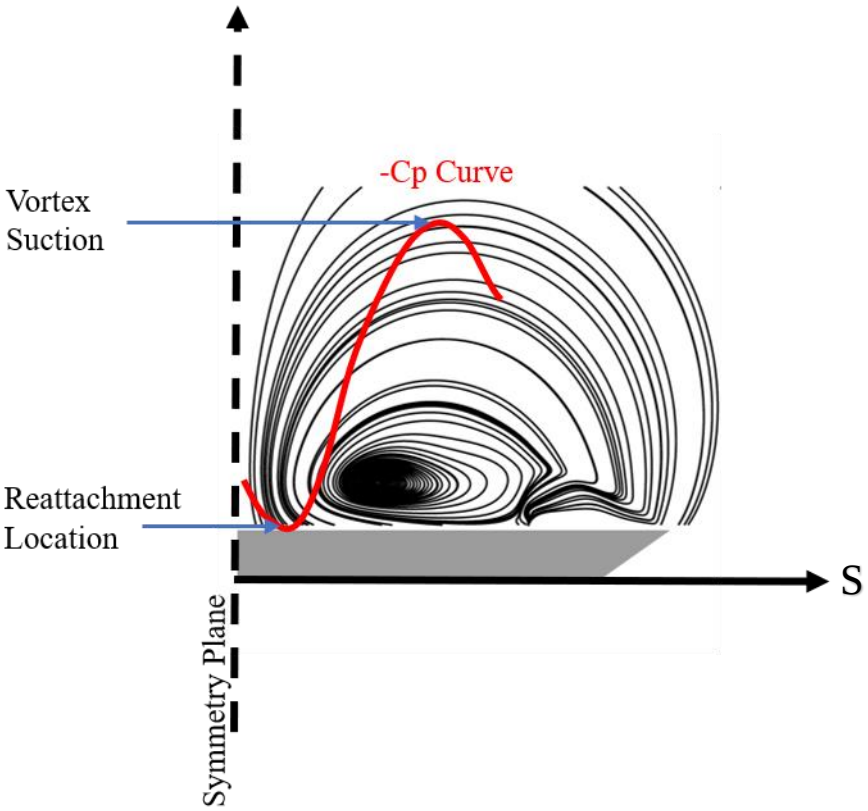

Figure 1-5. Illustration of Suction Effect of Vortex Structure

Polhamus [12] examined the contribution of the vortical structure to the lifting force in high swept wings. Figure 1-6 shows this contribution for a 75° wing. Figure 1-7 shows the variation of lift coefficient due to vortex lift with the attack angle for wings with different sweep angles. The effect of high-velocity vortices on the lift force increases as the sweep angle of the wing increases. Therefore, the lift force, that stems from the vortex flow structure, is a proportionately smaller portion of the total lift force for non-slender delta wings.

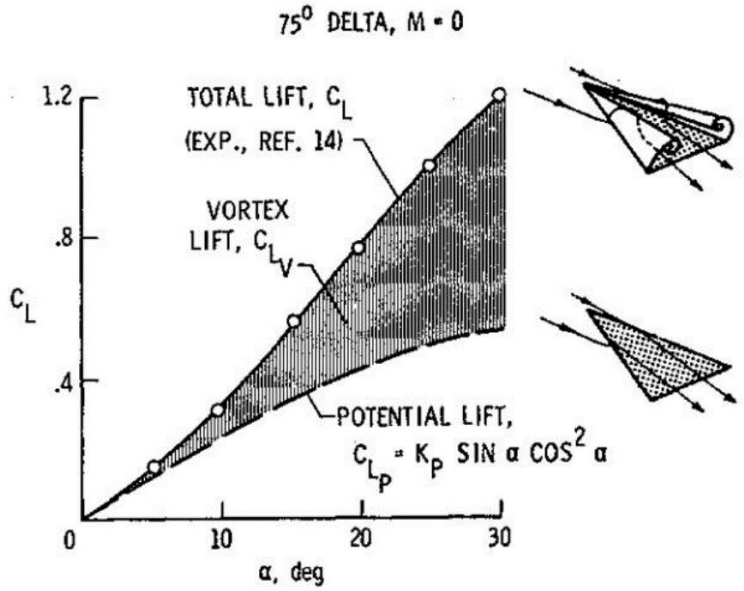

Figure 1-6. Illustration of Vortex Lift Contribution to Lift Coefficient According to Polhamus Vortex Lift Theory [12]

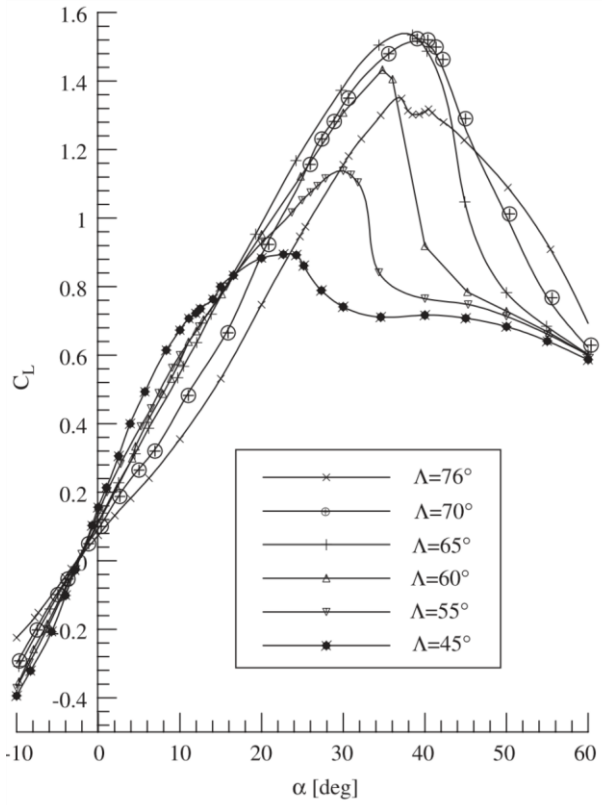

Figure 1-7. Illustration of Vortex Lift Contribution to Lift Coefficient for Different Sweep Angles[1]

Depending on the shape of the wing and the flight condition, different flow structures may occur around the wing. One of the structures is shear layers that separate from the leading edge to form different regions known as the free shear layer, rotational core, and viscous sub-core as shown in Figure 1-8. Yanıktepe and Rockwell [8] categorized the vortex stream as large scale and small scale and instabilities are related to small scale patterns. These small-scale patterns, in other words small vortices, are caused due to the Kelvin-Helmholtz instability. Similar findings have also been observed in other studies [13,14]. Yavuz et al. [15] studied the sub-structures formed on the shear layer using the PIV flow visualization method, results of which can be seen in Figure 1-9. This instability causes the vortex core to wander around the mean location, known as vortex wandering.

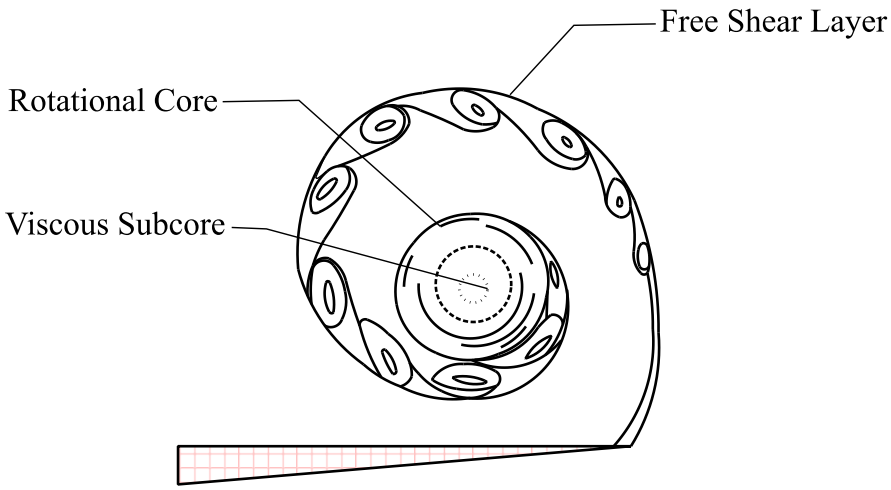

Figure 1-8. Regions of a Shear Layer [16]

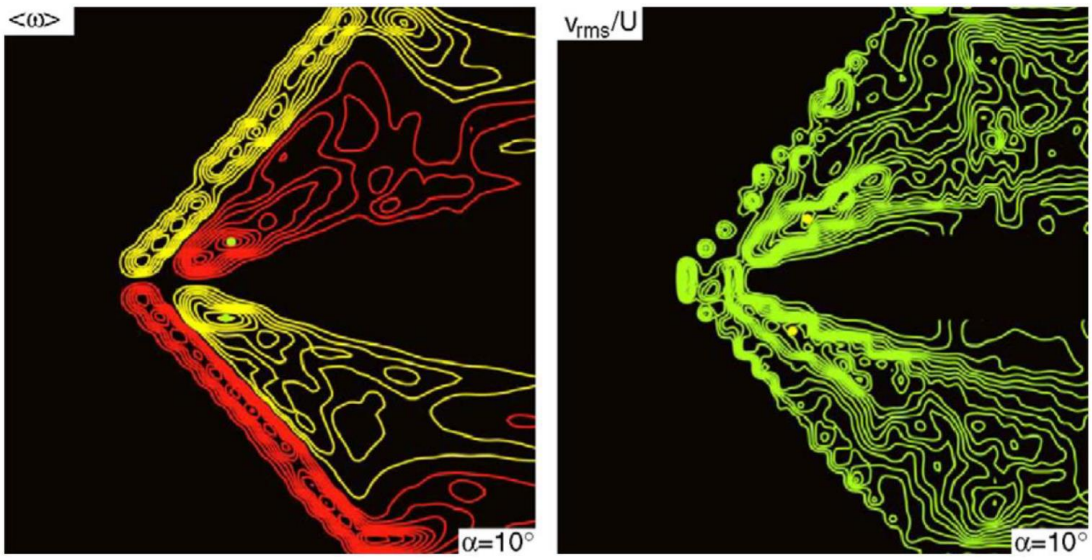

Figure 1-9. PIV Measurement Results of Shear Layer Sub-structures for a 38.7° Swept Delta Wing [15]

The flow structure around delta wings varies according to the wing features and flight conditions. Changes in flight conditions can cause different instabilities such as vortex breakdown, shear layer instabilities and helical mode instabilities, and other undesirable formations in the flow structure may be observed. These unstable conditions are mostly observed with an increase in the angle of attack [1]. Vortex breakdown and shear layer instabilities are visualized in Figure 1-10. As the angle of attack increases, the instabilities observed around the wing vary according to the shape of the wing. In slender delta wings, vortex breakdown is observed as the angle of attack increases. The location of the vortex breakdown has a direct impact on the wing performance. At high angles of attack, changes in the location of the vortex breakdown result in a sudden drop of the lift force. Vortex breakdown is one of the main reasons for stalling in slender wings [17]. On the other hand, in non-slender delta wings, the stability of the wing is determined by the reattachment of the flow separated from the leading edge to the wing's surface. Research has shown that the reattachment of the shear layer is one of the main causes of high-velocity fluctuations for non-slender wings. The main reason for this is the higher level of vortex-boundary layer interaction in non-slender wings. In non-slender wings, the location of vortex breakdown gets closer to the apex as the angle of attack increases. Furthermore, the reattachment line advances towards the central line. The greatest difference between the flow structures around non-slender and slender delta wings is observed at this point. High-velocity fluctuations are observed along the reattachment line, not at the location of the vortex breakdown. Therefore, reattachment is the main cause of buffeting for non-slender delta wings [6].

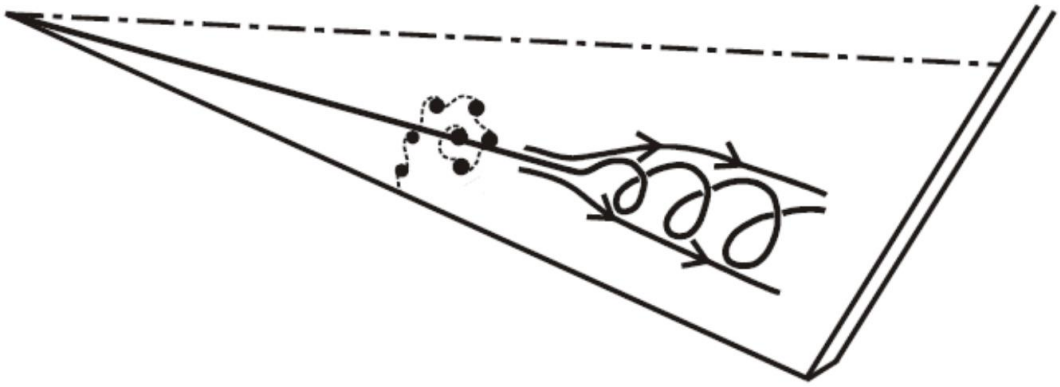

Figure 1-10. Illustration of Vortex Breakdown and Shear Layer Instabilities [18]

The stability of vortices formed around a delta wing is directly effective in its performance and is vital to wing stability. Standard delta wings do not have high stability performance. Therefore, they often require the application of flow control techniques. Vortex breakdown for slender delta wings can be prevented or delayed by flow control strategies. Since a significant part of the lift force in slender delta wings is provided by the vortex formed by separating from the leading edge, delaying of the vortex breakdown allows ascending to high angles of attack without entering the stall regime. Whereas in non-slender delta wings, vortex breakdown is seen starting from low angles of attack. Furthermore, the control of vortex breakdown is not a top priority for non-slender delta wings due to the low contribution of vortex-induced lift to the total lift. With flow control strategies in non-slender wings, controlling separation from the leading edge and strengthening of the reattachment are attempted. In non-slender wings, the main condition that creates instability is the reattachment of the separated shear layer. Therefore, flow control studies are concentrated in this field [19].

The need for wings that are able to ascend to high angles of attack requires the application of flow control mechanisms on the wings. This requirement has led many researchers to lean in this direction. In literature, there are many studies examining active and passive flow control methods applied to delta wing platforms. The most

common of these methods are: geometric modifications [20–24] (e.g. changes in wing shape or parts added to the wing), material modifications [25] (e.g. using materials with different surface roughness or flexibility), blowing or suction [26,27] (e.g. blowing or sucking steady or unsteady air through the holes drilled on the surface of the wing), heating the wing's surface [28]. Some of these methods are active methods, which require extra energy to be applied, or passive methods, which do not require energy for the application of the flow control mechanism. Although the effect of passive flow control mechanisms is generally lower than active ones, they are preferred methods because of their ease of application. Although the most common passive flow control mechanisms are geometric and material modifications, the bleeding method is also encountered in the recently conducted studies. In this thesis, the application of bleeding as a passive flow control method, which is becoming increasingly common, is studied.

1.1. The Motivation and Aim of the Study

While predominantly slender type delta wings have been used in the past, it is seen that non-slender delta wings have started to be used in platforms such as MAV, UCAV and UAV, which are increasingly becoming popular nowadays. Therefore, studies on non-slender wings are smaller in number compared to the ones on slender wings. Cruising radius anxiety in unmanned aerial vehicles and the need to be used in different flight conditions have made it important to control the flow around the wing using flow control methods. Passive control methods are particularly preferred in such platforms.

The current study is the continuation of a series of earlier passive control of flow over delta wing studies performed at METU Mechanical Engineering Department. Çelik et al. [19] conducted a study on the application of the passive bleeding on non-slender wings. He opened bleeding holes in different orientations on a 45-degree sweep angle delta wing and investigated the effects of bleeding on the flow structure experimentally. Karagöz [18] experimentally examined the hole configurations that

Çelik did not examine at different Reynolds numbers. Kestel [29] examined the effect of the bleeding opening ratio on the flow around the low swept delta wings and reported the drag and lift forces for various configurations. The main motivation of this study is to take these earlier studies a step further by studying the performance of different bleed hole configurations, including novel ones, numerically.

The aim of this study is to control the flow around a non-slender delta wing with passive bleeding flow control method It is aimed to investigate the effects of different bleeding hole configurations on the flow by numerical simulations. The effects of different bleeding hole locations and sizes are investigated at Reynolds number 75000 and angle of attack 16°, 17° and 18°. Calculations are carried out using ANSYS Fluent software under the conditions of the wind tunnel used by Karagöz [18]. By examining the studies of Karagöz and Çelik [19], possible changes that can be made in the bleeding holes and that can improve the flow structure are evaluated, and the determined configurations are simulated.

1.2. Structure of the Thesis

This thesis consists of six main chapters in total. Chapter 1 provides brief information about delta wings and flow features observed over them, describes the position of the delta wings in the aviation industry, discusses the challenges of using delta wings and provides the motivation and aim of the study.

In chapter 2, the literature survey including the fundamentals of flow structure around delta wings, mainly non-slender delta wings are given. The focus of the chapter in on the use of passive flow control strategies.

The geometric details of the used wing, numerical details of all simulations performed throughout the study and mesh independence study for the base wing and bleeding wings are shared in Chapter 3.

In Chapter 4, results of the validation simulations performed are compared with the experimental results of Karagöz [18] and Çelik [19].

In Chapter 5, results of the new bleeding hole configurations are presented.

The thesis ends with conclusions and potential future study ideas given in Chapter 6.

CHAPTER 2

LITERATURE SURVEY

Delta wings are the preferred wing types in many aviation applications with their ability to reach high speeds and produce high lifting force. Despite the advantages of delta wings, the complexity of the flow around them increases the number and variety of studies to be conducted. Studies in the literature go back to the wing designed by Alexander Lippisch in 1931, the first successful use of the delta wing [30]. Today's studies are customized according to the geometric characteristics of the wing and flight conditions. When we examine the delta wings according to their shapes, they are divided into two main groups as slender and non-slender. There are many more studies in the literature for high swept delta wings compared to low swept ones that are considered in the current study. This chapter summarizes the related literature in two steps; the first one focusing on the numerical aspects and the second one focusing on the flow control aspect.

2.1. Numerical Studies

In the process of improving aerodynamic performance around the wings, researchers need to understand the flow physics and work on a large number of design alternatives. Today, the Computational Fluid Dynamics (CFD) is considered to be an important complement to experimental studies and plays an important role in the development of modern high-performance aircraft. CFD, which has been developing since the mid-sixties, has demonstrated its ability to model vortex flows with Euler and Navier-Stokes equations.

Until recently, vortical flows studies were generally limited to steady-state simulations due to the limited computational power. In the first studies in this field, Euler equations had been used predominantly. Eriksson and Rizzi [31] have pioneered the

use of numerical simulations in this field by using the three-dimensional compressible Euler equations to model a delta wing with 70° sweep angle under subsonic and transonic conditions. In the simulations performed at Mach number 0.9 and 1.5, 18,000 grid points are used and the vortical flow structure separated from the sharp leading edge can be observed. Eriksson and Rizzi continued their studies in this field by examining the wings under different conditions [32–34]. In another study [35], they compared the simulation they did using 76.800 grid elements with the results of the potential boundary-integral (Panel) method. This study is the first proof that the vortical structure around the wing can be captured numerically with an acceptable accuracy level. However, they interpreted the change at about 80% of the chord length as "unexpected vortex generation". In the following years, it was understood that this situation is a "vortex breakdown" [35,36].

In this field, the first studies using Navier-Stokes equations include the study of Fuji [37], in which a case at $\mathrm{Re} = 0.9 \times 10^6$ is simulated using laminar flow assumption. In addition to the primary vortex, a secondary vortex was also captured, and the results were consistent with the experiments. The frequency of unsteady studies has increased as we approached today [4,38–41].

Turbulence model used is one of the most important differences in the numerical studies seen in the literature. To capture the vortical structure and the instabilities generated around the delta wing, the selected turbulence model is of great importance. In his study examining VFE-2 wing, Cummings [42] carried out examinations using RANS (Reynolds-averaged Navier–Stokes), DES (Detached Eddy Simulation) and DDES (Delayed Detached Eddy Simulation) models. He pointed out that although the RANS models are sufficient to resolve the flow field correctly, the DES model should be used to obtain more detailed information about the flow around the wing and to understand the flow character. Vlahastergios [43] carried out examinations on vortex breakdown with URANS (Unsteady RANS) and Reynolds-Stress models. He also made simulations with the half and full wing model and reported that the solutions made with the half wing and the solutions with the full wing gave very similar results.

Lan [44] used the Spalart-Allmaras turbulence model and compared the vortex core axial velocities in slender and non-slender wings. The vortex core velocities in non-slender wings were higher than those in slender wings. Cooper [45] conducted simulations at low Reynolds numbers, focusing on modeling challenges of vortex breakdown, which is turbulent whereas the flow around the wing is close to being laminar. He worked with RANS and PANS (Partially-averaged Navier Stokes) models. Schiavetta [46] examined the vortex flow around the delta wings numerically and focused on unsteady effects. In his study, he made comparisons between DES and URANS models and found that low-frequency instabilities generated around the delta wing could be captured with both URANS and DES models with sufficient accuracy. However, he concluded that DES model is more successful in calculating high-frequency vortex instabilities. It is understood that RANS models can be used if the instability occurs at a low frequency. In his thesis, Görtz [47] examined the flow around the delta wings on a wider scale. The main findings of his study include the following: vortex breakdown has an inviscid structure and its location can be calculated the same by using Euler or Navier-Stokes equations; vortical flows, especially vortex breakdown, are highly sensitive to grid resolution; vortex breakdown is a problem that must be solved as unsteady; DES has high accuracy but requires considerable computational power. Mitchell et al. [48] used DES and RANS-LES models in their studies and reported that RANS-LES models can accurately solve sub-structures in the flow, but also reported that LES (Large Eddy Simulation) requires significantly dense grid by nature when compared to DES. On the other hand, Küçükyılmaz [49] focused on vortex breakdown phenomenon in his study and performed comparisons between different RANS turbulence models. In his study, he demonstrated that the k-ω SST with Curvature Correction turbulence model is able to capture the vortical structure around the wing in the most accurate manner. Sayılır [50] also made a comparison between RANS turbulence models for VFE-2 wing and obtained results parallel to Küçükyılmaz's results.

Many researchers use CFD to better understand the physics of the flow around delta wings and to simulate conditions that are costly to examine experimentally. In this context, numerous studies have been conducted to better understand the effect of wing shape [20,24,51–53], the effect of Reynolds number [54], the effects of maneuvering and landing/take off [55,56], flow characteristics [55–60] and the effects of experimental setups on results [61].

CFD, by its very nature, has several challenges in governing equation complexity, turbulence and transition modeling, flow field asymmetry, grid generation and numerical dissipation [62]. Some of these challenges in the flow around delta wings are:

- Finding the right turbulence model for the cases under consideration. Studies conducted [41,45,49,50,63–65] show that turbulence models cannot capture all flow structures and case-specific turbulence models need to be identified. This increases the workload and makes it necessary to support the numerical study with experimental studies. In addition, the effects of artificial viscosity and numerical dissipation in the models used should be taken into consideration, especially for cases where flow separation is intense [62].
- Geometric scale of model, compressibility and unsteady effects (such as asymmetry in the flow and oscillations) need to be addressed [62].
- Obtaining surface pressure values accurately is the most challenging situation in delta wing flow simulations. Especially RANS turbulence models are insufficient at this point. In many studies in the literature, it is seen that C_p curves do not match with experimental results. Son [41] performed simulations using DES and RANS models and found that RANS models could not capture surface pressure gradients with sufficient accuracy, but more accurate results could be obtained with DES. In studies conducted with advanced turbulence models such as DES and LES, the similarity with the experiments is found to be higher than the RANS models [63,66–68].

2.2. Flow Control Techniques on Delta Wings

Structures that constitute the main characteristics of the flow around the delta wing are also the source of the wing's instability in extreme flight conditions. Delaying of the vortex breakdown, control of separation and reattachment are the main objectives of flow control to improve and keep the wing's performance stable. In this context, the wing can be kept away from unstable situations with active or passive techniques to be applied to the wing. Active flow control methods that are encountered in this field are blowing or suction, low or high-frequency excitations, pneumatic or hydraulically controlled flaps, surface morphing and plasma actuators. The major passive flow control methods are geometry modifications or material modifications. Gursul et al. [2] summarized active and passive flow control techniques on delta wings in their studies. In addition, according to the geometric character of the wing, the desired instability to be controlled in the flow structure also changes. For slender delta wings, the priority is to control the vortex breakdown, while for non-slender wings it is desirable to control the reattachment. In his recent work, Gursul [69] focused on the topic of flow control of tip/edge vortices. In a broad framework, he described the physics of flow around the wings in detail, then touched on active and passive flow control techniques. In the remainder of the chapter, flow control studies in the literature will be examined under two main titles as active and passive.

2.2.1. Active Flow Control

Active flow control is very popular in the field of aviation and therefore there are many studies on it in the literature.

The most common active flow controls are the techniques that control the flow by suction or blowing. The basis of this method is to add momentum to the flow or extract it. Blowing or suction can be performed from different parts of the wing; the separation can be controlled by blowing or suction from the leading edge [70–75], blowing or suction from the trailing edge [76–78], blowing or suction from wing's surface according to wing's shape and vortex core location [79–82]. All these operations can

be performed as unsteady or steady. Unsteady blowing suction is known to be more effective than steady blowing suction [2]. Figure 2-1 shows a comparison of unsteady and steady blowing suction effectiveness where C_μ is momentum coefficient and ΔC_N is the difference of normal force coefficient of controlled and uncontrolled cases. It is seen that unsteady blowing has a great potential for active flow control. Wood et al. [71] were able to control the vortex structure on wings with a sweep angle of 60° up to an angle of attack $\alpha = 50^\circ$ using steady blowing method. In their numerical study, Vlahostergios [83] and Kyriakou [84] achieved a considerable delay in the vortex breakdown location by jet flap application on the trailing edge. Vlahostergion used an in-house developed CFD code in his study, while Kyriakou used the commercial software Fluent. In studies for unsteady blowing and suction [70,85–87], periodic suction and blowing application from the leading edge for slender wings improved the lift force by delaying the formation of vortex breakdown and delayed the transition to the stall regime. Buzica [65], on the other hand, studied the flow control with the leading-edge blowing method numerically at a high angle of attack of 45° using the Detached Eddy Simulation method. He worked with fine meshes like 66M cell and compared his simulations with wind tunnel tests. With the DES model, he was able to capture surface pressure distribution very precisely. According to Gursul's study [2], the most effective blowing technique is the along-the-core technique. Using this technique, Küçükyılmaz [49] examined the effect of pitch angle and momentum coefficient on vortex breakdown location in a 70° swept wing and found that high momentum coefficient causes a big delay in the vortex breakdown location. Küçükyılmaz performed his simulations with k-ω SST with Curvature Correction turbulence model using ANSYS Fluent software.

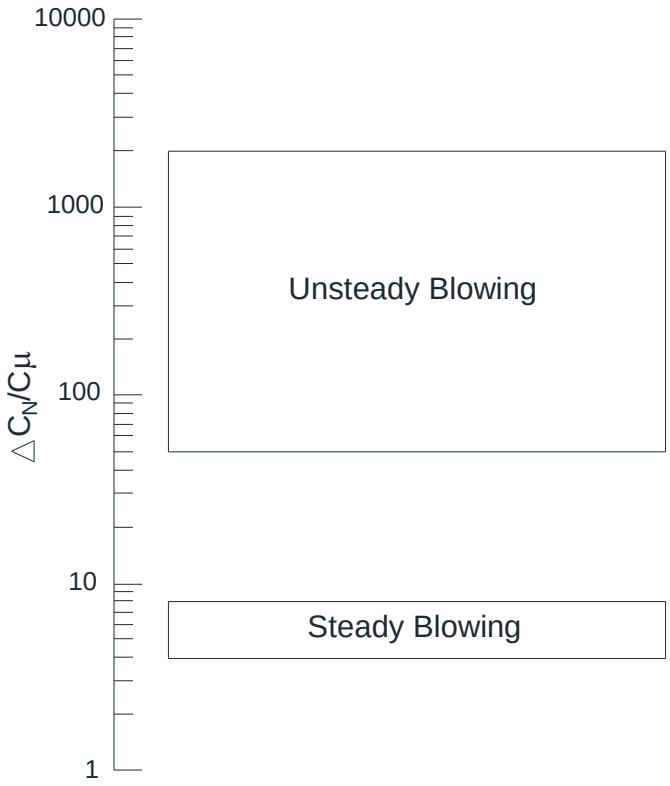

Figure 2-1. Effectiveness Comparison of Steady and Unsteady Blowing [2]

In non-slender wings, suction and blowing applications are less in number compared to slender wings. Yavuz and Rockwell [77] applied the steady trailing edge blowing method on a wing with a sweep angle of 35° and examined the effects of this application on the near surface. Zharfa [88] used a similar wing and reported that steady blowing is an effective method for the control of three-dimensional separation. In another study, Yavuz and Rockwell [89] examined the effects of trailing edge blowing for a wing with a 35° sweep angle and observed that an increase in the blowing coefficient caused a reduction in the overall spatial extent of the pattern of normal velocity fluctuations. Figure 2-2 taken from this study, clearly shows the differences, between the wings on which blowing is and isn't applied. The flow around

the wing is controlled by this method and reverse flow formation on the wing is prevented to a high degree.

Another active flow control method is the use of actuators. Sibilski [90], in his study, examined the aerial vehicles with delta wings experimentally and controlled the symmetrically formed vortices with micro actuators causing the symmetry to be distorted. Distortions in flow symmetry changed the moment balance on the wing and provided flow control. In a similar study, flow control by plasma actuators placed on the wing bevel surface was examined by Shen [91].

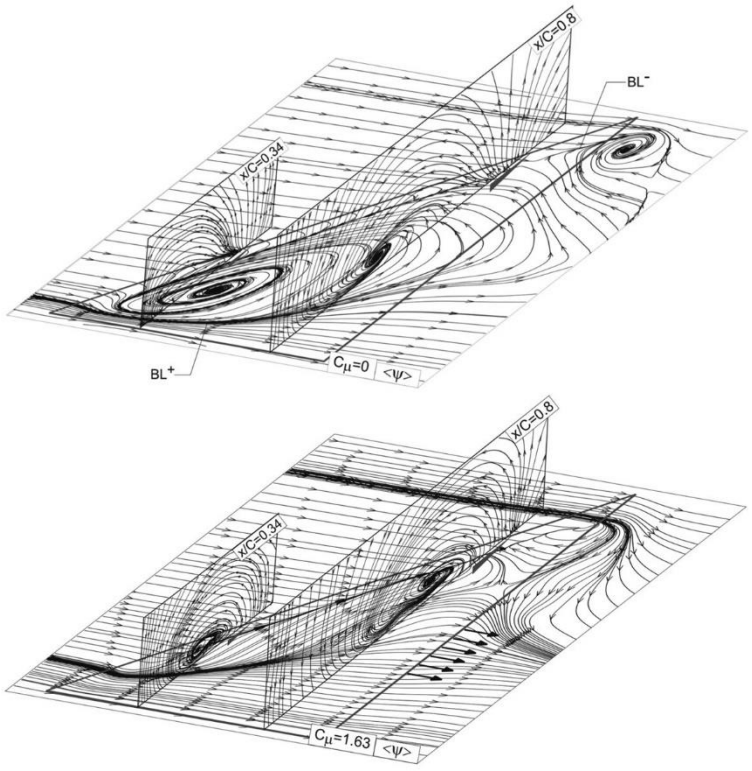

Figure 2-2. Comparison of Near-surface Streamline Patterns with Crossflow Topology for Trailing-edge Blowing at Values of Momentum Coefficients C_μ=0.4 and 1.63 at the Planes of Interest x/C=0.34 and 0.8 [89]

2.2.2. Passive Flow Control

The passive flow control method is easier to apply and hence has a wider range of applications because it does not require energy and is also inexpensive to implement. The basis of this method is geometric and material modifications. Although it has smaller effects than active flow control, it can sometimes cause unexpected improvements too.

Passive flow control methods applied differ according to the shape of the wing. Apex flaps, leading edge or trailing edge flaps [92–94] and leading or trailing edge modifications [20–22] are applicable to control vortex breakdown for slender wings. Apex flaps provided the greatest benefit among these applications. Tormalm [95], in his study, examined numerically the swept Lambda wing and performed a detailed study with adjustable flaps at different angles placed on the trailing edge. He used RANS turbulence model in his study and obtained results parallel with experimental studies. Hitzel [96] also studied a similar wing in his study numerically with RANS turbulence models in the transonic regimen. There are many other studies [97–99] in this field in the literature.

On the other hand, the primary objective in non-slender wings is to control the reattachment. In this context, researchers have shown that the use of a flexible wing improves reattachment and provides control of leading edge separation [25,93,100].

In addition to these methods, the bleeding method, which has become more popular in recent years, is one of the effective passive flow control methods to control flow on non-slender wings. The basis of the method is the holes drilled on the wing using the pressure difference between the pressure side and the top side of the wing. The air passing through these holes contributes to the development of reattachment by changing the flow structure on the top side of the wing. With this feature, it is a good alternative to the blowing method that uses energy. The bleeding method can be used as both a passive and an active method. Flow control can be performed simultaneously by actively opening and closing the holes. The first use of the method was realized by

Lechmann [101] in the 1920s and he applied the method on slotted wings and ailerons . Hunter et al. [102] examined the application of passive porosity on a fighter aircraft numerically and demonstrated that the method is applicable in this field. Carpenter and Porter [103], in their theoretical studies, have shown that passive porosity is an effective method for controlling boundary-layer instability. In the study on two-dimensional VR-7 airfoil, it was observed that the bleeding method contributed to the forces and moments on the wing [104]. In the light of these studies, Çelik [19] investigated the effect of different orientation bleeding holes on the flow structure around a non-slender delta wing with a sweep angle of 45°. In order to define the hole orientation, he defined the Back angle and Edge Angle and examined the effect of these angles on the flow experimentally. In these examinations, he observed that the bleeding method re-formed the vortical structure that disappeared with increasing angle of attack, and in all cases that he examined, the reattachment line shifted outward from the wing's symmetry line. Karagöz [18] based her study on Çelik's and investigated experimentally the effect of the change in the back angle on the wing with a 45^o sweep angle at different Reynolds numbers. In his study, in addition to surface pressure measurement, he also visualized the flow on the upper surface of the wing using the PIV method. The experimental matrix included the angle of attack varying in the range of 13° to 23°, the Reynolds numbers at $3{,}5x10^4$, $7{,}5x10^4$ and $12{,}5x10^4$, and the back angle values of 13^o,18^o and 23^o. As a result of her study, she found that bleeding method re-established the vortical structure and increased suction pressure at high angles of attack (i.e. α = 16, 17, 18). On the other hand, bleeding holes cause a decrease in suction pressure and have no advantage at higher angles of attack (i.e. α=19) compared to relatively low angles (i.e. α=13). Similar studies [105,106] in this field also clearly demonstrate the effect and potential of the bleeding method on non-slender wings.

Although the bleeding method is mostly applied in non-slender wings, application examples are also seen in slender wings. Sayılır [50], in his study, examined the effect of bleeding holes numerically on VFE-2 delta wing with a 65^o sweep angle. In his

study, he found that the most effective turbulence model is k-ω SST with Curvature Correction and performed the simulations using ANSYS Fluent software. In his examination, he found that bleeding flow control application provided little improvement in the lifting force and breakdown delay of the wing. This study demonstrates that the bleeding method has greater potential in non-slender wings than in slender wings. Kestel [29] [29] examined the effect of bleeding opening ratio, i.e. ratio of the total hole area to the wing's original upper surface area. He reported that the wing with the maximum bleeding opening ratio was able to reattach the flow up to an angle of attack of 20^{o}, but the lift force was low compared to the wings with lower opening ratio. Although the wing with the maximum opening ratio has a lower lift force compared to the other wings, it was shown that it is the wing that delayed the entry to the stall regime the best.

CHAPTER 3

SIMULATION MODEL

This chapter consists of five sections, which provide details of the

- geometrical model
- simulation domain and boundary conditions
- simulation parameters
- mesh generation process
- mesh independence study.

3.1. Geometrical Model

The wings used in this study can be divided into two main groups. The first is called the 'base wing', which has no bleed holes. The second group is called 'bleeding wings', which contain bleed holes to provide passive flow control. Several different bleed hole configurations will be used, resulting in multiple bleeding wings. The base wing and one of the bleeding wings used in Karagöz's experiments [18] will be used for validation purposes, and these are the wings that are introduced in the coming two sections. Then the details of the extra bleed configurations introduced in this thesis will be given.

3.1.1. The Base Wing

Figure 3-1 shows the geometric dimensions of the base wing, as taken from Karagöz's thesis [18]. Considering the geometry and the flow field to be symmetric with respect to the wing centerline, only half of the wing is considered in the simulations. The length of the chord (C) is 135 mm. Sweep angle (Λ) is 45^{o}, making the span width to be twice of the chord length. The wing thickness (t) is 8 mm and the bevel angle is 45°.

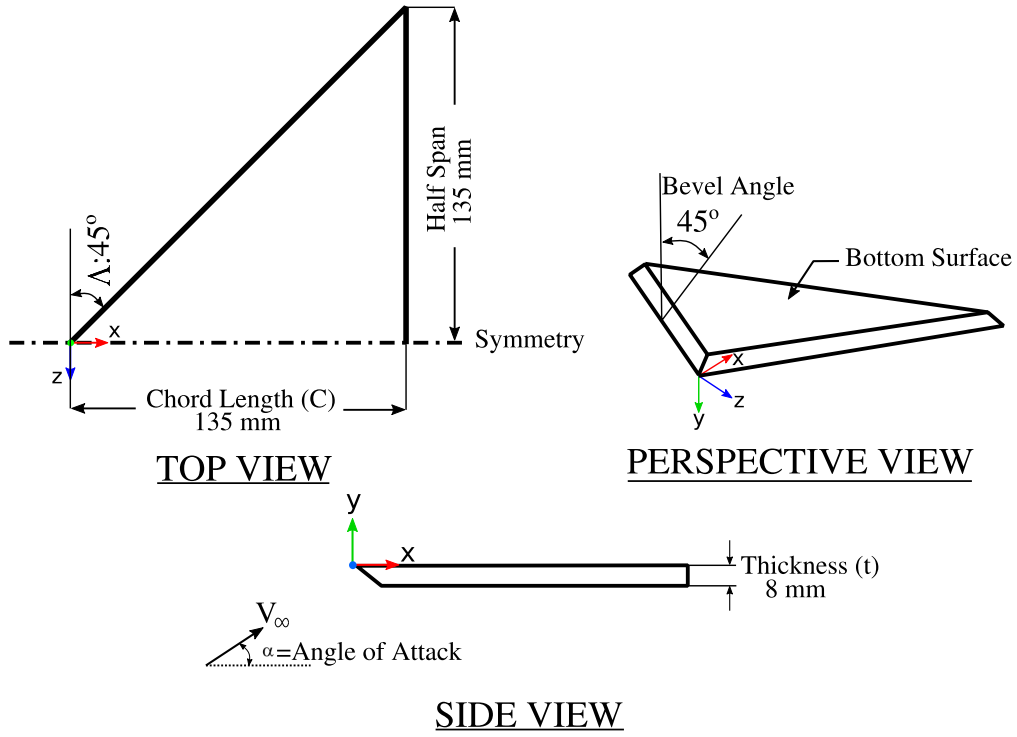

Figure 3-1. Dimensions of the Base Wing

3.1.2. Bleeding Wing used in Validation

Other than the base wing, one of the bleeding cases examined by Karagöz will also be used for validation. In the selected case, there are five bleed holes with a back angle of $\theta = 18°$ and edge angle of $\phi = 18°$ as shown in Figure 3-2. The holes are positioned parallel to the beveled leading edge. Each hole has a length of L = 21 mm and a width of 3 mm. The ends of the holes are rounded by 1.5 mm radius arcs. The distance between the holes is s = 4 mm, the distance from the holes to the leading edge is d = 3.5 mm and the distance between the first hole and the bevel surface is a = 9 mm. Other geometrical details of this wing are the same as the base wing.

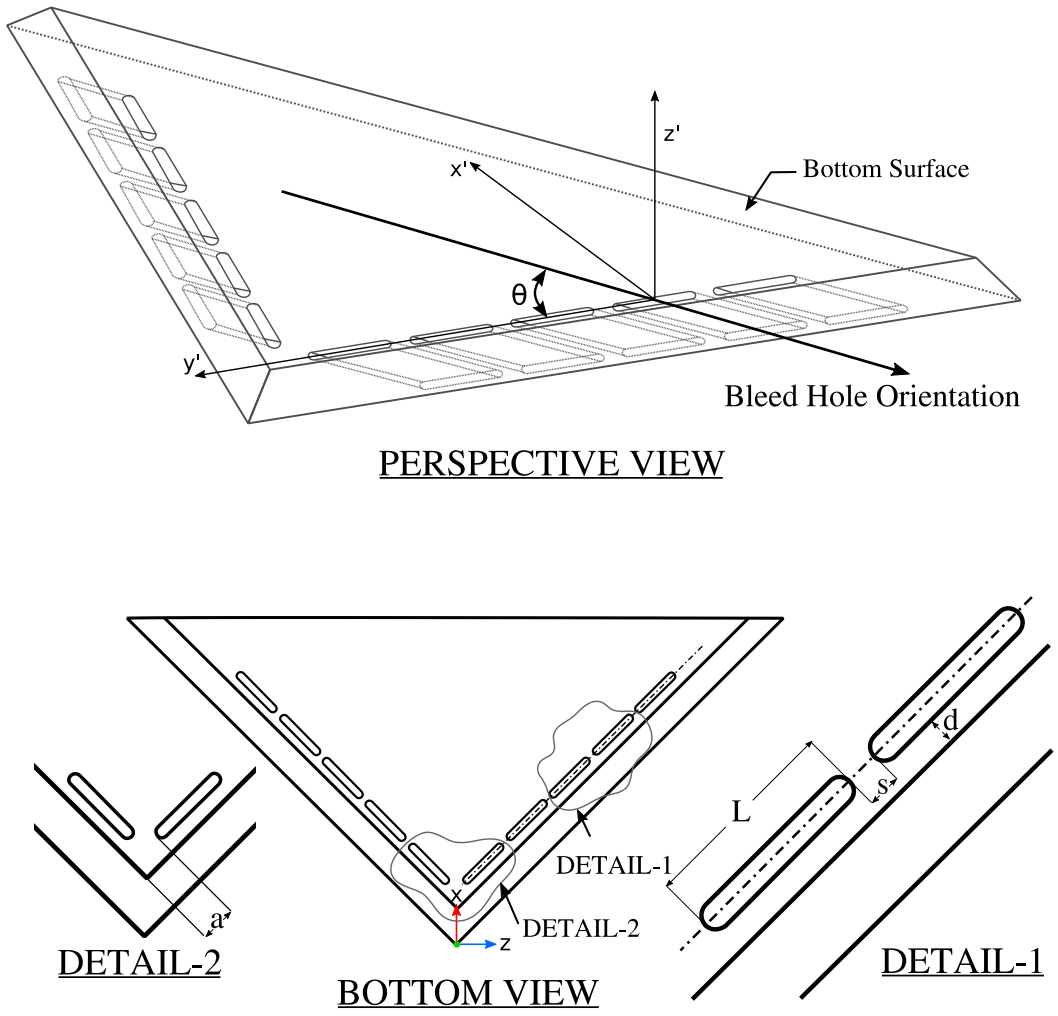

Figure 3-2. Illustration of Bleeding Wing Dimensions used in the Validation Study [19]

3.1.3. Extra Bleeding Wings

The bleeding wing introduced in the previous section is used for validation purposes, but it is not the only bleeding configuration used in the current study. In parallel with the ongoing experimental studies in the METU Fluid Dynamics Laboratory at Mechanical Engineering Department, bleeding holes are combined into a single hole, as shown in

Figure *3-3*, resulting in the fully open configuration. The location of the starting point of the first hole and the ending point of the fifth hole are kept the same as the original 5-hole configuration. The width of the hole and arc radii used at the ends are also kept the same.

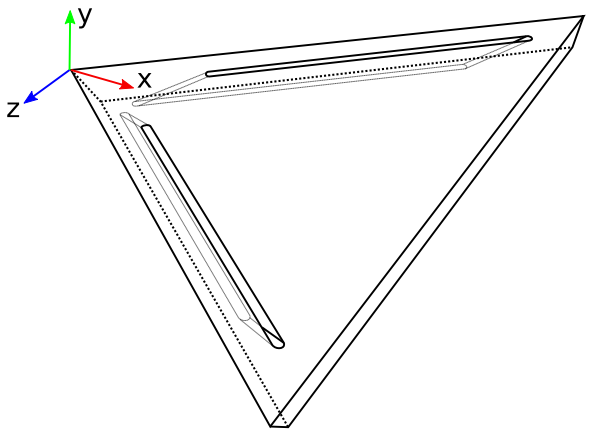

Figure 3-3. Fully Open Bleeding Wing

In the above configurations the holes are aligned parallel to the leading edge. This alignment is thought to have an effect on the flow field and to study it a new angle called the yaw angle (Ω) is defined, as shown in Figure 3-4. In this study, a single yaw angle was examined. When determining the angle to be studied, the results of the reference bleeding wing are examined and the areas where reverse flow is observed at 17° AoA are taken as a basis in selecting the yaw angle to be studied as 5.5°. The determined yaw angle is applied to both five-hole and fully open configurations. The modified five-hole and fully open wings are shown in Figure 3-5.

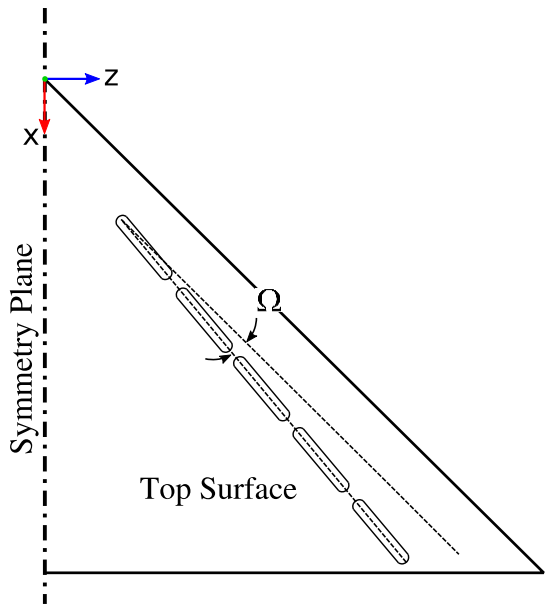

Figure 3-4. Definition of Angle Ω

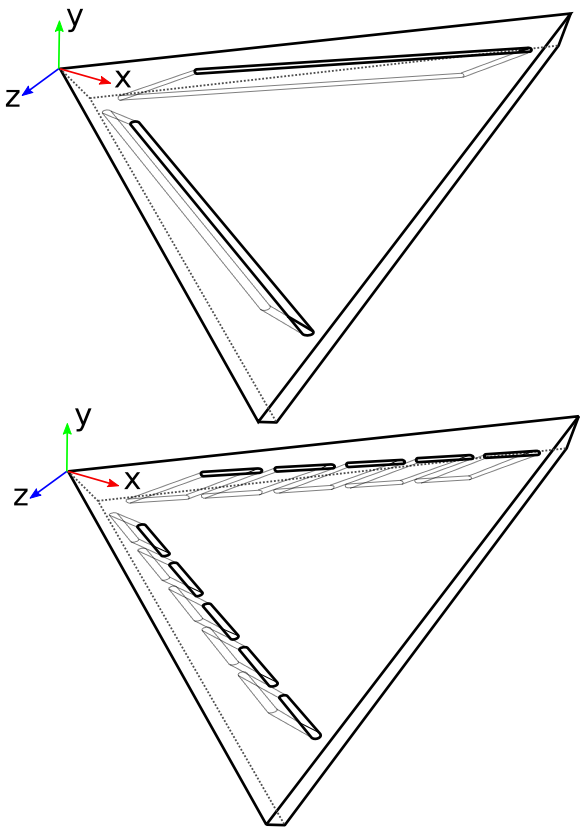

Figure 3-5. Modified versions of Five Hole and Fully Open Configurations Using $\Omega = 5.5°$

After examining the effects of the holes on the flow field (with extra configurations tried and not mentioned here), it is anticipated that bringing the exit of the first hole on the upper surface closer to the apex of the wing can be useful. However, shifting the first hole by the desired amount was not possible because the bevel surface on the pressure side was already very close to the first hole on the bottom surface. In case of a shift, the bevel surface would have lost its integrity. Therefore, a new configuration is proposed with each hole having a different back angle, as shown in Figure 3-6. By gradually varying the back angle from 26^o at the first hole to 18^o at the last one, it is now possible to move the exit of the first hole closer to the apex as seen in the figure by the comparison with the original 5-hole configuration. By this way it is possible to shift the first by 8.2 mm towards the apex.

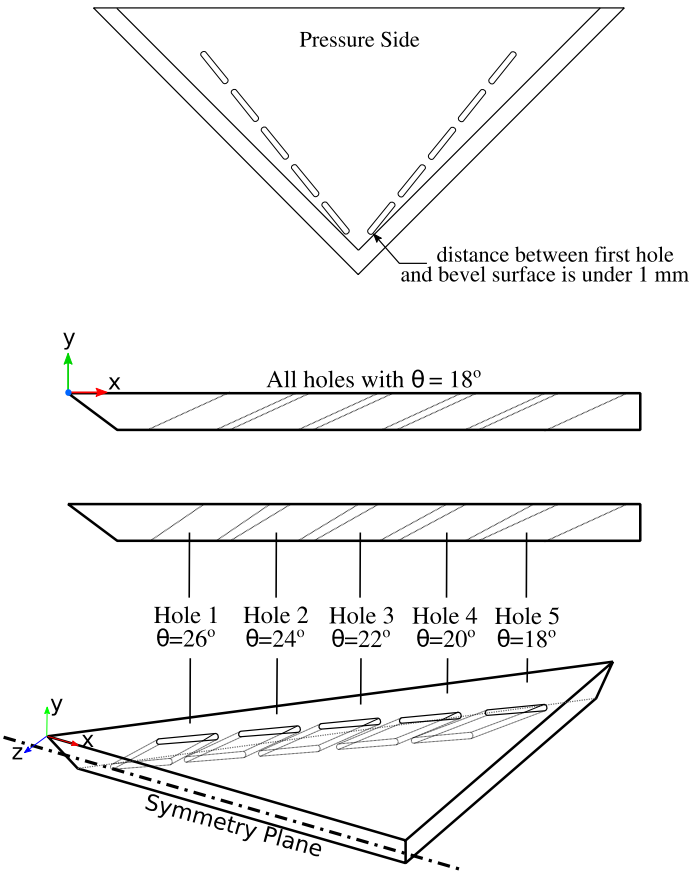

Figure 3-6. Bleeding Wing with Gradually Changing Back Angles and $\Omega = 5.5°$

3.2. Simulation Domain and Boundary Conditions

In CFD simulations of external flows, the problem domain size may have a significant effect on the results. Selecting the domain as too small may cause boundary conditions to alter the flow close to the wing and thus affecting the results. On the contrary, selecting it as unnecessarily large increases the number of mesh elements, resulting in long run times. In this study, the problem domain shown in Figure 3-7 is selected after a series of preliminary runs In these runs, first a very large flow domain is selected. Flow domain size is systematically made smaller and the results are compared to make sure that the results are independent of the domain size, i.e. even the smallest domain used to get the final results are not being affected artificially by the boundary conditions. It is assumed that the flow is symmetrical with respect to the wing centreline. For this reason, half of the wing is modelled. To test the symmetrical flow assumption, the base and the reference bleeding wings are also modelled as full wings and the results of simulations performed at 17° AoA are compared with the results obtained using half-wings. The differences in the vortex core location and surface pressure distribution were minimal, indicating that the flows are indeed symmetrical.

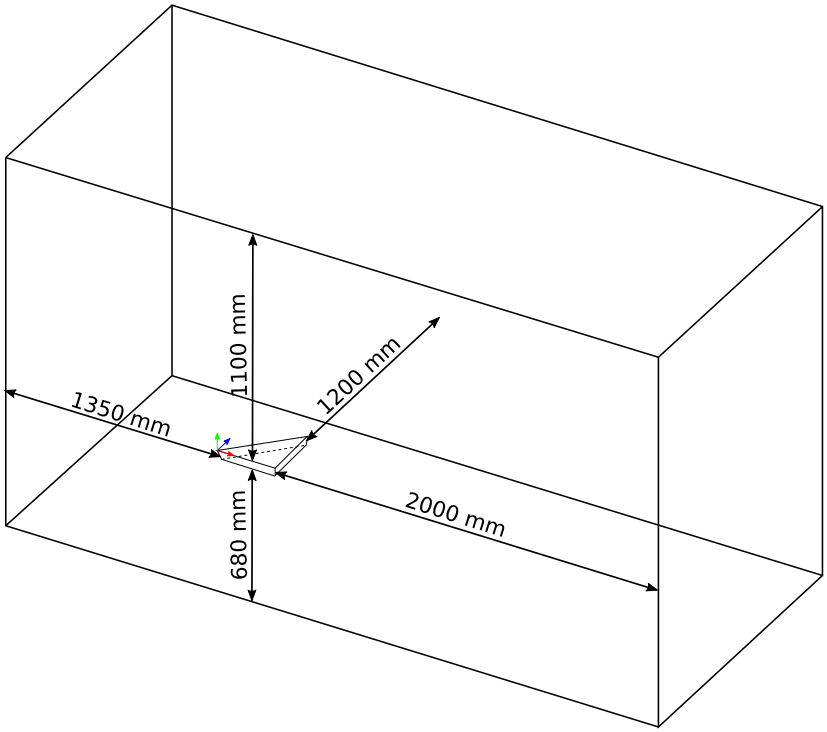

Figure 3-7. Dimensions of Flow Domain with Half Wing Inside

Boundary conditions used in the simulations are shown in Figure 3-8. Inlet boundary condition is defined on the left and bottom surfaces of the flow domain. Reynolds number based on the chord length is 75,000 in all the analyses, which corresponds to an inlet speed of 8.86 m/s. The direction of this uniform inlet speed depends on the attack angle. By defining the left and lower surface of the flow volume as inlet, it was possible to define the attack angle by providing proper *x* and *y* velocity components without changing the orientation of the wing. Turbulence characteristics are also important at the inlet boundary. At this point, the turbulence values measured in the wind tunnel experiments of Karagöz's study [18] were examined and turbulent intensity of 0.9% and turbulent viscosity ratio of 10 are specified at the inlet to support the validation study. After the validation study, the same inlet turbulence characteristics are used all other simulations.

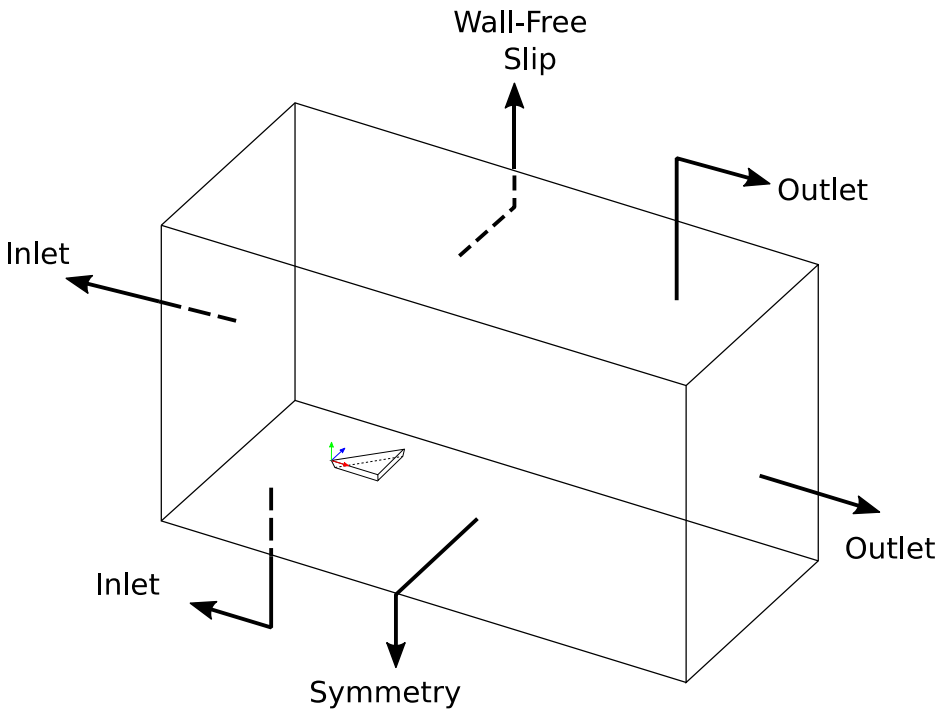

Figure 3-8. Boundary Conditions

The outlet boundary condition with zero-gauge pressure is defined on the upper and right surfaces of the flow domain. The surface of the flow domain passing through the wing centerline is defined as a symmetry boundary. The side surface of the flow volume away from the wing is defined as a free slip wall, which sets all three shear stress components on that surface to zero. Wing surfaces and the surfaces of the bleeding holes are assumed to be smooth and defined as no-slip walls Boundary conditions used are summarized in Table 3-1.

Table 3-1. Boundary Conditions Details

Name Selection	Boundary Condition Type	Parameter	Value
Inlet	Velocity Inlet	Velocity (m/s)	8.86
		Turbulent Intensity (%)	0.9
		Turbulent Viscosity Ratio	10
Outlet	Pressure Outlet	Gauge Pressure (Pa)	0
Wing Surface and Holes	Wall	No Slip	-
Side Wall	Wall	Free Slip	-
Symmetry	Symmetry	-	-

3.3. Simulation Parameters and Solver Settings

Air is the working fluid. Since the analyses are performed at low Reynolds number and in constant temperature conditions, the density and viscosity of air are assumed to be constant. Fluid properties are defined in accordance with the experimental conditions of Karagöz's study [18] in order to make a proper validation study. Air density and viscosity are taken as $1.204\ \mathrm{kg/m^3}$ and $1.8375 \times 10^{-5}\ \mathrm{kg/(ms)}$, respectively.

One of the major parameters affecting the simulation results is how the turbulence is modelled. In his thesis work on delta wings, Küçükyılmaz [49] compared different turbulence models and found that the $k-\omega$ SST with Curvature Correction (CC) model gave the most accurate results. Based on this, at the beginning of this study, the $k-\omega$ SST with CC turbulence model was used. However, the wing used by Küçükyılmaz was a slender type wing and the Reynolds number was around 1.5M. Because of these differences, the performance of different turbulence models is also tested during the validation runs and the $k-\omega$ SST with CC turbulence model was

found to give the closest results to the experiments, in parallel with Küçükyılmaz's study. Therefore $k-\omega$ SST with CC model is used in all the analyses performed in this study.

Simulations are performed using steady formulation in ANSYS Fluent. The pressure-based coupled solver is used. The gradient discretization is performed using the Green-Gauss Node Based method. PRESTO! scheme is used for pressure discretization and the second-order upwind scheme is used for everything else. All schemes and discretization methods used in the analyses are given in Table 3-2. To check the steadiness of the flow fields and the correctness of performing steady simulations, unsteady simulations are also performed for the reference bleeding wing at 17° AoA. In unsteady simulations, it is observed that the vortex core location did not change with time and was in the same location with steady simulation results. In addition, the surface pressures are calculated as both instantaneous and time-averaged and compared with steady simulation results. They are all found to be almost identical In the light of these observations, it is found that unsteady effects are not critical for the cases studied in this study and steady simulations are applicable

Table 3-2. Methods and Discretization Schemes Used

	Methods and Discretization Schemes
Pressure-Velocity Coupling	COUPLED
Gradient	Green-Gauss Node Based
Pressure	PRESTO!
Momentum	Second Order Upwind
Turbulence Kinetic Energy	Second Order Upwind
Specific Dissipation	Second Order Upwind

Convergence is followed on the residual graph, as well by the help of defined monitors. Velocity data are obtained at nine control points shown in Figure 3-9 and used for monitoring. This monitoring not only ensures that the solution converges, but also shows indications of any unsteadiness present in the flow field, if there is any. In addition to monitoring velocities, the drag and lift forces on the wing are also monitored in declaring convergence. Residuals and variations of drag and lift forces, as well as the velocities at the selected control points during the iterations of a selected run are given in Figure 3-10. All simulations were initialized by the Full Multi Grid (FMG) method and convergence was achieved between 1000 - 4000 iterations in all simulations.

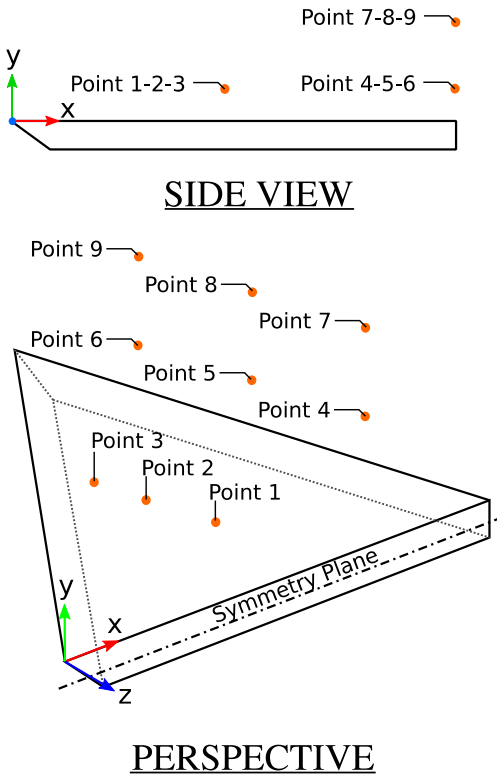

Points	X Coordinate (m)	Y Coordinate (m)	Z Coordinate (m)
Point-1	0.065	0.01	0.015
Point-2	0.065	0.01	0.035
Point-3	0.065	0.01	0.050
Point-4	0.135	0.01	0.035
Point-5	0.135	0.01	0.0675
Point-6	0.135	0.01	0.1
Point-7	0.135	0.03	0.035
Point-8	0.135	0.03	0.0675
Point-9	0.135	0.03	0.1

Figure 3-9. Locations of Monitoring Points used for Convergence Check

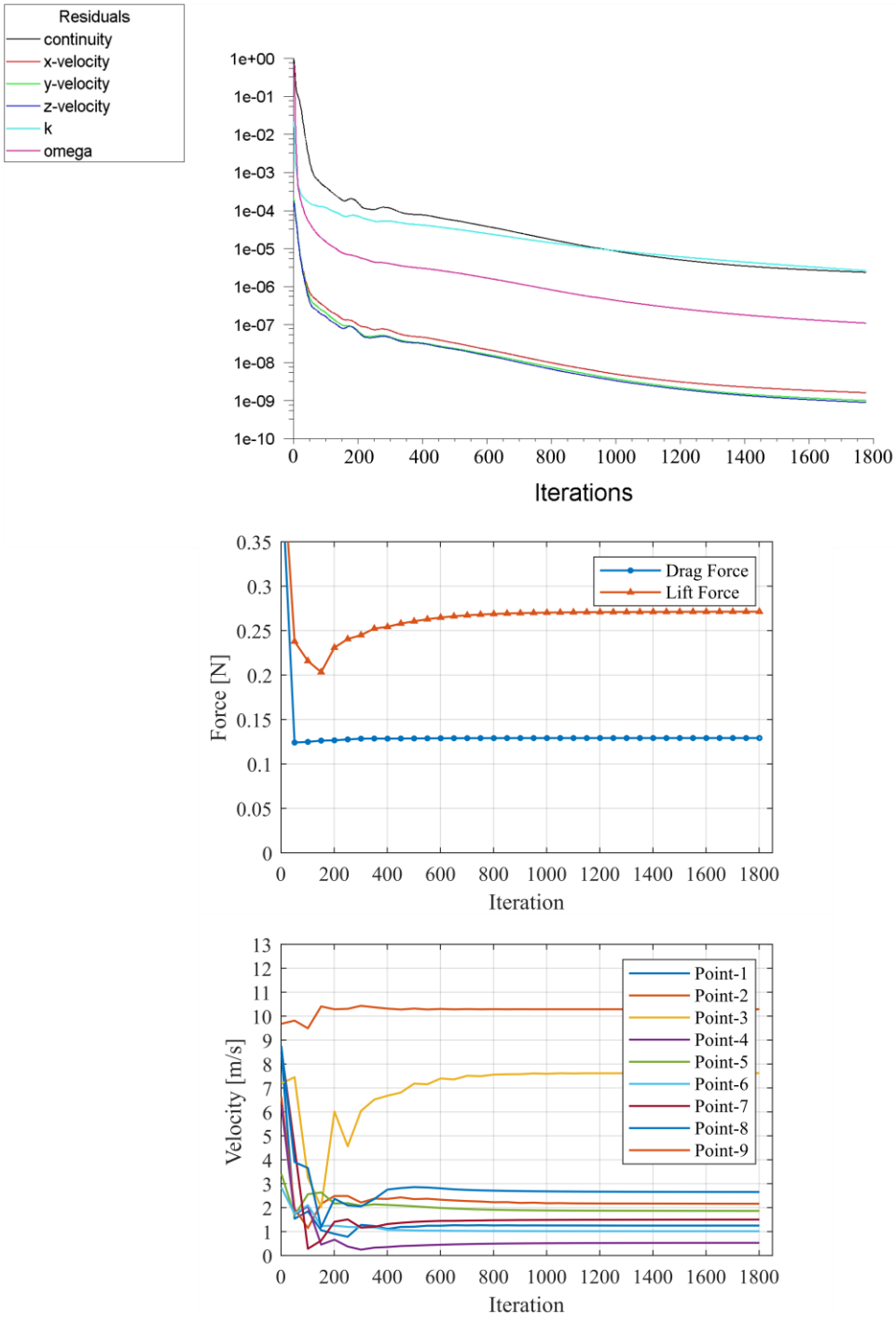

Figure 3-10. Residuals and Convergence Monitors

3.4. Mesh Generation

Mesh generation is very critical in a CFD study, affecting not only the accuracy of the results but also the number of iterations required for convergence and therefore the run time. The shape and the size of the problem geometry and physics to be resolved are the most important inputs of the mesh generation process. Mesh element types commonly used are tetrahedral, hexahedral, polyhedral and Cartesian with cut cells. Each element type has advantages and disadvantages over the others. For example, using hexahedral elements result in a low total number of elements and quick convergence. But it is extremely difficult to construct a high quality full hexahedral mesh in complex geometries. Tetrahedral elements can easily generate high-quality meshes inside complex geometries with automatic algorithms but may cause problems in convergence. Also, their use is not suggested inside boundary layers where the flow has a dominant flow direction, which can be discretized and solved more accurately using hexahedral elements. Another mesh type is polyhedral mesh which contains polyhedral cells. Its main advantage compared to tetrahedral or tetrahedral-hexahedral hybrid meshes is the lower overall cell count, almost 3 - 5 times lower. Additionally, polyhedral meshes can provide convergence with fewer iterations. On the other hand, in ANSYS Fluent polyhedral meshes cannot be generated directly. The starting point of the polyhedral mesh generation process is a valid surface mesh which must be a triangular mesh of good quality.

In this thesis, a very detailed mesh generation study is performed to shorten the simulation times, improve convergence and obtain high accuracy. Throughout the preliminary runs, several different meshes with all different element types mentioned above are used. Hybrid meshes, such as those combining tetrahedral and hexahedral or hexahedral and polyhedral elements are also tested. Figure 3-11 shows examples of some of the meshes tested. As a result of detailed tests and comparisons, the most advantageous mesh type in terms of both memory requirement and run time turned out to be the meshes with all polyhedral elements. Therefore, such meshes are used in all of the analyses performed in this study.

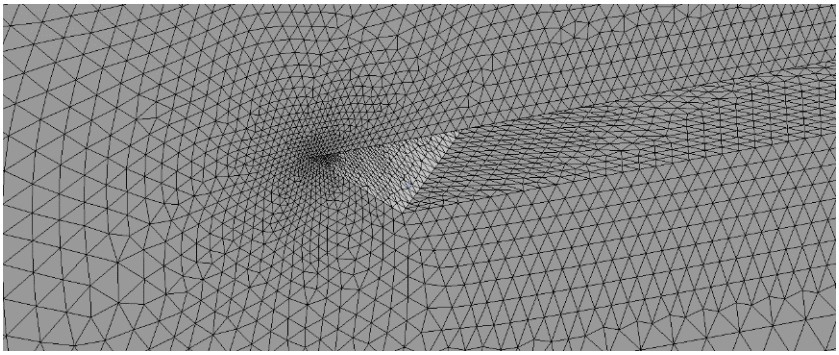

a)

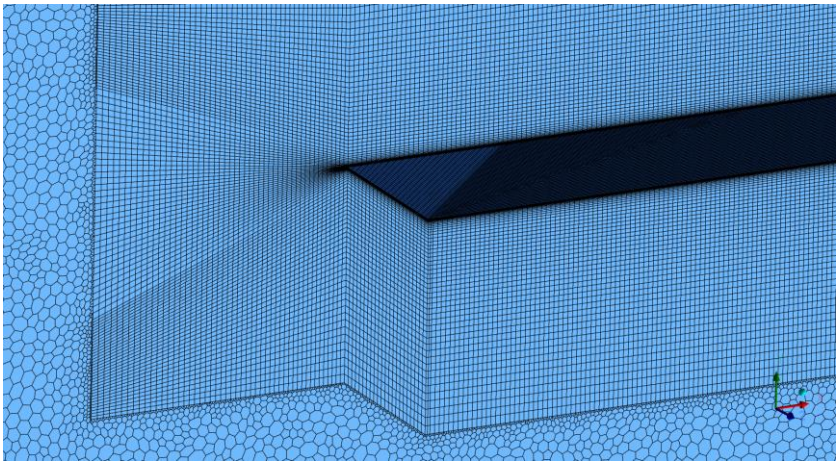

b)

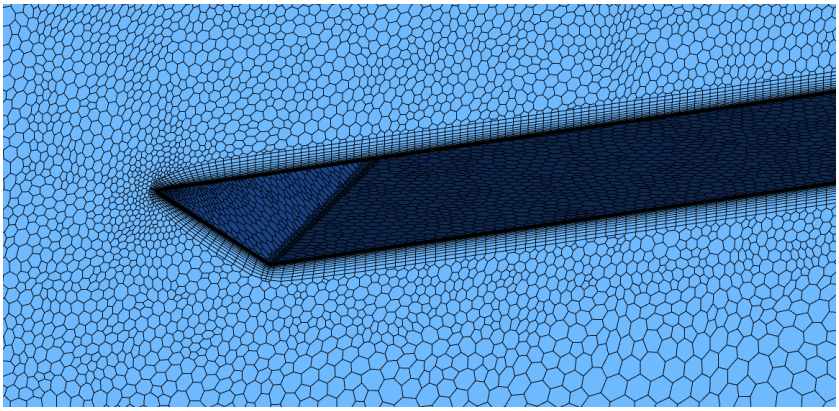

c)

Figure 3-11. a) Tetrahedral Mesh b) Hybrid Hexahedral-Polyhedral Mesh c) All Polyhedral Mesh

The region where the greatest changes are seen in the flow domain is close to the wing. Therefore, it is necessary to mesh a certain region around the wing with denser elements. As shown in Figure 3-12, three refinement regions are defined around the wing to control the mesh density. The mesh is allowed to get gradually coarser from the inner to the outer layers. The dimensions of these regions were determined and optimized by a set of auxiliary simulations, starting with very large refinement regions, and making them smaller systematically. The shown refinement regions are obtained at the end of this process and it is ensured that solutions are independent of the refinement region sizes.

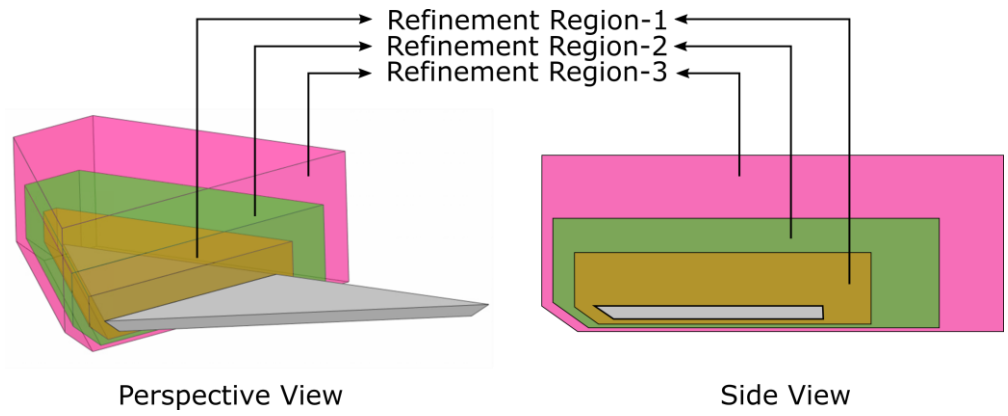

Figure 3-12. Refinement Regions used to Control Mesh Density

One of the important points in the mesh generation process is the generation of the boundary layer mesh, for which the requirements of the turbulence model used is critical. In this study, the $k-\omega$ SST CC turbulence model is used, which requires that the y^+ value to be about 1 on surfaces with wall boundary conditions. For this reason, the boundary layer meshes consisting of 20 layers are used, with the first layer heights carefully selected to provide $y^+ \approx 1$ on the walls. In all analyses, the results are examined for the adequacy of y^+ and the total thickness of the boundary layer. The

properties of the boundary layer mesh used are given in Table 3-3. In addition, the boundary layer images from different parts of the wing are shown in Figure 3-13.

Table 3-3. Details of the Boundary Layer Mesh

	Dimension
Number of Layers	20
First Layer Height at Wing Surface	1.4×10^{-2} mm
First Layer Height at Bleeding Holes Surfaces	1.2×10^{-2} mm
Growth Rate	1.1

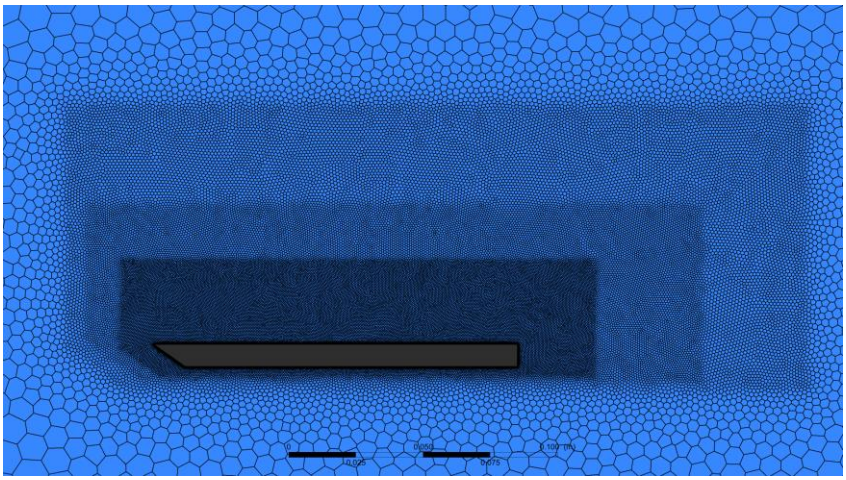

a)

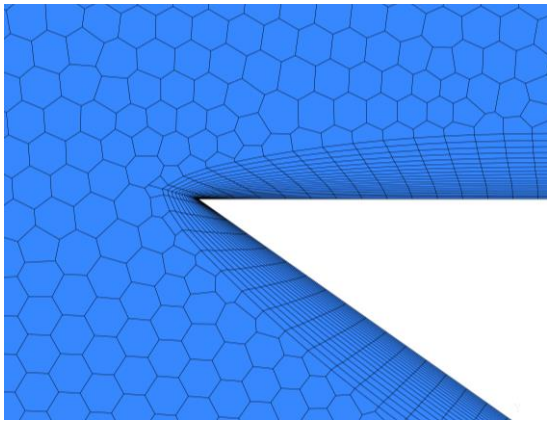

b)

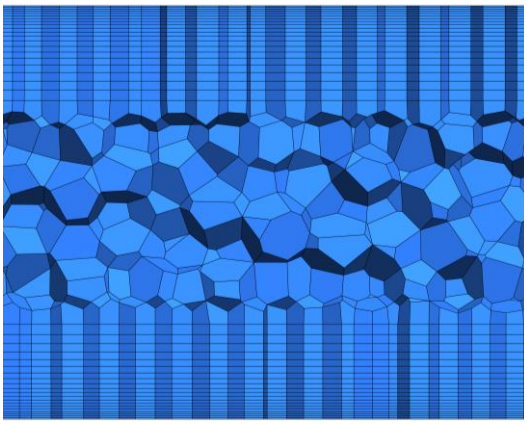

c)

Figure 3-13. Boundary Mesh Examples at Different Locations a) Mesh Aroun the Leading Edge b) Mesh inside a Bleeding Hole

3.5. Mesh Independence Study

In this part of the thesis, details of the mesh independence study, which is conducted in two steps, first for the base wing and then for the bleeding wing with 5 holes, are provided.

3.5.1. Mesh Independence for the Base Wing

The parameters critical to the mesh independence study are the sizes of the surface elements and the maximum element sizes in the refinement regions. Six different meshes are generated for the base wing geometry by changing these parameters as shown in Table 3-5. As seen, the sizes of the element faces on both the pressure side (lower surface) and the top surface of the wing, as well as the sizes of the elements inside the refinement regions, are decreased gradually starting from the coarsest Mesh-1. Since separation and re-attachment will be observed on the upper surface, finer elements are used there compared to the lower surface for coarser meshes. As the meshes get finer, there is no need to make a difference between the lower and upper surfaces. It is tried to create the meshes such that the number of elements increase about 2 times between successive refinements. Number of elements vary between 375 thousand to 17.5 million.

Table 3-4. Meshes Used for the Base Wing (All sizes are in mm)

	Mesh-1	Mesh-2	Mesh-3	Mesh-4	Mesh-5	Mesh-6
Element Face Size (Upper Surface)	3	1.5	0.75	0.5	0.4	0.3
Element Face Size (Lower Surface)	4	2	1	0.5	0.4	0.3
Refinement Region-1	4	2	1.25	0.75	0.55	0.4
Refinement Region-2	6	3	1.75	1.25	1	0.6
Refinement Region-3	10	5	2.25	1.75	1.25	1
Number of Elements	375 K	900 K	1.9 M	4.9 M	9.5 M	17.5 M

To check mesh independence, first, the pressure variation on the upper surface along spanwise lines at the $x/C = 0.3$, $x/C = 0.5$ and $x/C = 0.7$ (see Figure 3-14) are used, where C is the chord length. Pressure values are collected from 100 points along each line and non-dimensionalized using

$$C_p = \frac{p - p_\infty}{\frac{1}{2}\rho U_\infty^2} \tag{3.1}$$

where p is the pressure, $p_\infty = 101325\, Pa$ is the free stream pressure, U_∞ is the freestream velocity and ρ is the density. Pressure variations are given as negative pressure coefficient in Figure 3-15. This study is carried out at an angle of attack of $\alpha = 17^o$ for which the flow is dominated by the vortical structure formed by the separation from the leading edge. The non-dimensional spanwise distance z/S, with S being the half span width, is measured from the symmetry line to the leading edge. When the results are examined, it is seen that the $-C_p$ curve get flattened and converges as we move from Mesh-1 to Mesh-6. The results of the last two meshes are close to each other with maximum deviation being less than 4.2 %.

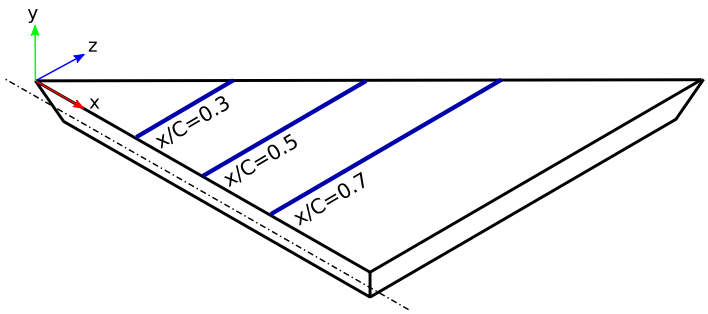

Figure 3-14. Pressure Measurement Lines

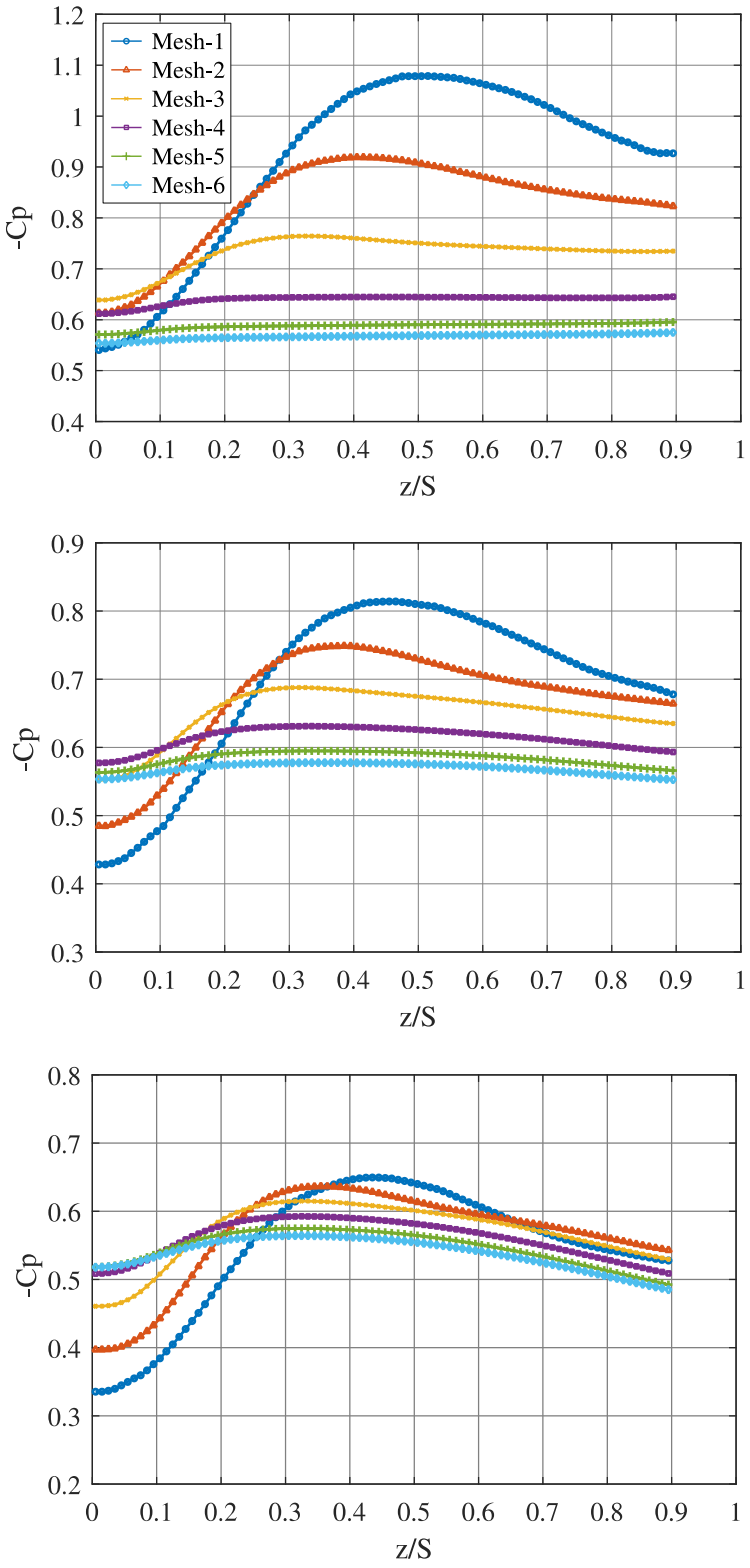

Figure 3-15. Negative Pressure Coefficient on the Upper Surface at x/C=0.3 (top), x/C=0.5 (middle), x/C=0.7 (bottom) ontained by Different Meshes

Figure 3-16 shows the shear stress lines at the upper surface of the wing obtained by different meshes. Convergence as the mesh is refined can be seen here too.

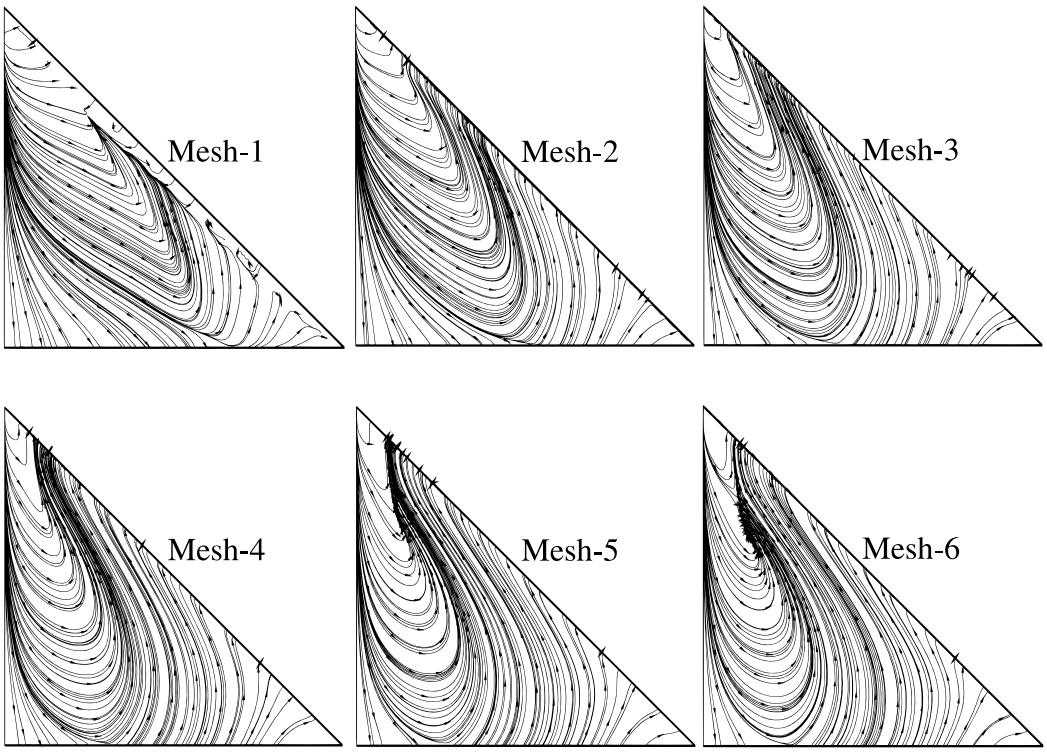

Figure 3-16. Shear Stress Lines at the Upper Surface Obtained by Different Meshes

Next, the streamlines are visualized at 2 planes parallel to the upper surface, 1 mm and 3 mm away from the surface. The results are given in Figure 3-17, and once again it can be seen that the results converge as the mesh is refined and the ones for Mesh-5 and Mesh-6 are very close to each other.

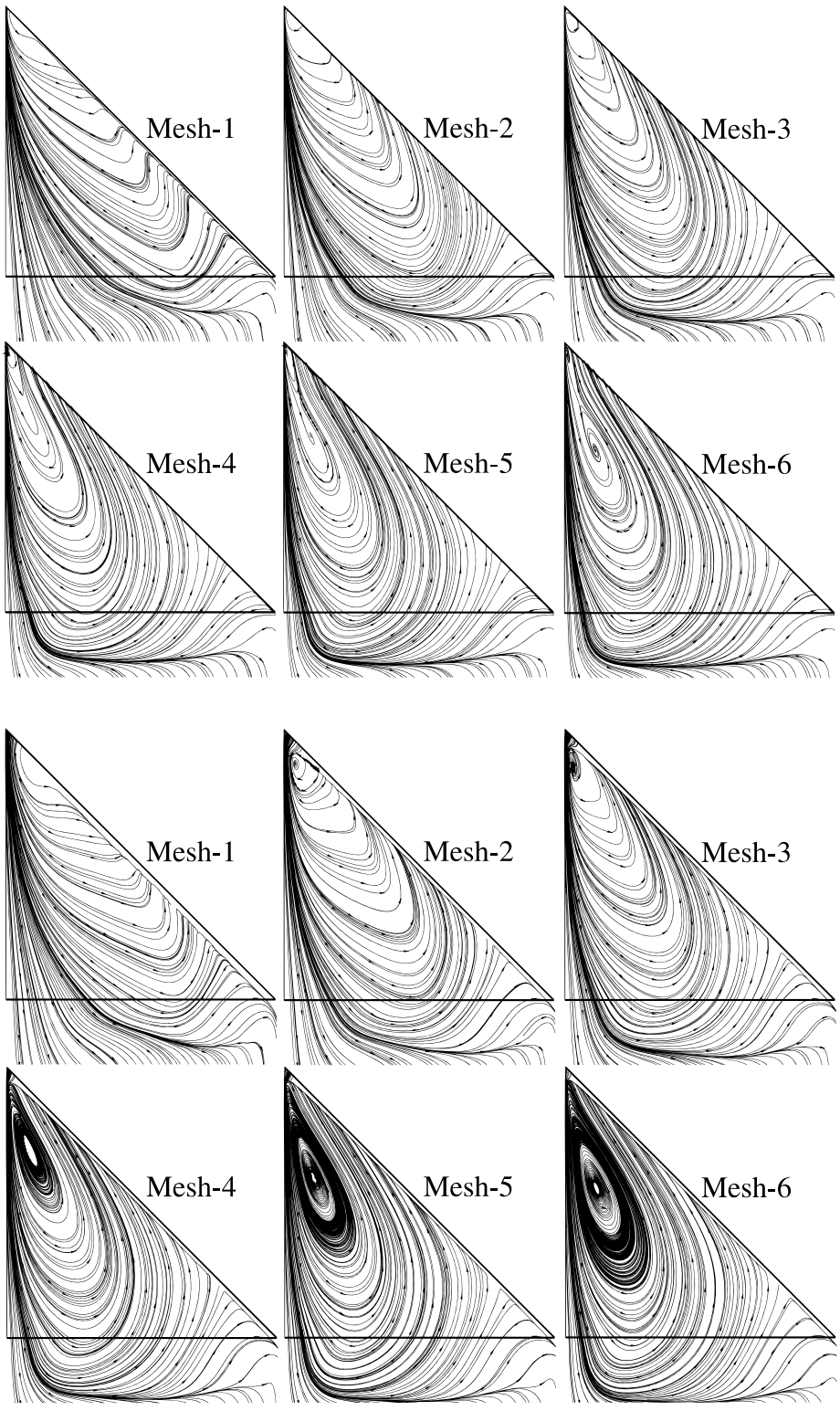

Figure 3-17. Streamlines on Two Different Planes Parallel to the Upper Surface. Top two rows: 1mm, Bottom two rows: 3 mm Away from the Surface

u velocity contour is of great importance to see the reverse flow zones on the top surface of the wing. In Figure 3-18, -u zone is given on the plane that is 3 mm away from the top surface of the wing. By using only one contour line, it is possible to distinguish negative u zones, as dark gray color. Last two meshes seem to provide identical results.

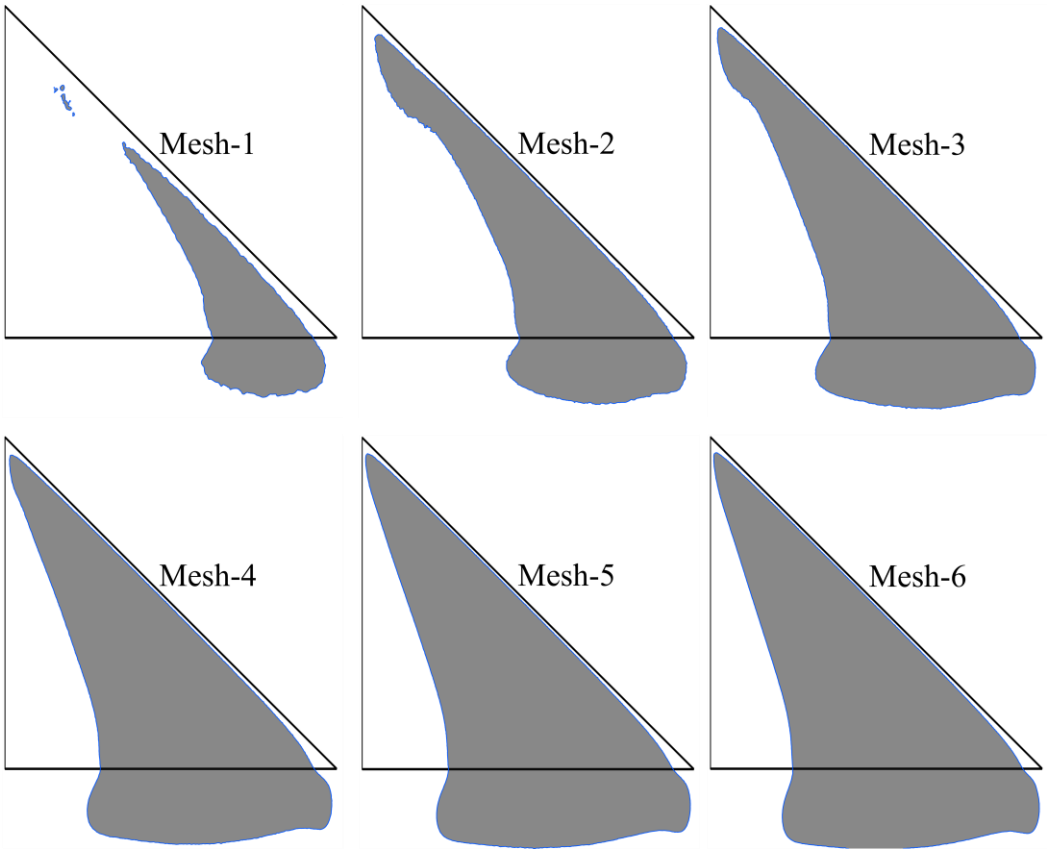

Figure 3-18. u Velocity Contour on the Plane 3 mm Away from Top Surface. Gray Color Shows Negative u Zones

For the final check of mesh independence on the base wing, drag and lift forces are compared in Figure 3-19 and Figure 3-20. Relative errors with respect to the Mesh-6 solution, which is expected to be the most accurate one, are also shown on the figure. As seen, the differences between Mesh-5 and Mesh-6 results are less than 1% for both drag and lift forces.

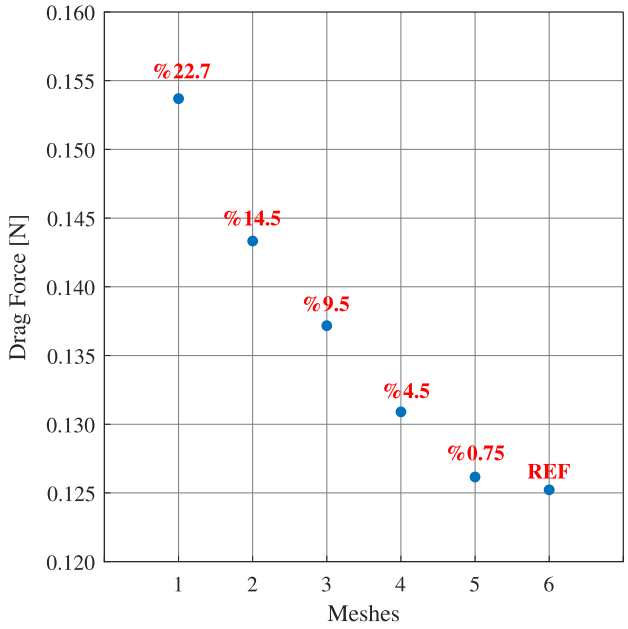

Figure 3-19. Base Wing Drag Force Comparison with Relative Errors

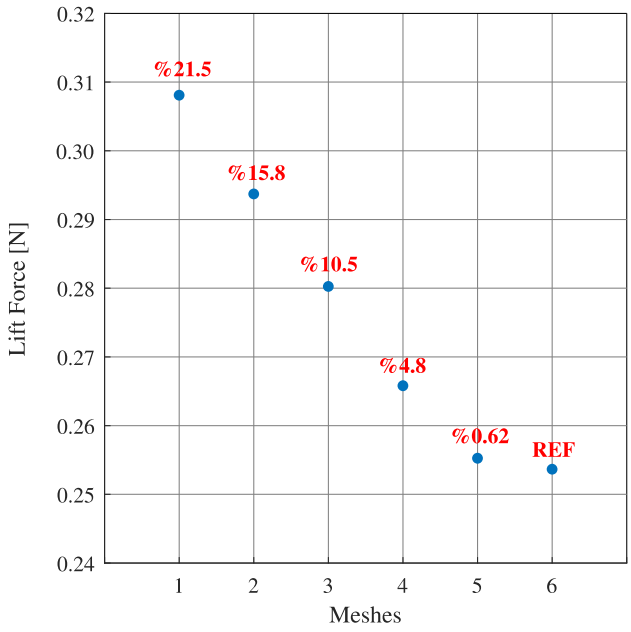

Figure 3-20. Base Wing Lift Force Comparison with Relative Errors

With all the checks given above, it is seen that a mesh independent solution for the base wing is indeed reached, and Mesh-5 is considered to be the suitable mesh to be used in further simulations.

3.5.2. Mesh Independence for the Bleeding Wing

The first bleeding wing with 5 holes described in Section 3.1.2 is also put into a mesh independence test, because the holes change the mesh topology and the flow structure considerably. Based on the results of mesh independence tests of the base wing, it is decided to generate meshes using the same settings of Mesh-5 and Mesh-6 of the previous section. But, after noticing considerable difference in their results, it is thought that the cells near the holes are not small enough and they are refined. Unfortunately, this could be done only for Mesh-5 to obtain a new mesh called "Mesh-5 with Fine Bleeding Holes (FBH)", but not for Mesh-6 because it already has 19 M cells and using a finer one was not possible considering the computational resources. In this study, the solutions are conducted by the parallel use of two workstations each having two Intel Xeon-5 2.6 Ghz CPUs and 64 GB 2133 MHz memories. Details of the meshes used in the mesh independence study of the bleeding hole configuration are given in Table 3-5. Average wall-clock times per iteration for each mesh can also be seen in the table.

Results are shown in Figure 3-21 – Figure 3-25, as negative $-C_p$ variations along three different spanwise lines, streamlines on two different planes parallel to the upper surface, $-u$ zone and drag and lift forces. After examining all these, it is decided that the settings used for generating "Mesh-5 with FBH" are the proper ones for bleeding wings and similar settings are used to create the meshes for all further simulations with bleeding holes.

Table 3-5. Meshes Used for the Bleeding Wing (All sizes are in mm)

	Mesh-5	Mesh-5 with Fine Bleeding Holes (FBH)	Mesh-6
Element Face Size (Upper Surface)	0.4	0.4	0.3
Element Face Size (Lower Surface)	0.4	0.4	0.3
Bleeding Holes Face Size	0.4	0.3	0.3
Refinement Region-1	0.55	0.55	0.4
Refinement Region-2	1	1	0.6
Refinement Region-3	1.25	1.25	1
Number of Elements	10 M	11 M	19 M
Average wall-clock time per iteration [s]	36.9	39.7	78.2

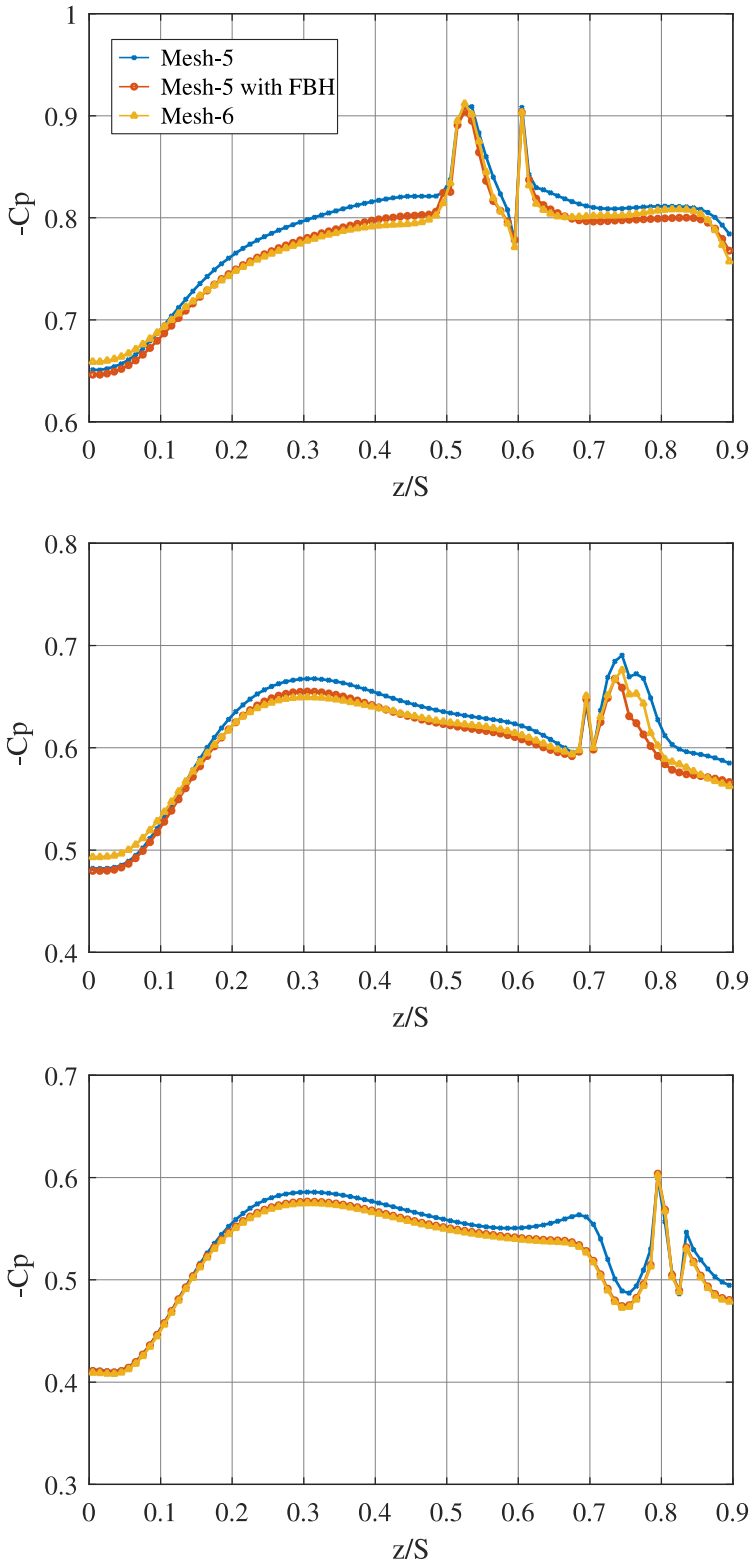

Figure 3-21. Negative Pressure Coefficient on the Upper Surface of the Bleeding Wing at x/C=0.3 (top), x/C=0.5 (middle), x/C=0.7 (bottom)

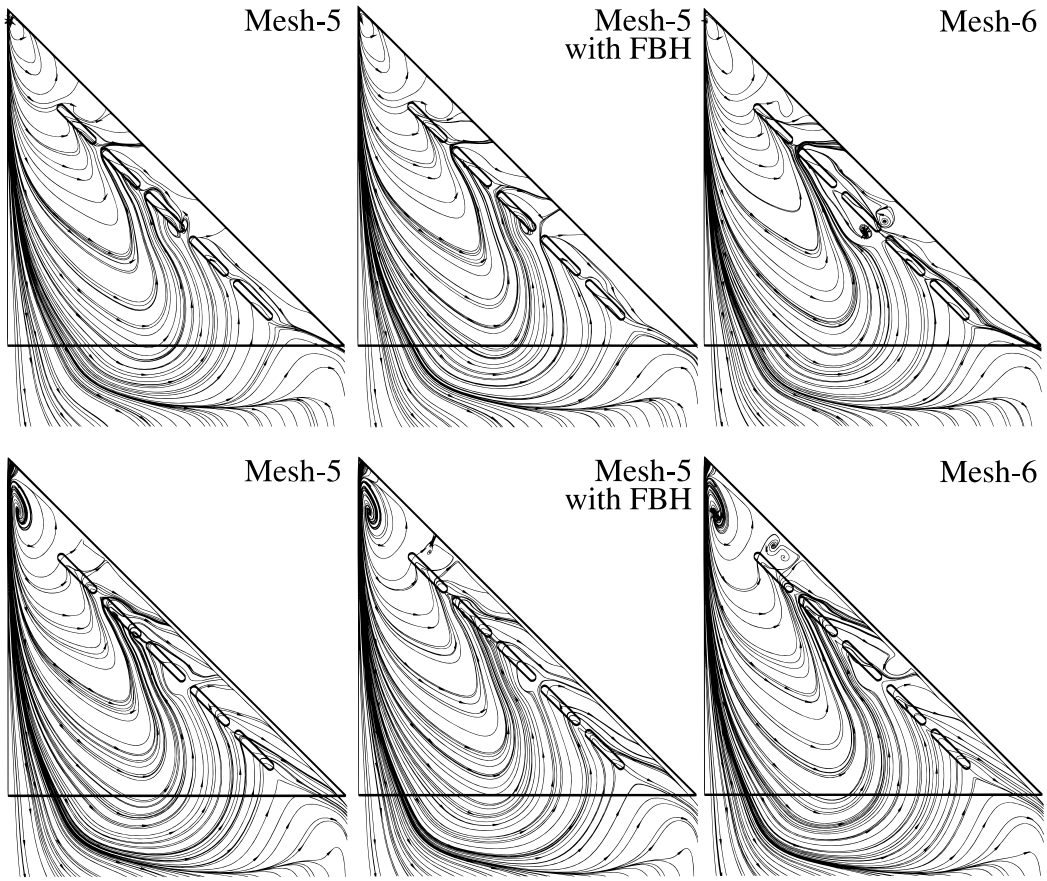

Figure 3-22. Streamlines on two Different Planes Parallel to the Upper Surface of the Bleeding Wing. Top row: 1mm, Bottom row: 3 mm Away from the Surface

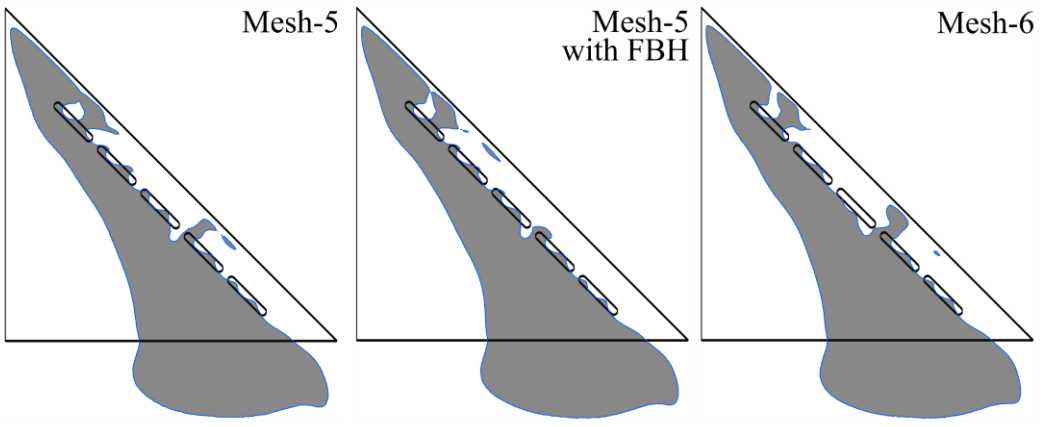

Figure 3-23. u Velocity Contour on the Plane 3 mm Away from Top Surface. Gray Color Shows Negative *u* Zones

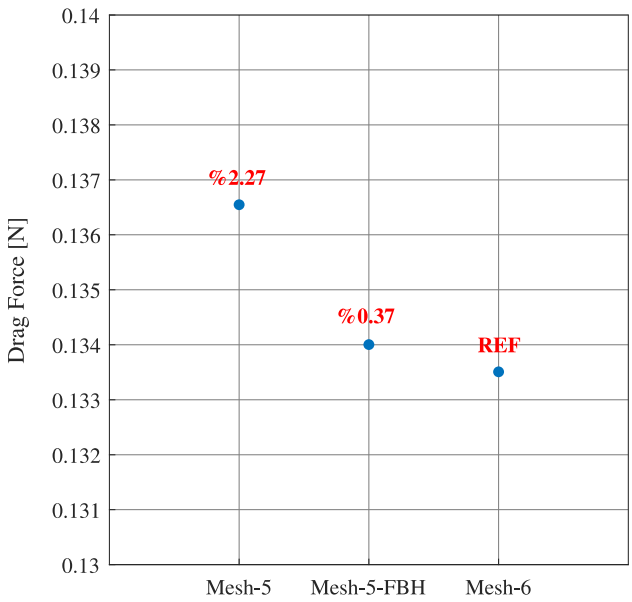

Figure 3-24. Bleeding Wing Drag Force Comparison with Relative Errors

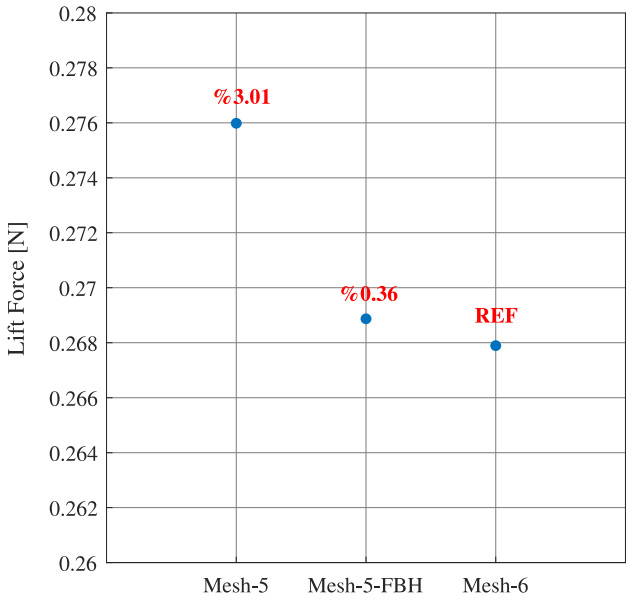

Figure 3-25. Bleeding Wing Lift Force Comparison with Relative Error

CHAPTER 4

VALIDATION STUDY

In this chapter, the numerical approach used in this thesis will be validated by comparing the results with the experiments performed by Karagöz [18] and Çelik [19]. This will be done first for the base wing and then for the bleeding wing with 5 holes, which was described in detail in the previous chapter.

To remember, Karagöz carried out her study at the Fluid Mechanics Laboratory of the Mechanical Engineering Department of METU. She performed experiments for the base and bleeding wings with various back angles. She manufactured the wings with rapid prototyping using fine polyamide PA2200 as the material. She studied different Reynolds numbers and attack angles. She used Laser Doppler Anemometry (LDA) and pitot-static tubes for wind tunnel characterization, measured surface pressure of the top surface using static holes, and visualized the flow field by Particle Image Velocimetry (PIV)

Out of the results available in Karagöz's study, we will make use of the following ones

- Base wing at Re=75000 and Angle of Attack (AoA)=18°.
- Bleeding wing with 18° back angle at Re=75000 and (AoA)=17° and 18°.

For both cases comparisons will be made using

- near-surface streamlines,
- cross-plane streamlines and velocity vectors,
- pressure coefficient variations along spanwise lines.

4.1. Comparison of the Base Wing Results

Figure 4-1 shows comparison of the streamlines on the plane 3 mm away from the top surface of the wing. The main characteristic of this high angle of attack flow over a non-slender wing with no flow control is that the vortical structure formed by the three-dimensional separation from the leading edge interacts with the boundary layer on the wing surface. This vortical structure is formed starting from the apex and dominates the flow in the top side. The positive and negative streamwise velocity component zones in the upper region of the wing and the wide vortex starting at the apex are observed in both the reference experiment and the current results. It can be said that the main flow characteristics are captured in the current solutions, with a certain amount of shift of the position of the vortex compared with the experiments.

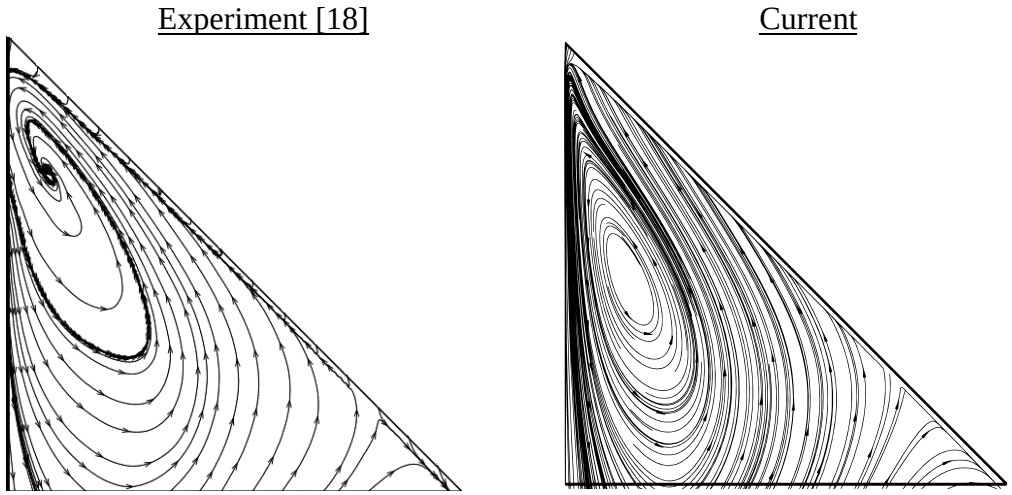

Figure 4-1. Comparison of Streamlines 3 mm Away from the Top Surface of the Base Wing at $\alpha = 18°$

In Figure 4-2, the streamlines and velocity vectors on the cross-plane at $x/C = 0.5$ are compared. Although the results are similar, current one predicts a smaller vortex core. The reattachment locations, where the velocity vectors are attached perpendicular to the wing, are very close to each other in both cases. The shared results belong to the upper region of the wing and are shared in reverse order to conform to

the representation in the literature, which should be taken into account when reviewing the results.

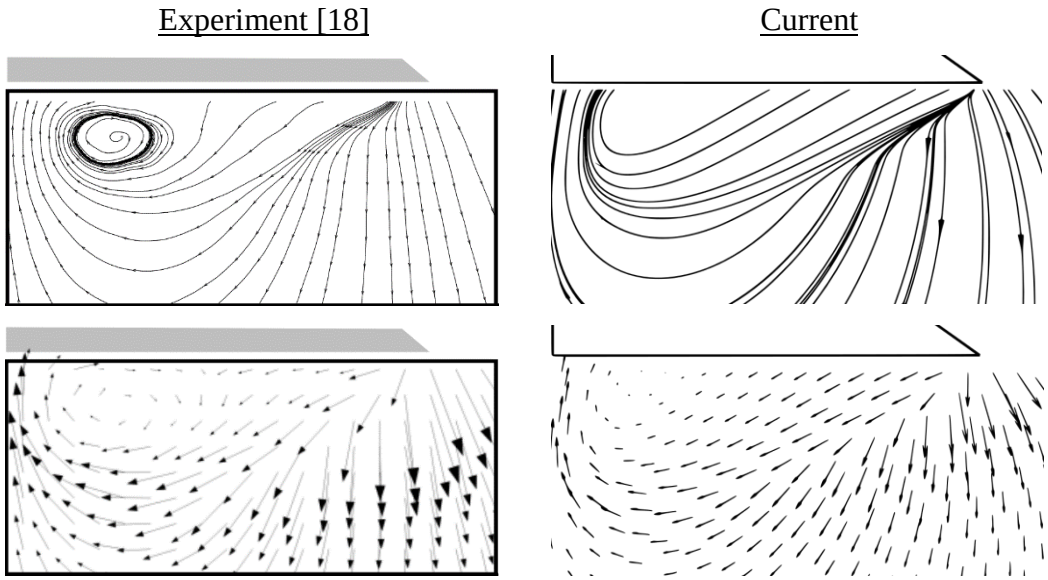

Figure 4-2. Comparison of Cross Plane Streamlines and Velocity Vectors for the Base Wing at $\alpha = 18°$

The final comparison for the base wing is carried out for the pressure coefficient in Figure 4-3. The pressure variation on the upper surface along the spanwise line at $x/C = 0.5$ is used. Although there is a considerable shift between them with deviations up to 20%, both results show flat-like behavior meaning that both can capture the three-dimensional separation with almost no lift generating capability. It is a known fact that obtaining surface pressures accurately is quite challenging in delta wing simulations. Especially RANS turbulence models can be insufficient at this point, as discussed in Chapter 2.

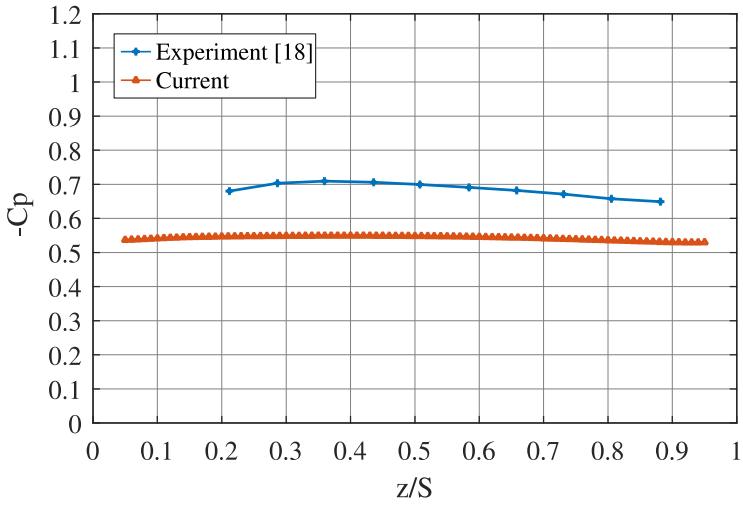

Figure 4-3. Pressure Coefficient Comparison for the Base Wing at $\alpha = 18°$

4.2. Comparison of the Bleeding Wing Results

In this section current results will be compared with the 5-hole bleeding wing studied by Karagöz [18]. Figure 4-4 shows the comparison of the streamlines on the plane 3 mm away from the top surface. The main characteristic of this flow with the passive bleeding applied is the regeneration of the desired vortical structure. In both results, it is seen that, compared with the base wing, the vortex core gets closer to the apex, more so in the current results. The reattachment line moves away from the wing's symmetry axis, especially after the mid-chord. With the effect of bleeding holes, reverse flow is prevented in regions close to the apex. The overall streamline patterns are quite similar, except in the region between the holes and the leading edge. The simulations cannot capture the details there.

Experiment [18] Current

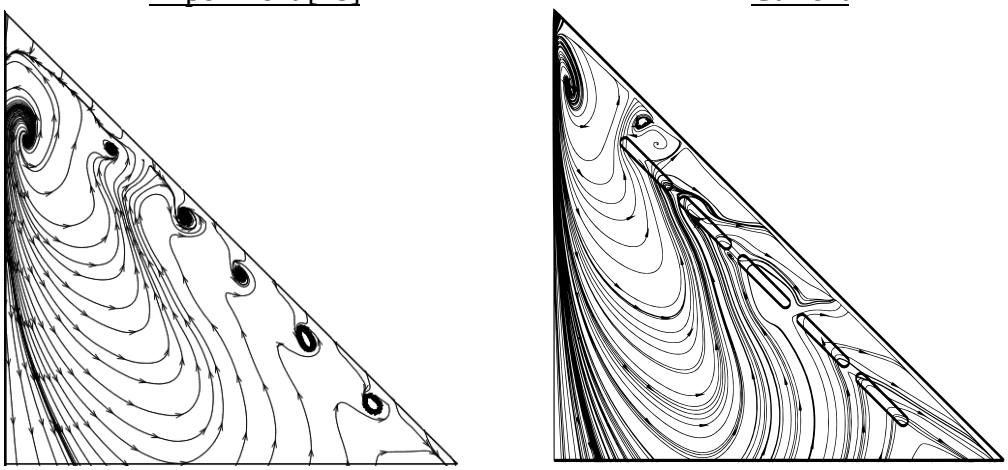

Figure 4-4. Comparison of Streamlines 3 mm Away from the Top Surface of the Bleeding Wing at $\alpha = 18°$

The cross-plane streamlines and velocity vectors at $x/C = 0.5$ are compared in Figure 4-5. As seen the flow fields are similar with similar vortex core locations and sizes. As a result of the bleeding application, the reattachment is strengthened and moved away from the wing centerline.

Experiment [18] Current

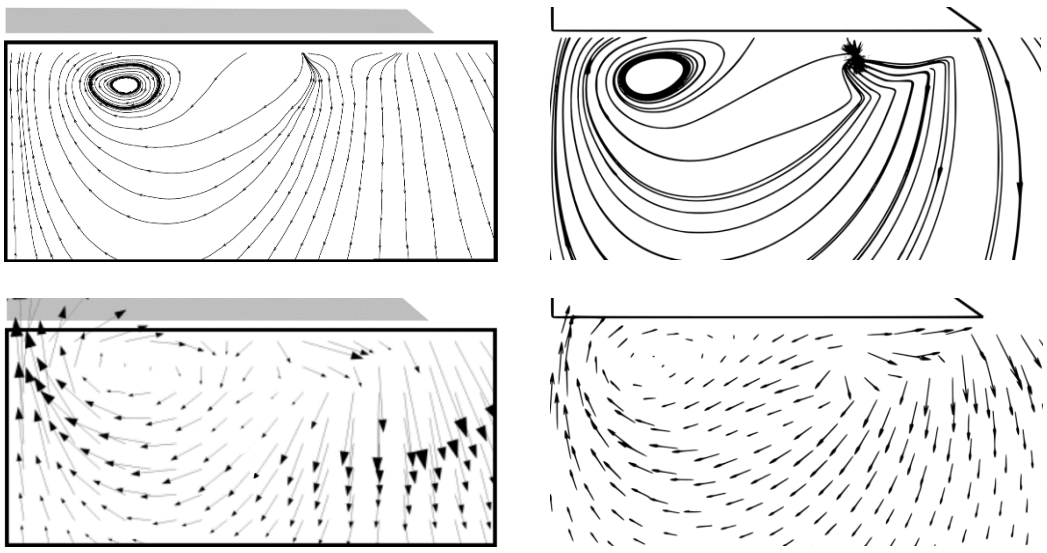

Figure 4-5. Comparison of Cross Plane Streamlines and Velocity Vectors for the Bleeding Wing at $\alpha = 18°$

Figure 4-6 shows the comparison of pressure coefficients obtained along the spanwise line at $x/C = 0.5$. Compared to the base wing results both curves attained a more hump like behavior, which is more obvious in the experimental results, indicating the regained lift generating capability. There is considerable shift between the results with the maximum deviation being 25%. The peak seen in the current result is due to the bleeding holes, which is not seen in the experimental results because no data is collected there.

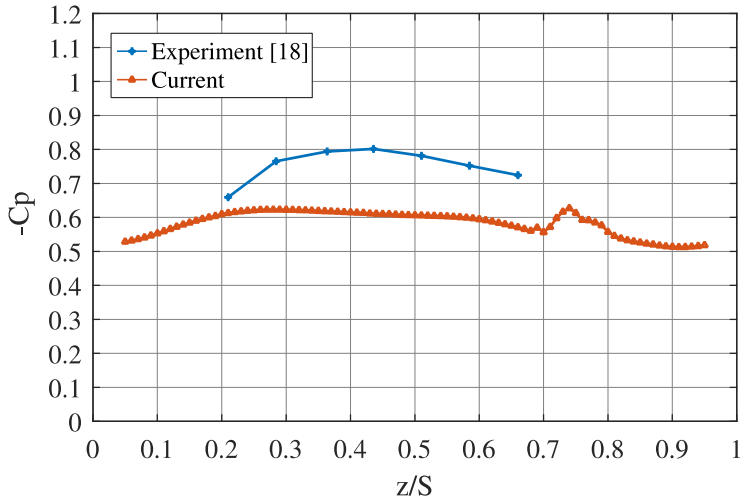

Figure 4-6. Pressure Coefficient Comparison for the Base Wing at $\alpha = 18°$

It is very important that the simulation model can capture flow physics under different conditions. Figure 4-7 shows a comparison of the base wing pressure coefficient at a low attack angle. It is seen that the vortical structure observed at low attack angles can be captured. Similar vortical structure can be recovered at high attack angles by bleeding application. In this context, it can be said that the simulation model is capable of capturing the vortical structure recovered by bleeding application.

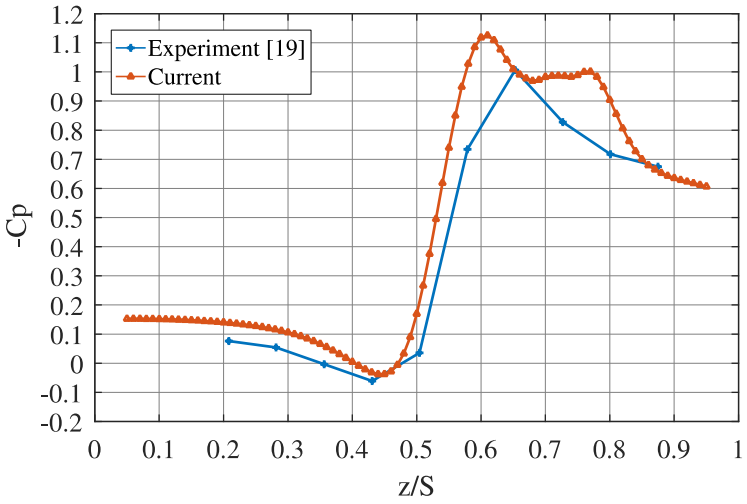

Figure 4-7. Pressure Coefficient Comparison for the Base Wing at $\alpha = 6°$

When the pressure coefficient curves of all cases compared for validation are examined, it is noteworthy that the surface pressure distribution at low angles of attack matches the experimental data better. As the angle of attack increases, the deviation between experimental and numerical results increases up to 25%. One of the main reasons for this deviation is the turbulence model used. Although RANS turbulence models can capture the general physics of the flow around the delta wing [42,46], they are inherently unable to capture local details within the flow. Therefore, compared to advanced turbulence models such as DES, they are particularly insufficient to capture surface pressures [41].

4.3. Sensitivity of the Results

In the comparison of the numerical results and the experimental results performed in the validation study, the flow fields for both the base wing and the bleeding wing are in general found to be similar. It is important to note the following details when comparing the results:

- Taking PIV measurements on planes parallel and very close the wing surface is a challenging task. Adjusting the distance to the surface has its own uncertainty, and dispersion of the laser beam as it travels is known to affect the results. To illustrate how the streamlines depend on the distance to the wing surface Figure 4-8 shows them for the bleeding wing at $\alpha = 17°$ taken from surfaces at three different distances. These are numerical results and no such experimental comparison is available. The differences are especially noticeable close to the apex. The vortex core is not visible for 0.5 mm results. In addition, as the plane moves away from the wing, the vortex core moves away from the apex. The 2 mm increase in the distance of the plane to the surface causes the vortex core to shift to about 7 mm, which shows that the vortex core location is highly sensitive to the distance from the surface. This sensitivity and the fact that laser thickness in PIV measurements can reach 2 mm need to be considered when comparing the results.

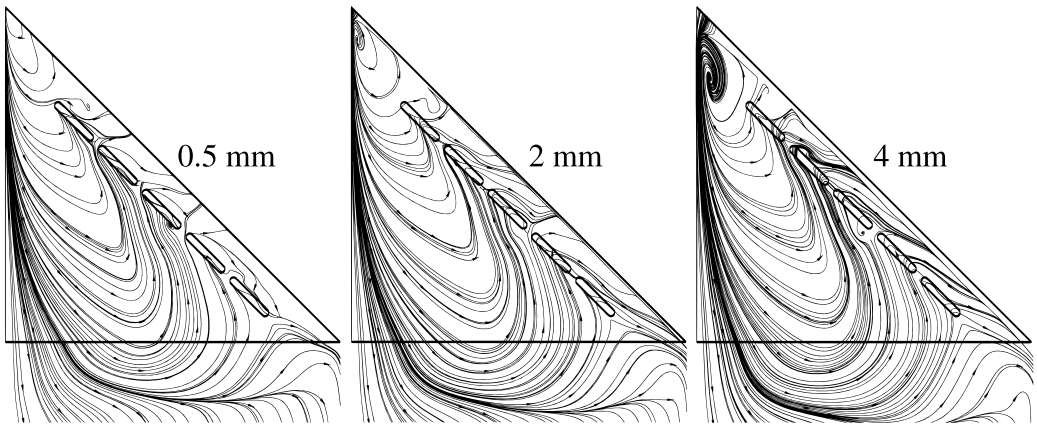

Figure 4-8. Streamlines 0.5, 2 and 4 mm Away from the Top Surface of the Bleeding Wing at $\alpha = 17°$

In both the experiments and the simulations, it was observed that the flow field is sensitive to the angle of attack, which during an experiment can only be set to the desired value within a certain amount of uncertainty. To demonstrate this,

- Figure 4-9 shows the numerically obtained near-surface streamlines of the bleeding wing at three different angles of attack. There are noticeable changes, especially when the angle increases from 16^o to 17^o. Bleeding holes seem to be more effective in lower angles of attack. Similar findings are also seen in the comparison of the pressure coefficient curves given in Figure 4-10. Although the curves for 17 and 18 degrees are similar and flat like, the one for 16^o is very typical of a case with the desired vortical structure.

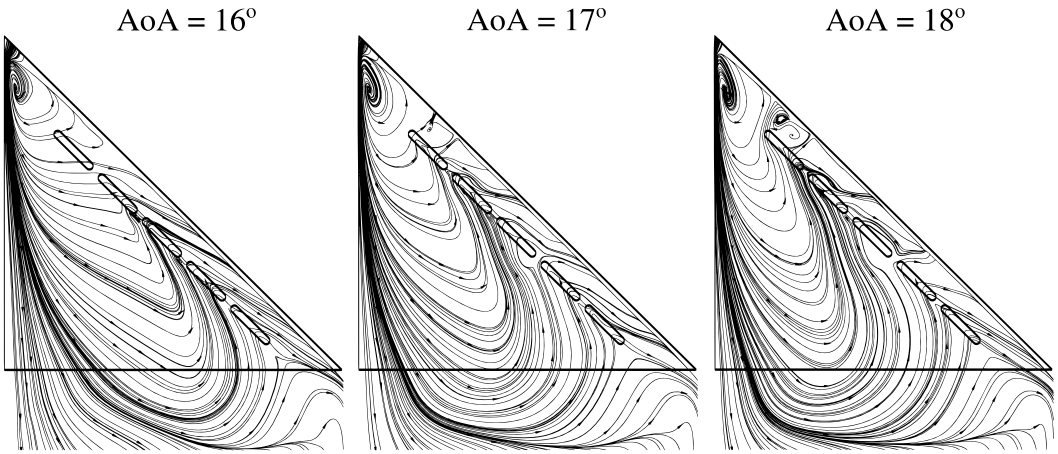

Figure 4-9. Streamlines 3 mm Away from the Top Surface of the Bleeding Wing at Different Angle of Attacks

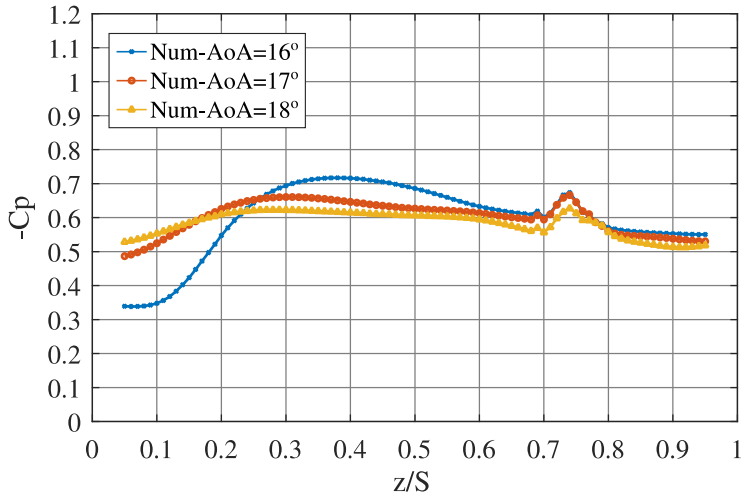

Figure 4-10. Pressure Coefficient Comparison for the Bleeding Wing at $\alpha = 6°, 17°$ *and* $18°$

Other than the above-mentioned sensitivities there are other factors which may cause differences in the experimental and numerical results. One is the problem domain used in the simulations and the boundary conditions being not the same as those used in the experiments. In the experiments, the blockage ratio was checked to make sure that wall effects are minimized, whereas in the simulations the outer box surrounding the wing is selected to be large enough not to affect the flow field close to the wing. Another factor is that the wings used in the experiments have a certain surface roughness associated with the manufacturing technique. However, surfaces are considered to be perfectly smooth in the simulations. Other geometrical differences that are hard to make identical, such as the sharpness of the leading edge, may also affect the results.

CHAPTER 5

RESULTS OF NEW BLEED HOLE DESIGNS

In this chapter, different bleed hole designs that were discussed in Chapter 3 will be simulated to see how they perform in enhancing the flow field characteristics at high angles of attack (AoA). Designs to be tested are the following ones;

Reference Bleeding Wing (RBW): This is the one with 5-holes all having $\theta = 18°$ back angle that was already used in Chapter 4 for validation. It is called the reference design because it had already been tested in earlier studies and the results of other designs will be compared against this one.

Design 1: This one is similar to the RBW, but with $\Omega = 5.5°$ yaw angle.

Design 2: This one is similar to Design 1, but the back angles of the holes vary from 26^o to 18^o gradually.

Design 3: This one is similar to RBW, but all the holes are combined into one big slot, giving us the fully open configuration.

Design 4: This one is similar to Design 3, but with $\Omega = 5.5°$ yaw angle.

Table 5-1 summarizes these different designs.

Table 5-1. Designs to be Tested

Design No.	Number of holes	Back angle θ in degrees	Yaw angle Ω in degrees
RBW	5	18	0
1	5	18	5.5
2	5	Varies from 26 to 18	5.5
3	1	18	0
4	1	18	5.5

Let's start by comparing the results of RBW and the base wing with no holes. Figure 5-1 - Figure 5-3 show the near-surface, crossflow (at $x/C = 0.5$) streamline and $-u$ zone comparisons. As can be seen in the near-surface results, reverse flow on the wing (the area where u velocity is negative) is reduced by the bleeding application. Objectives of bleeding is to rebuild the vortical structure, contribute to the lift force and move the reattachment line which causes instability away from the wing centerline. Crossflow results show that the vortex core and reattachment line move away from the center of the wing, especially at an angle of attack $\alpha = 16^{o}$. This result shows that bleeding is an effective method to control the flow around the wing. However, it is seen that flow control rate decreases with increasing angle of attack, in other words, bleeding starts to lose its function. This can be seen from the increased reverse flow as the angle of attack increases in near-surface results and from the location of the vortex core approaching the wing's symmetry axis as the angle of attack increases in crossflow results. In addition, Figure 5-4 shows the pressure coefficient curves taken along the spanwise direction at $x/C = 0.5$ plane. The curves become flat with increasing angle of attack, and the hump, which is a characteristic of the vortical structure is lost.

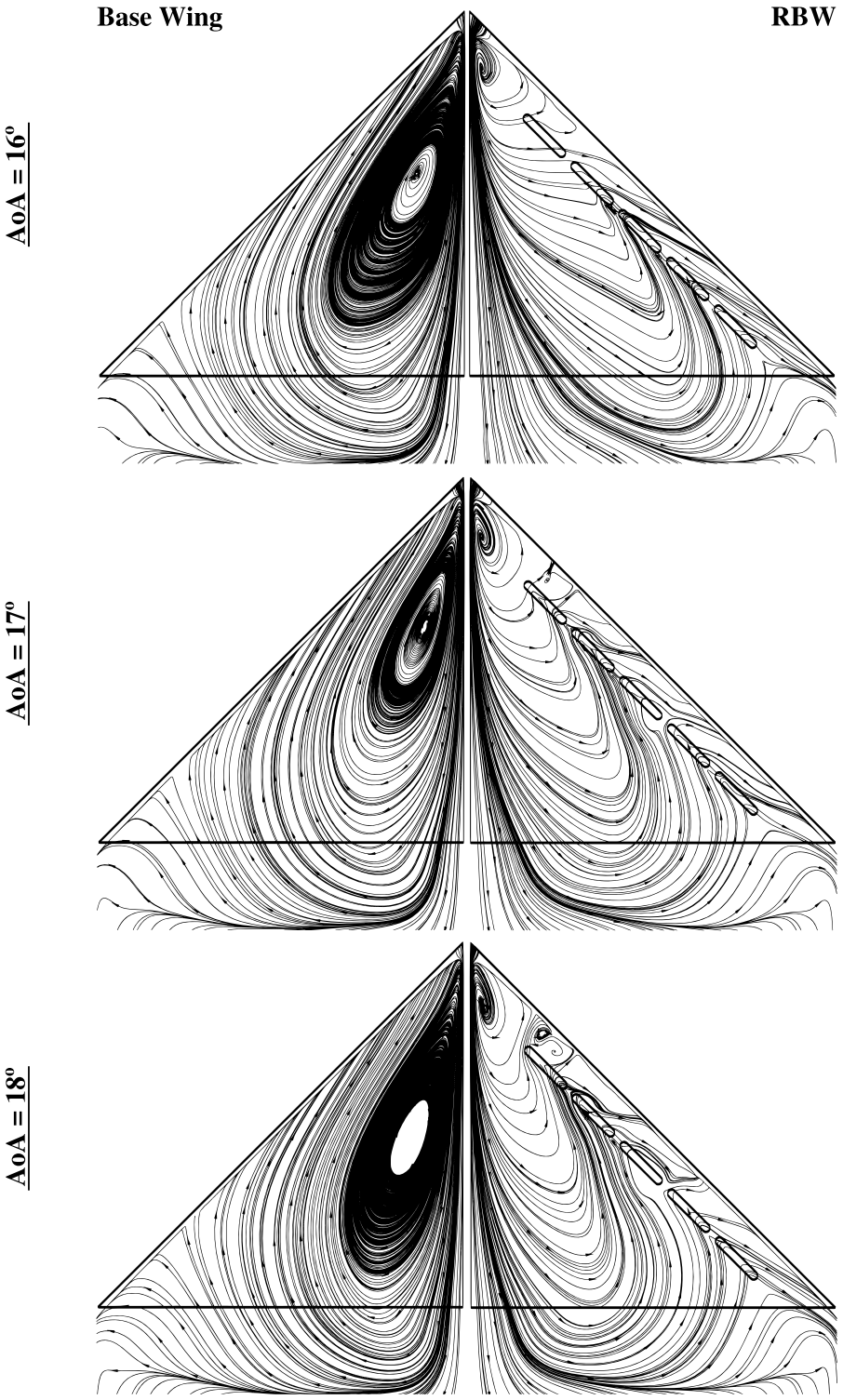

Figure 5-1. Streamlines on the Plane 3 mm Away from Top Surface at $\alpha = 16°, 17°$ and $\alpha = 18°$

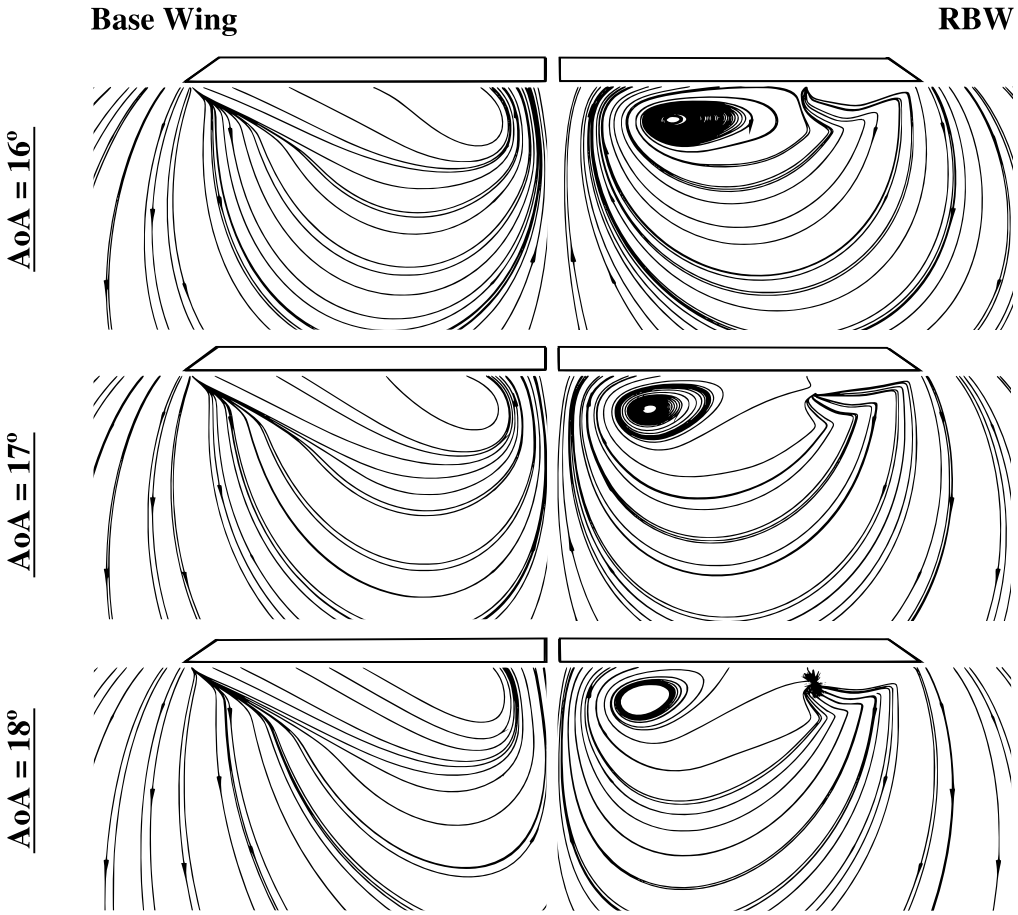

Figure 5-2. Comparison of Cross Plane Streamlines for the Base Wing and RBW at $\alpha = 16°, 17°$ and $\alpha = 18°$

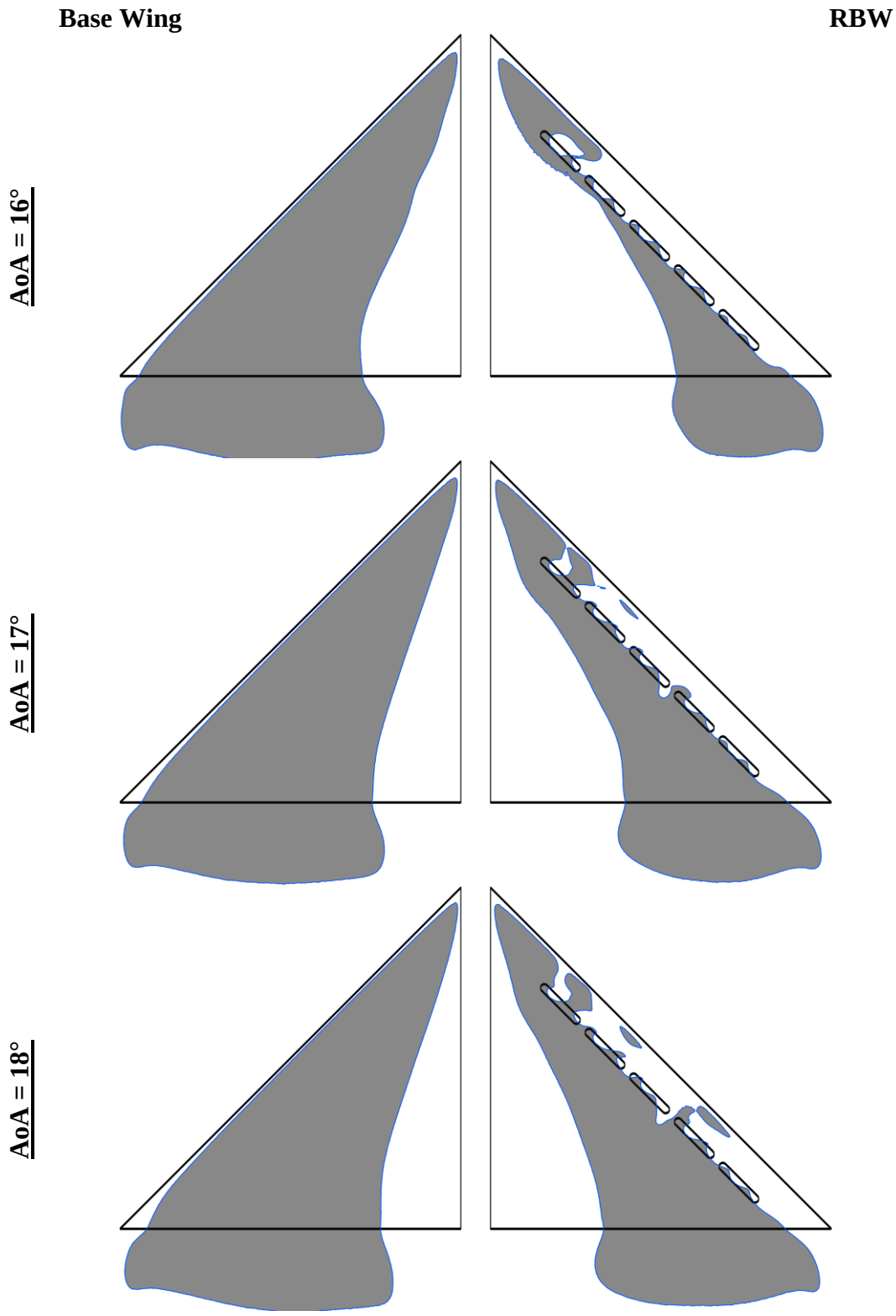

Figure 5-3. $-u$ Zone Contour on the Plane 3 mm Away from Top Surfacen of Base Wing and RBW. Gray Color Shows Negative u Zones

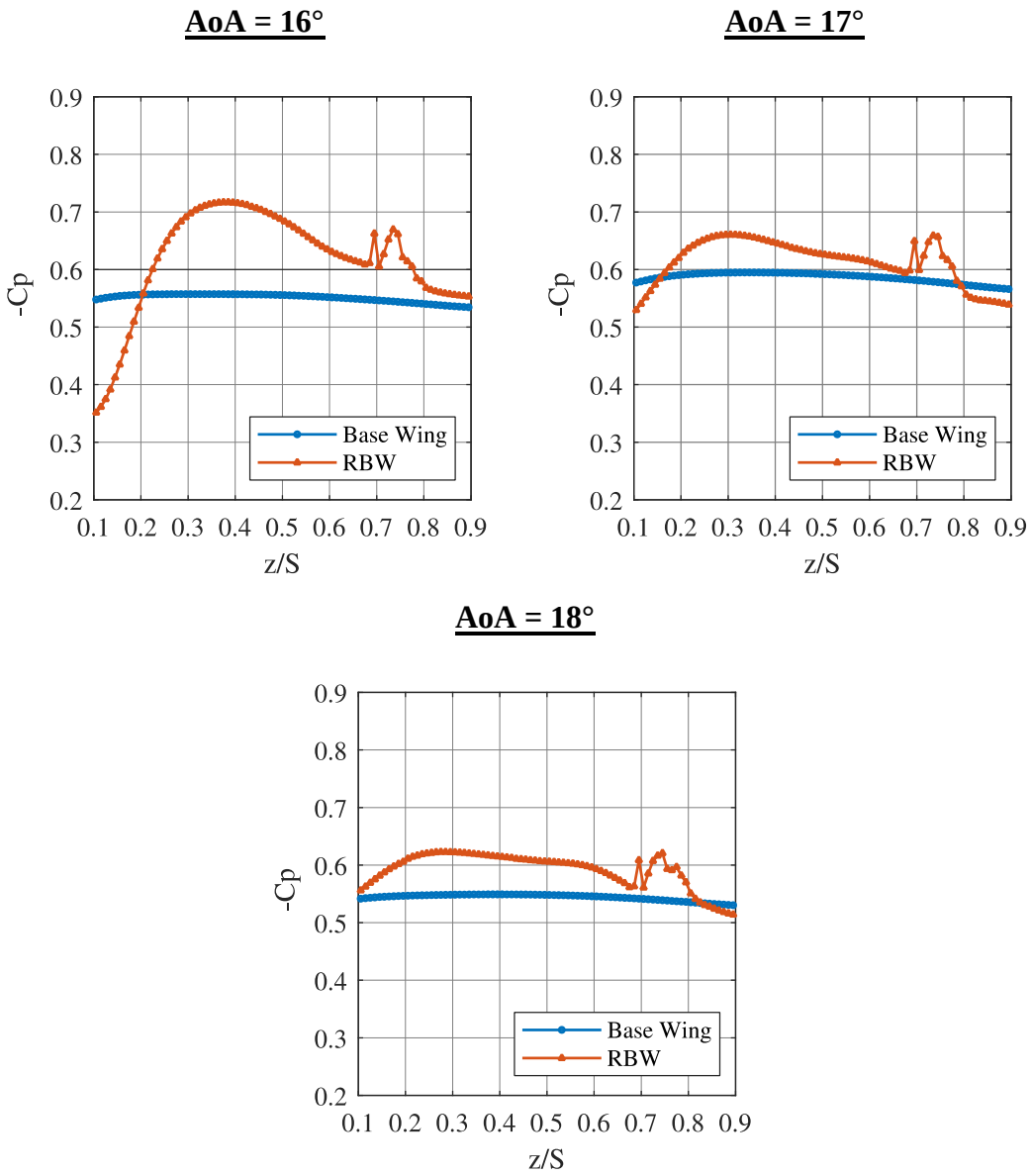

Figure 5-4. Pressure Coefficient Distributions of the Base Wing and RBW

As seen above, the RBW loses its performance as the AoA increases. In the remainder of the chapter, results obtained by the newly proposed four design will be compared with those of the RBW. After discussing all proposed deigns, with the one that has the highest positive impact on the flow field will be selected.

5.1. Design-1: 5 Bleed Holes Delta Wing with 5.5° Yaw Angle

In the RBW, bleed holes are positioned parallel to the leading edge. The main reason why RBW is designed in this way is that the design is based on the blowing method from the leading edge. In RBW design, it is aimed that the blowing effect from the leading edge can be achieved without the need for energy. This application was successful in recovering the lost lift generating capability at relatively low AoA but becomes ineffective as the AoA increase to higher values. The main reason for this is that the vortex core approaches to the wing's centerline with increasing AoA, in other words, it's getting away from the bleed holes. Therefore, energizing the vortex using the flow through the bleed holes becomes difficult with increasing AoA. The overcome this, the yaw angle **Ω**between the bleeding holes and the leading edge is used as discussed in Chapter 2. This way the holes are shifted more towards the vortex core. Design 2 modifies the RBW design is by using a yaw angle of $\Omega = 5.5°$. In Figure 5-5, the near-surface streamline, velocity vectors and $-u$ zones of Design 1 are shown. By comparing the results with RBW, it is seen that at 16^o AoA the flow is enhanced even further, and the reverse flow zone is decreased in size even more. Velocity vectors indicate that the reattachment occurs before reaching the symmetry line. At AoA 18°, it is observed that the design is beginning to lose its effect and near surface streamlines are becoming similar to RBW. Therefore, it can be said that the performance of Design 1 is sensitive to the increase in angle of attack. The crossflow results given in Figure 5-6 are also evidence of these findings. At 16^o AoA, while the reattachment line is away from the centerline and vortical structure is strong (an increase in velocity vector magnitude perpendicular to the wing indicates that the reattachment is strengthened), it approaches to the centerline and vortical structure becomes weak at higher angles of attack. Considering that the characteristic of the desired vortical structure over the delta wing requires reattachment taking place away from the symmetry axis, it is concluded that this design constitutes the targeted vortical structure at 16^o AoA but starts to lose its effect at higher angles, similar to the RBW.

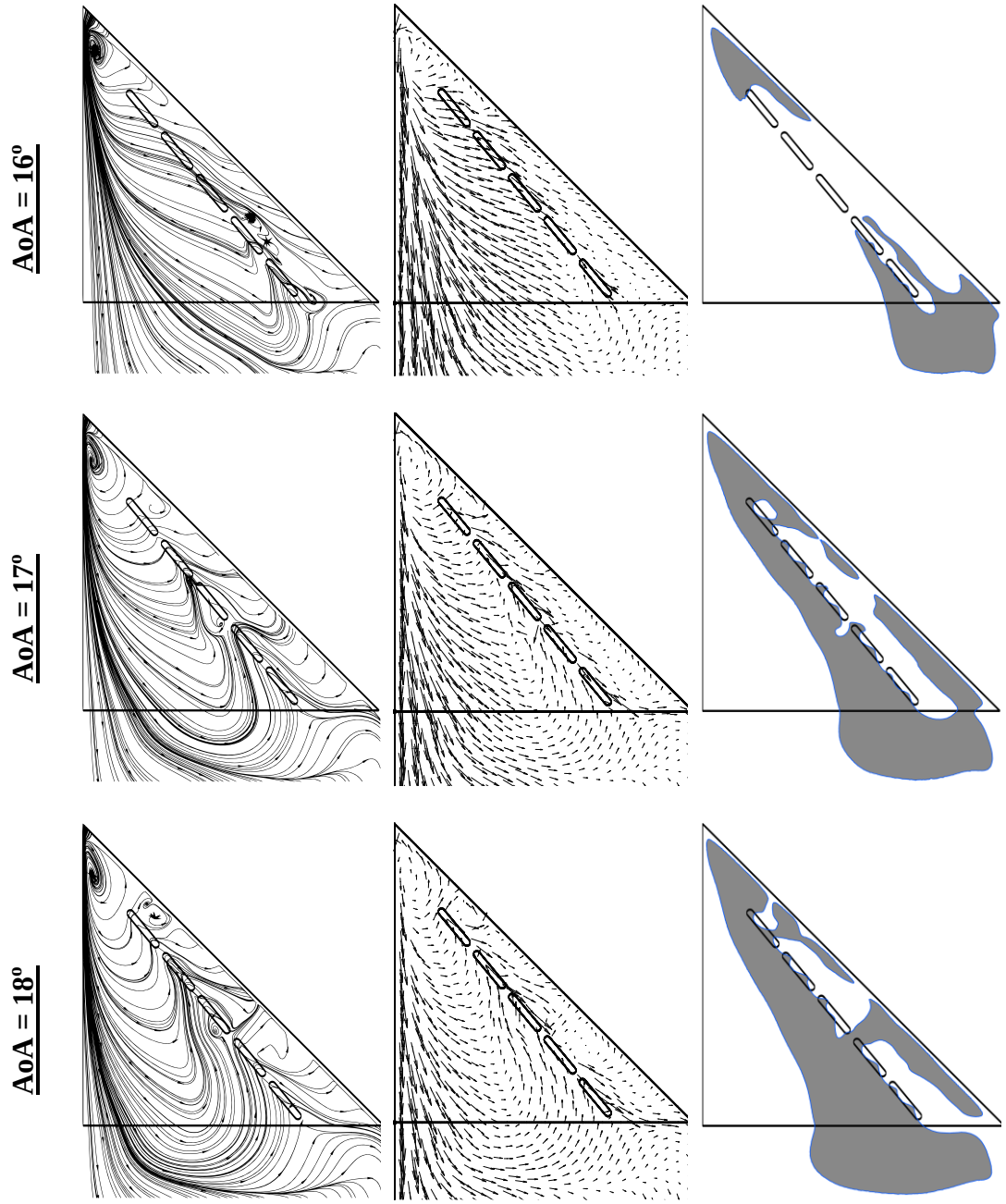

Figure 5-5. Streamlines, Velocity Vectors and *-u* Zone on the Plane 3 mm Away from Top Surface of Design 1

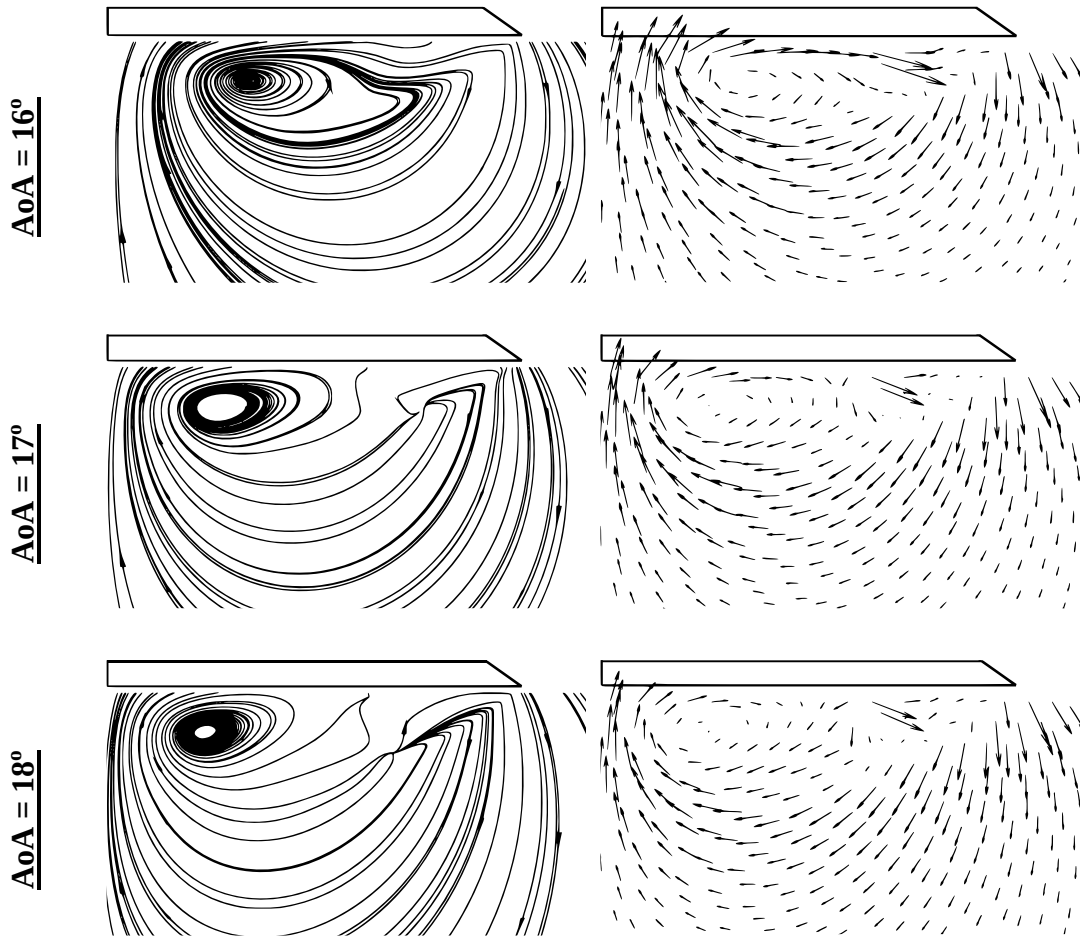

Figure 5-6. Cross Plane Streamlines and Velocity Vectors for Design 1

Pressure coefficients of Design 1 and the RBW are compared in Figure 5-7. The further enhancement of the flow field compared to RBW at 16° AoA is clearly seen in this figure. The C_p distribution is curved more, which is desired, and the difference between the minimum and maximum C_p values increased. These enhancements can barely be seen for 17° and there is no noticeable improvement for 18°. The flattening of the C_p curve with increasing AoA indicates deterioration of the vortical structure as discussed above.

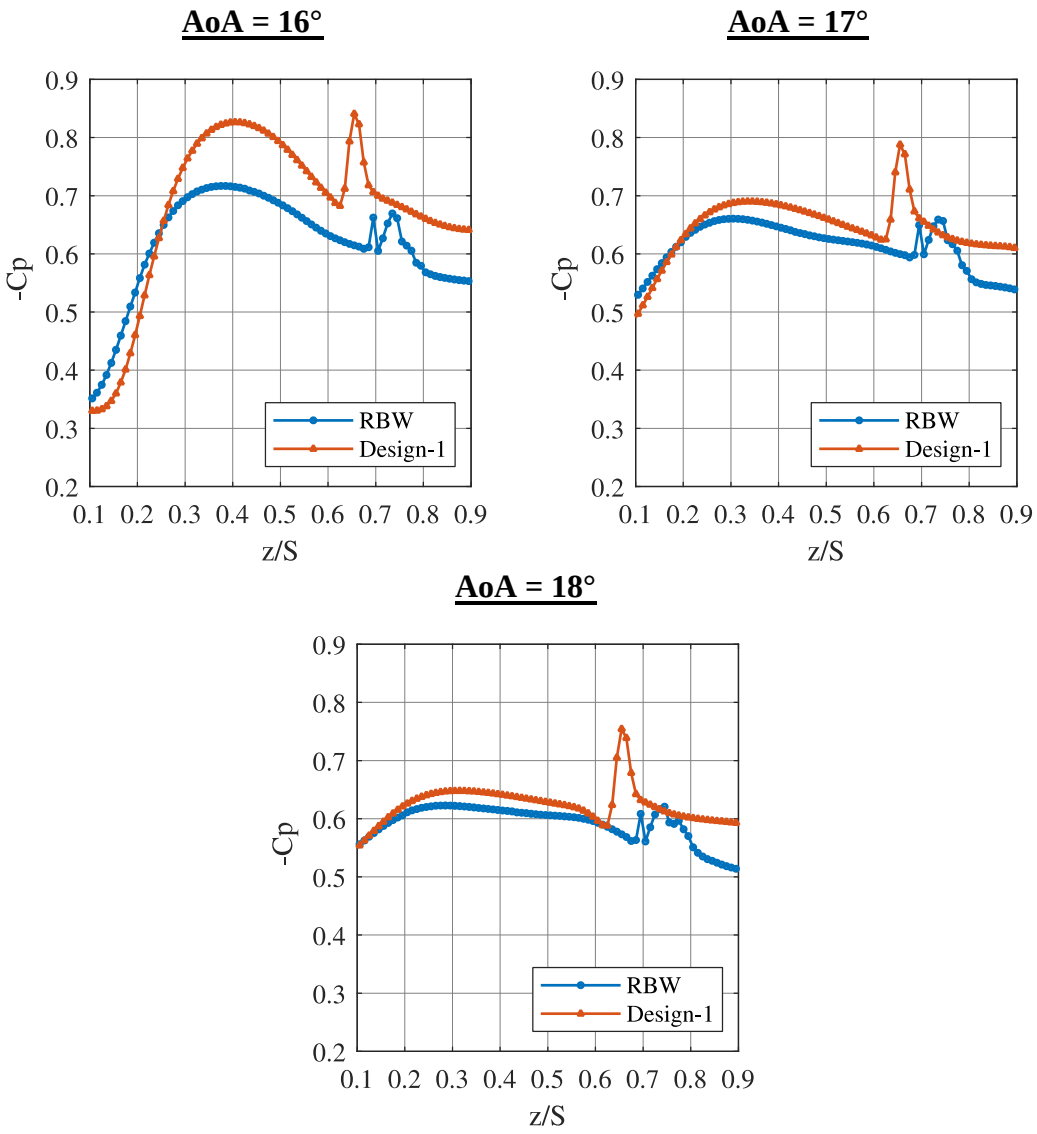

Figure 5-7. Pressure Coefficient Distribution at Half Chord of Design 1

5.2. Design 2: 5 Bleed Holes with Variable Back Angle and 5.5° Yaw Angle

As discussed above RBW and Design 1 enhances the flow field compared to the base wing. However, even at 16^{o} AoA, the reverse flow cannot be prevented close to the apex. It is also noteworthy that bleeding application loses its effect near the trailing edge. These findings raised the question regarding the level of impact each hole has on the flow control. An auxiliary study, details of which are not shared here, is performed to better understand the flow structure and to see the effect of the holes on

the flow. The first and the last holes are closed one-by-one and these two cases are analyzed separately. It is found that the first hole had the greatest effect in reducing the reverse flow and establishing the desired vortical structure. In case the first hole is closed, the flow field becomes similar to that of the the base wing and the other holes are not sufficient to control the flow. In the case where only the last hole is closed, the flow field is highly similar to that of the RBW. This situation shows that the last hole has a minimal effect on flow control. Therefore, the second design focuses on the role of the first hole and aims to maximize its contribution. In this context, it is thought that bringing the exit of the first hole closer to the apex will perform better. However, due to the fact that the entrance of the first hole on the pressure side of the wing is already very close to the beveled edge, it was not possible to shift it as desired. To overcome this, the back angles of the holes are increased gradually towards the apex, and they are shifted closer to the apex as much as possible.

In Figure 5-8, near-surface streamlines, velocity vectors and $-u$ zones of Design 2 are given. At all AoA, compared to Design 1, reverse flow is reduced in the area between the holes and the wing's axis of symmetry. However, the small increase in velocity vector magnitude near the symmetry axis indicates that the reattachment is strengthened. On the other hand, the reverse flow region, which is near apex, the main target of design, is observed to shrink especially at 16° and 17° AoA. In addition, in the region between the holes and the leading edge, it is noted that the -u velocity contours are formed in a fragmented manner. This can be particularly explained by the small swirls generated between the holes and the leading edge at 18° AoA. In the crossflow results shared in Figure 5-9, the vortex core location appears to be very similar to Design 1. However, there is an increase in velocity vector magnitude in the region close to the axis of symmetry, and the reattachment is strengthened accordingly. When the C_p graphs given in Figure 5-10 are examined, it is seen that the hump on the curve is more evident than it is in Design 1 at $\alpha = 17°$ and 18°, indicating stronger vortical structures. The ability to create a vortical structure, especially at 16° and 17° AoA, is one of the strong features of the design.

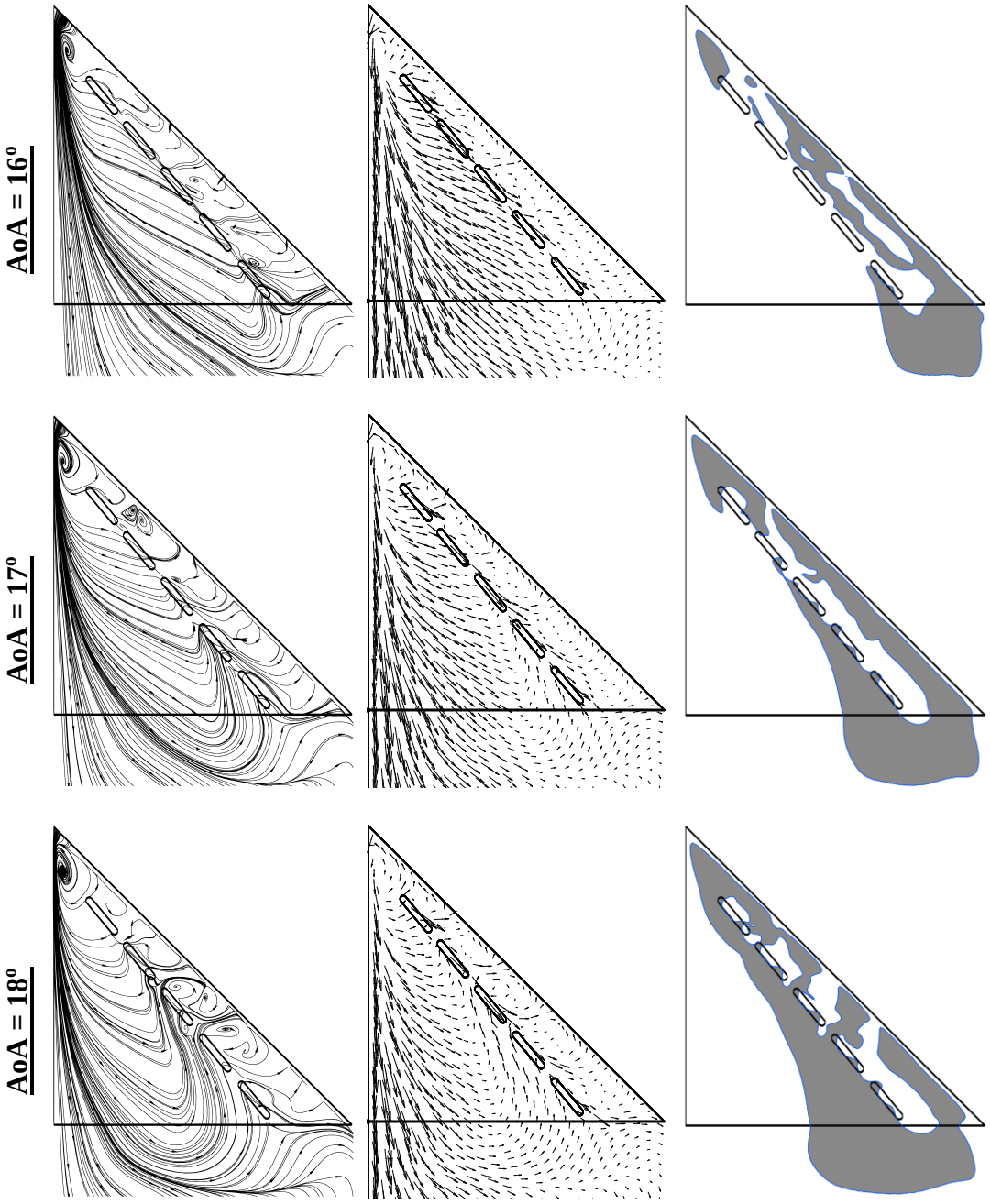

Figure 5-8. Streamlines, Velocity Vectors and -*u* Zone on the Plane 3 mm Away from Top Surface of Design 2

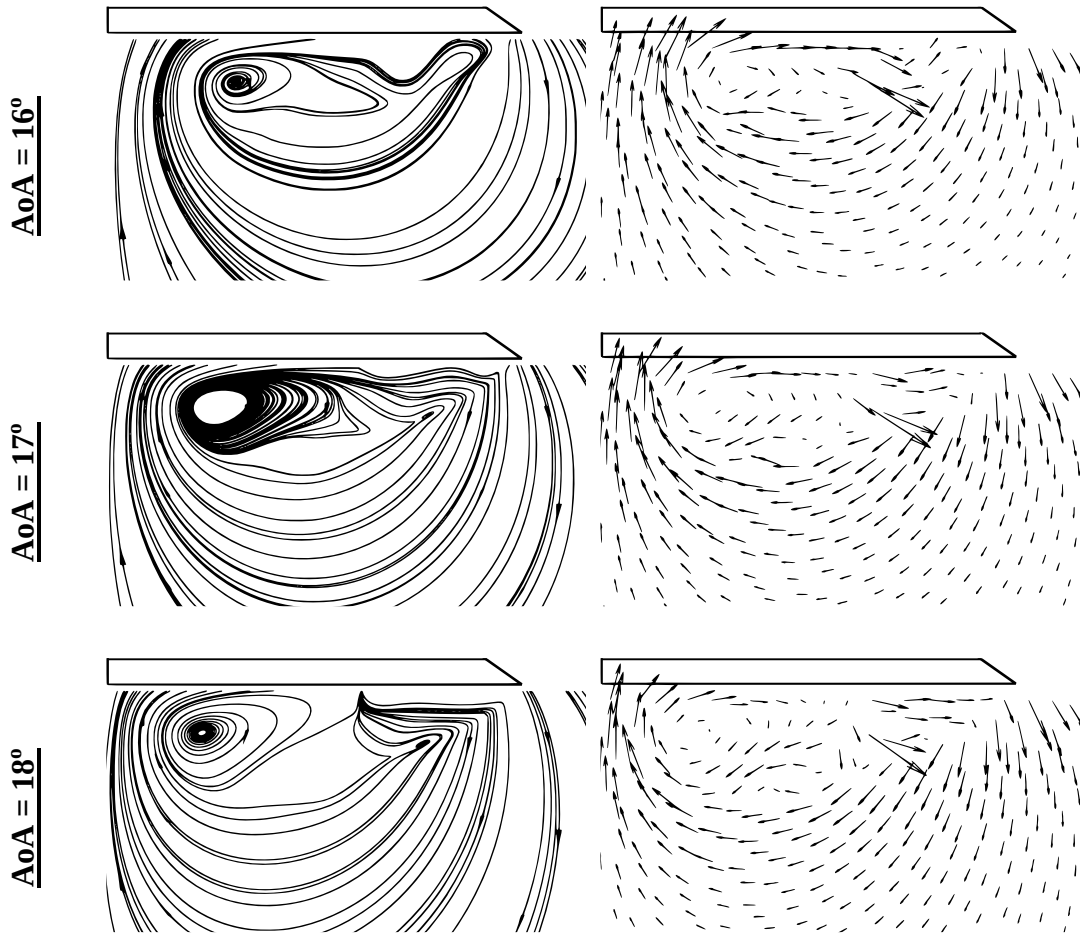

Figure 5-9. Cross Plane Streamlines and Velocity Vectors for Design 2

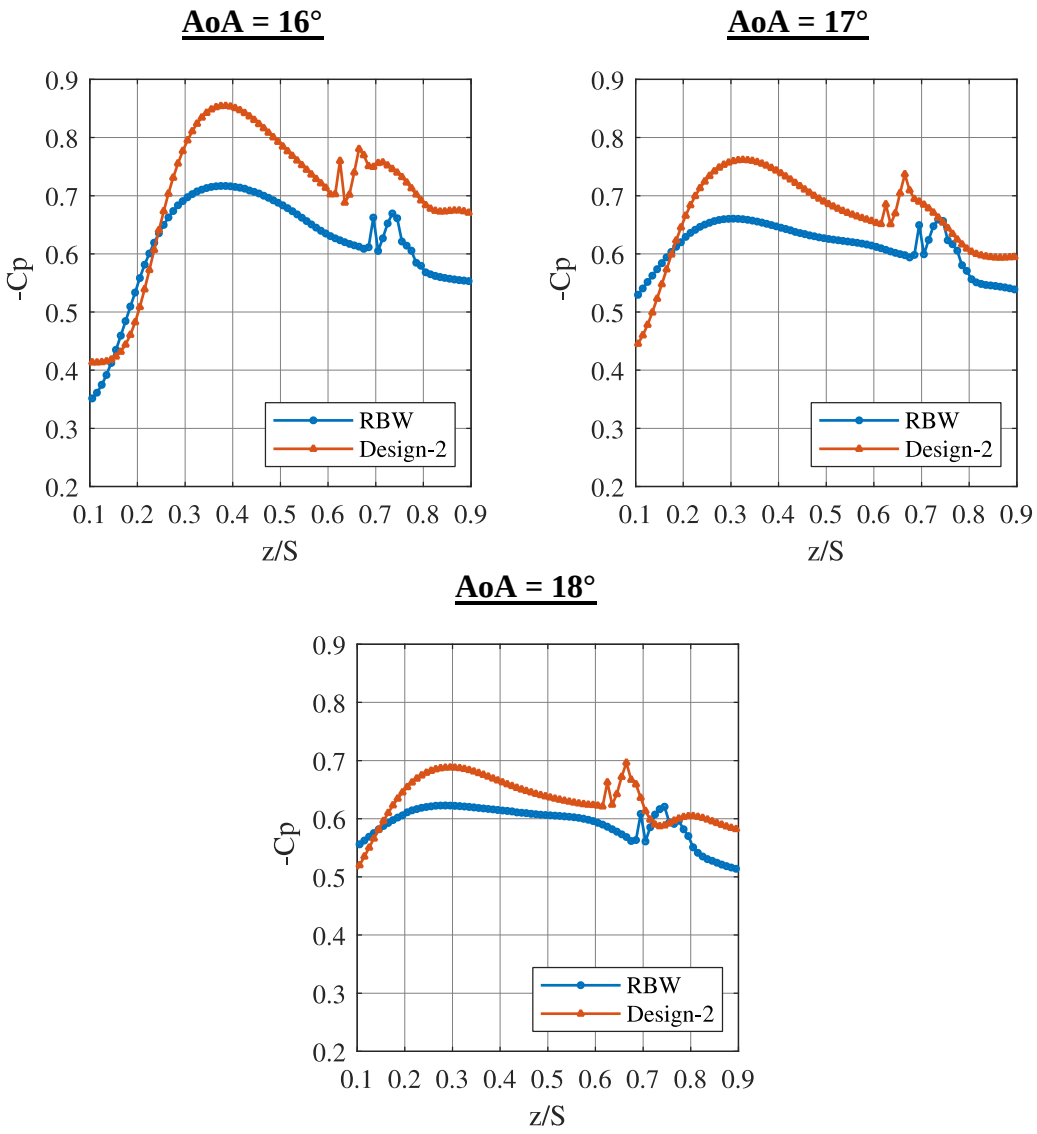

Figure 5-10. Pressure Coefficient Distribution at Half Chord of Design 2

5.3. Design 3: Full Open Bleed Hole

The main difference between bleeding and blowing is that the bleeding method is a passive method that uses the pressure difference between the upper and lower surfaces of the wing. On the other hand, blowing is a method that gives momentum to the flow by using energy. Naturally, the flowrate passing through the holes in the bleeding case is less than of blowing. The performance of bleeding can be increased by increasing the flow rate with the increase in the hole size. For this reason, the 5 holes in the RBW are combined into a single one. As a result of this design change, the flow rate through the hole has increased up to 110%

Results of Design 3 are shared in Figure 5-11 - Figure 5-13. It is observed that the performance of the wing with a fully open single hole is not very much different from that of the RBW, especially at 16^{o} AoA. However, when we compare Design 3 with Design 1 and Design 2, it is seen that Design 1 and Design 2 are more effective in reducing reverse flow at 16° AoA. When AoA increases, the crossflow results show that the vortex core location is farther from the wing's symmetry axis compared to RBW, Design 1 and Design 2. In addition, near surface results show that velocity vector magnitude is larger in the area close to the wing's symmetry axis compared to RBW and Design 1, and thus the reattachment seems to occur stronger. This situation makes fully open hole design more robust than other designs. The change in $-u$ zones with AoA being minimum is an evidence of this finding.

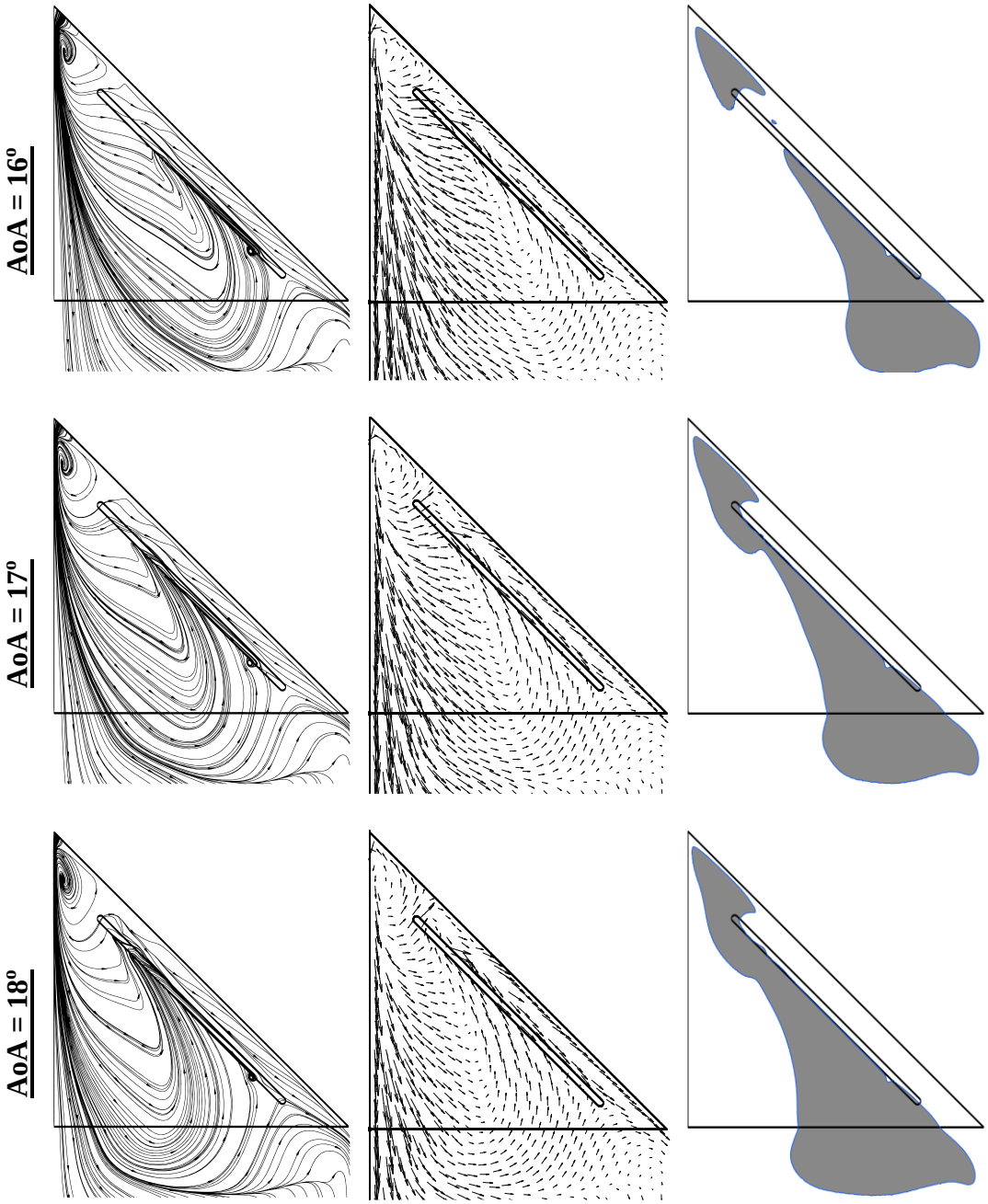

Figure 5-11. Streamlines, Velocity Vectors and *-u* Zone on the Plane 3 mm Away from Top Surface of Design 3

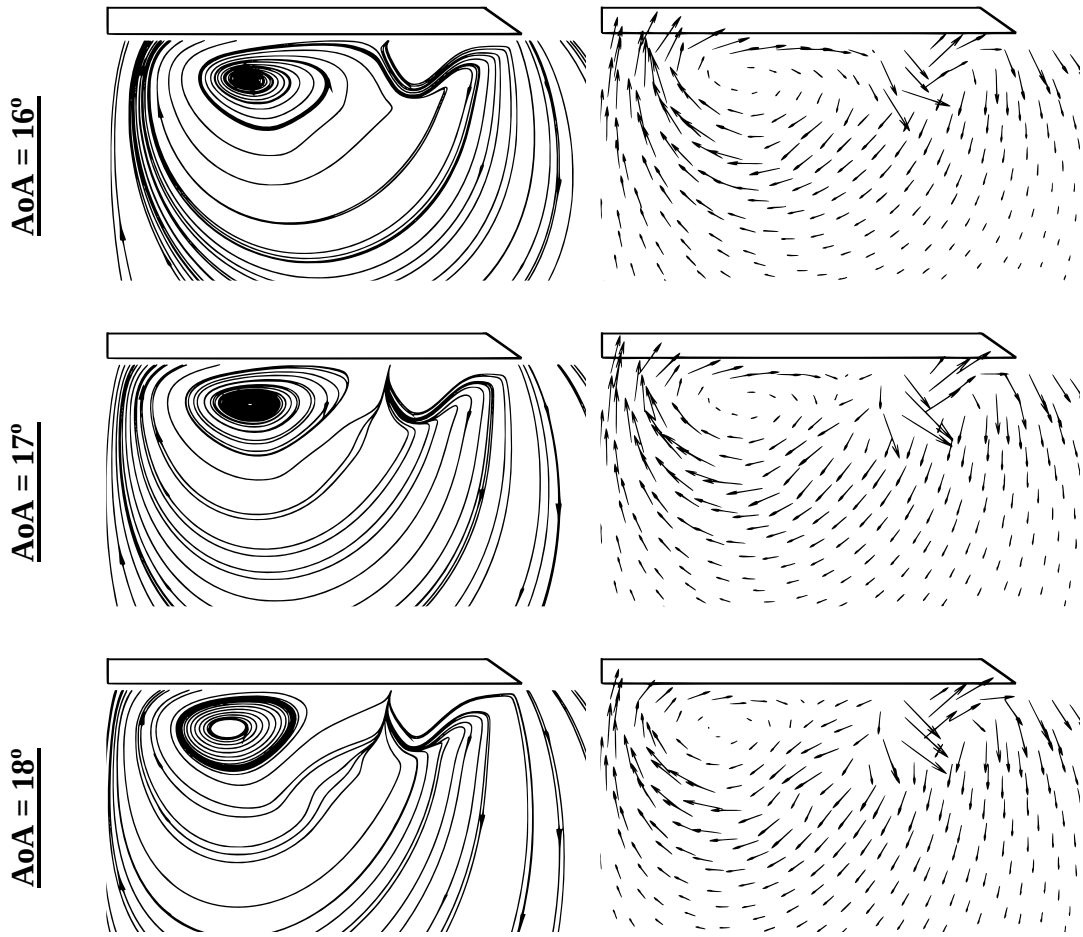

Figure 5-12. Cross Plane Streamlines and Velocity Vectors for Design 3

In Figure 5-13, C_p curves of Design 3 and RBW are compared. At $\alpha = 16^o$, the C_p curve is very similar to that of RBW. As the AoA increases, the C_p curve of the RBW becomes flat, while the curve of Design 3maintains its hump form relatively.

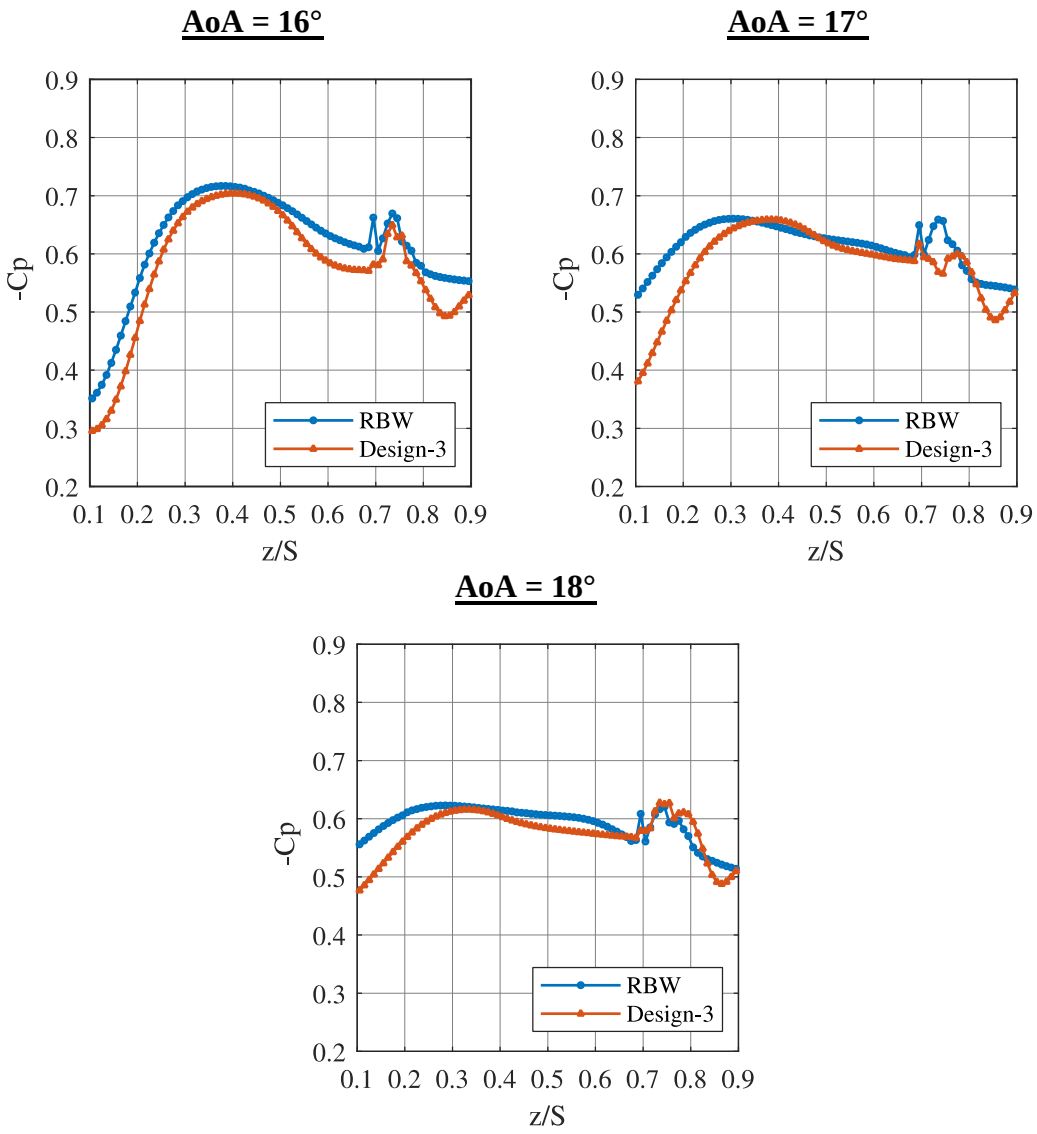

Figure 5-13. Pressure Coefficient Distribution at Half Chord of Design 3

5.4. Design 4: Full Open Bleed Hole with 5.5° Yaw Angle

More advanced flow control is provided in the previously reviewed Design 1 and Design 2 compared to the RBW. Flow control is more effective at lower AoA in Design 1. However, in the fully open bleeding hole design, sensitivity to change in the angle of attack decreases and a robust design emerges. The aim of flow control methods is to create a vortical structure by controlling the flow and to minimize the

sensitivity of the condition change. With the first design, the vortical structure is formed more strongly, and with the third design, the sensitivity to increase of the angle of attack is reduced. For this reason, as the geometric details are given in Chapter 3, **Ω** angle is applied to fully open bleeding hole design and the third design, namely fully open bleeding hole configuration with **Ω** angle design is obtained. The design is simulated at $\alpha = 16^o, 17^o$ and $\alpha = 18^o$, as in other examinations.

Figure 5-14, 5-14 and 5-14 show the results of Design 4. The results at $\alpha = 16°$ are very similar to that of Design 1. In addition, as seen in the u velocity contours, in this new design bleeding remains effective despite the increase in the AoA. This demonstrates that the robust characteristic of fully open bleeding hole design can be combined with the ability of the yaw angled holes to reconstruct the vortical structure. When the near-surface velocity vectors are examined at $\alpha = 18^o$, it is observed that the reattachment line has not yet reached the wing's symmetry axis, showing that the design remains effective at higher AoA. Furthermore, it is noted that swirls do not generate between the holes observed in the 5-hole designs and the leading edge and a smooth flow profile is obtained. Naturally, the flow around the wing has started to exhibit a steadier character compared to other designs. When the crossflow results given in Figure 5-15 are examined, the increase in velocity vector sizes indicates that the reattachment is strengthened. In addition, secondary vortex formation is seen more clearly compared to other designs. In addition, even at high angles of attack, the vortex core location is generated far from the axis of symmetry compared to other designs.

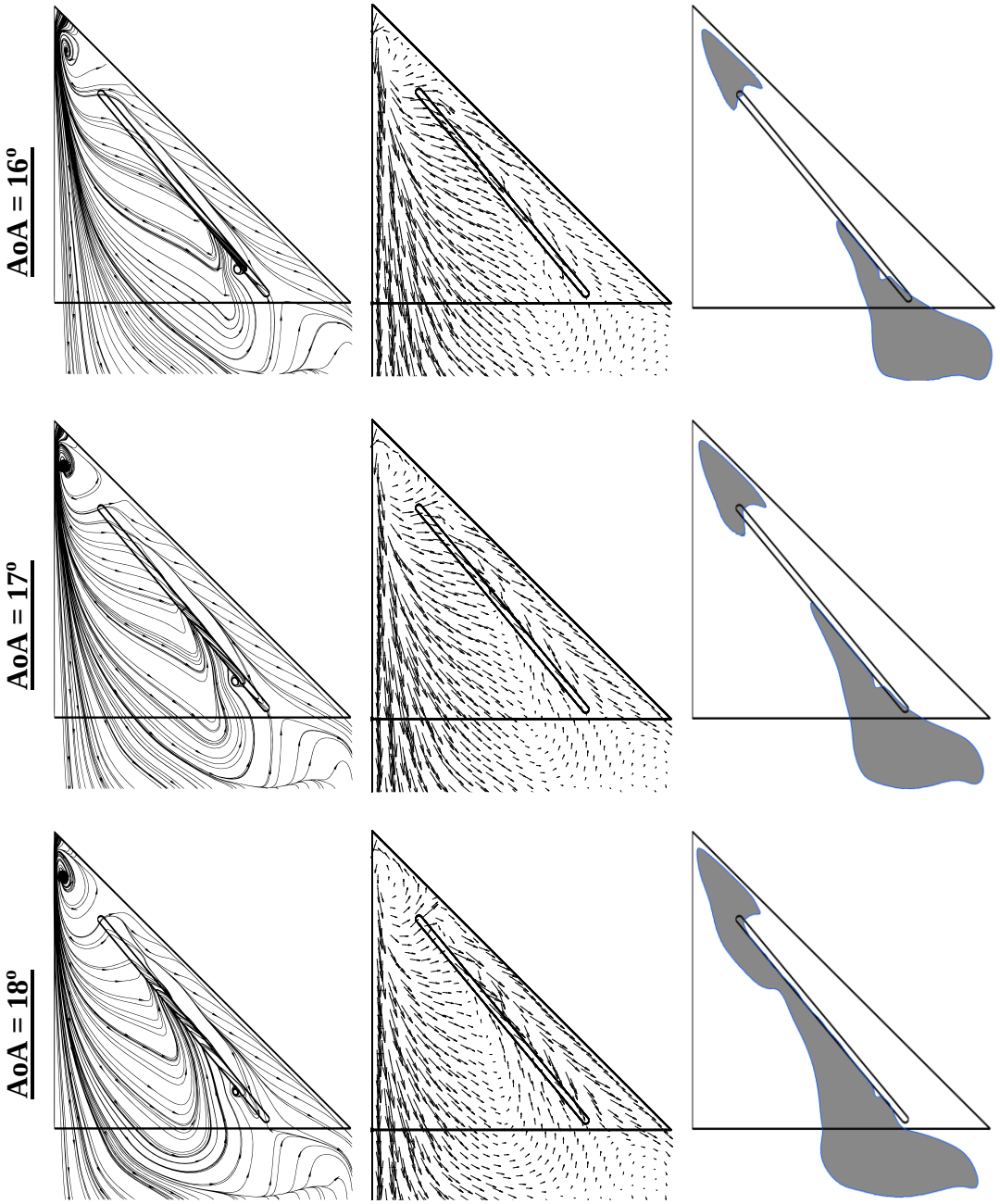

Figure 5-14. Streamlines, Velocity Vectors and *-u* Zone on the Plane 3 mm Away from Top Surface of Design 4

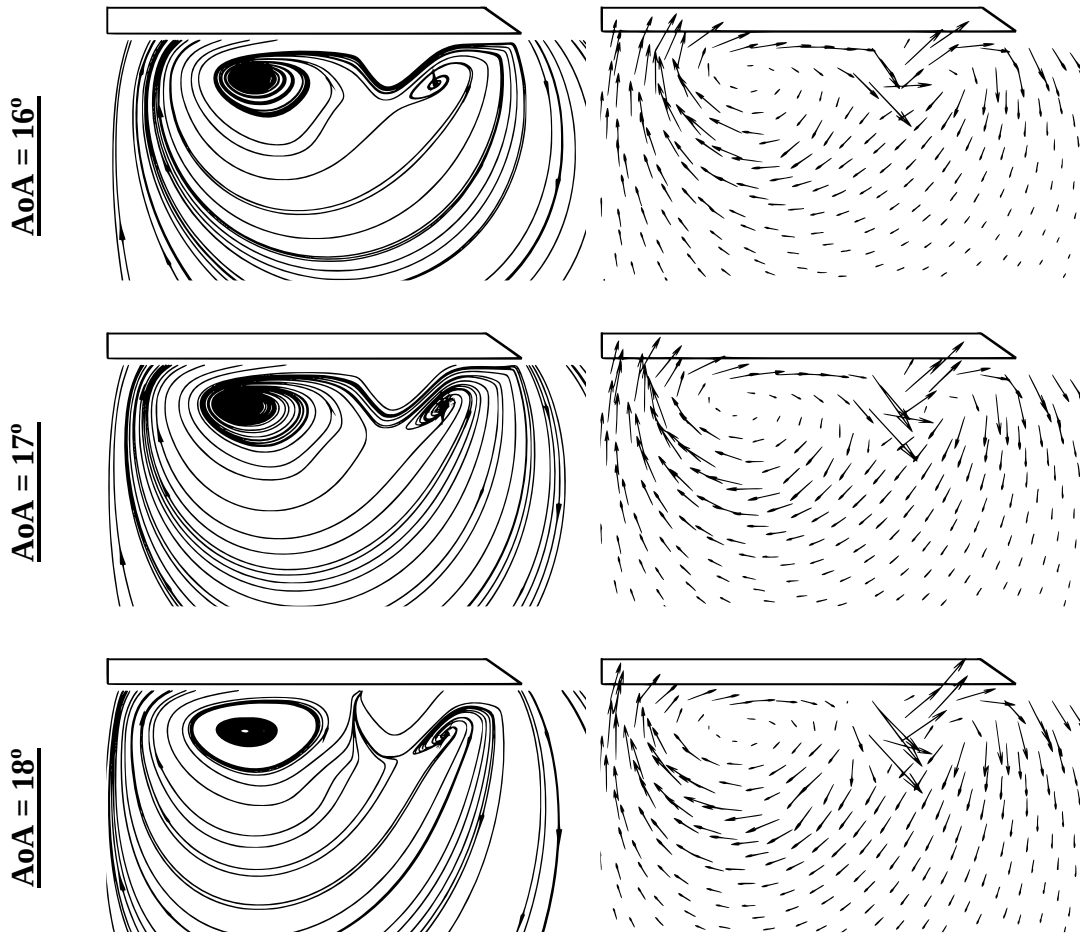

Figure 5-15. Cross Plane Streamlines and Velocity Vectors for Design 4

In Figure 5-16, the C_p curves of Design 4 and RBW are compared These results also go parallel with the previous discussions. The hump like structure seems to be maintained better at higher AoA. When all the results are evaluated, it can be concluded that Design 4 is less affected by the increase in AoA. The decrease of the curve around z/S=0.8 shows that vortex caused by the bleeding holes is more powerful than the other designs.

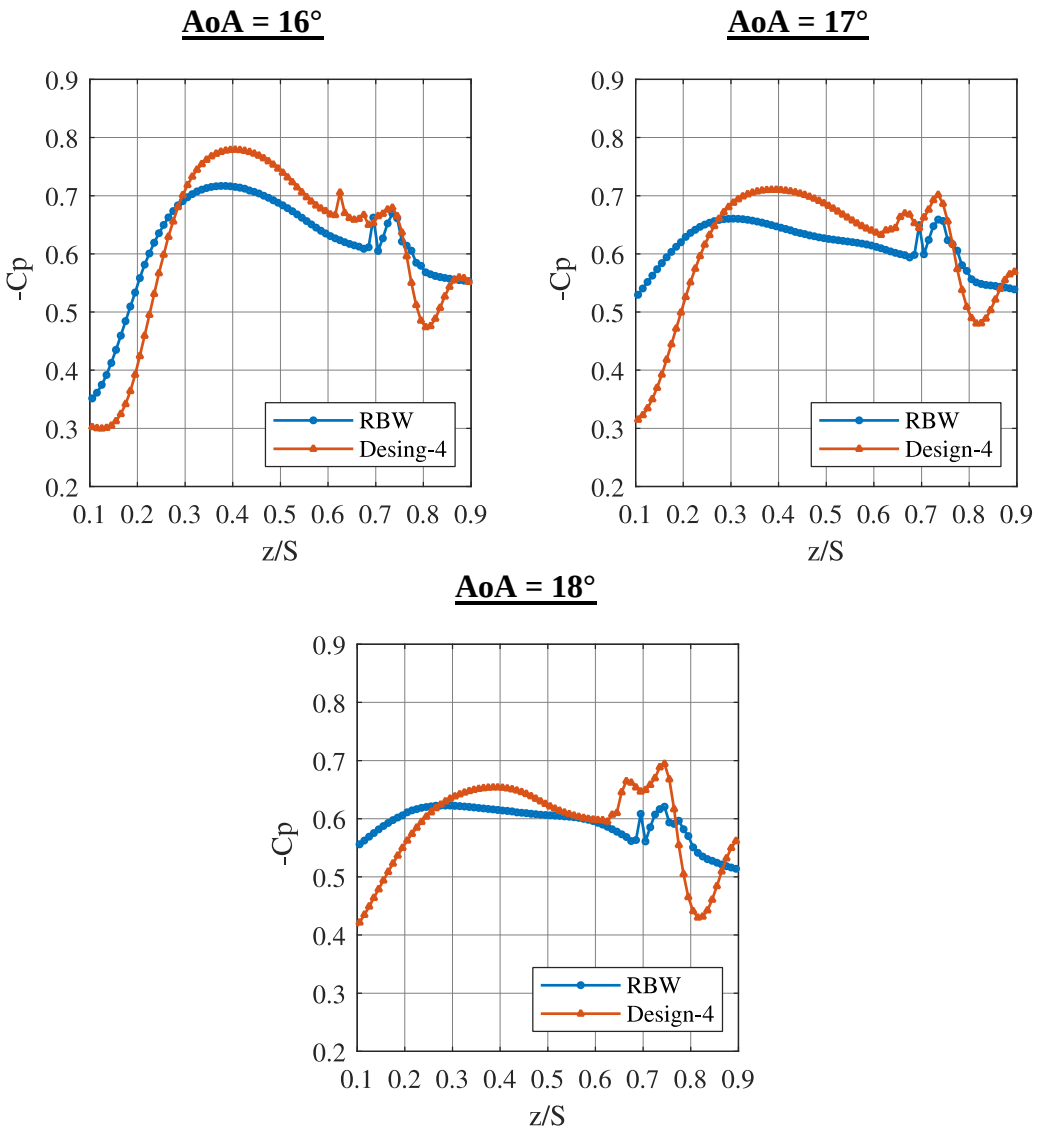

Figure 5-16. Pressure Coefficient Distribution at Half Chord of Design 4

5.5. Overview of All Designs

When all the designs are evaluated, it is seen that almost all of them perform better than the reference bleeding wing. Compared to the RBW, the evaluated four designs had two main differences. The first is the yaw angle defined between the bleeding holes and the leading edge. With this idea, the vortical structure could be created more strongly. However, it loses its advantage at higher angles of attack. The second main

change is combining the holes into a single one with a larger total opening area. With this design, the bleeding method can also be effective at higher AoA. In other words, a design that is more resistant to increase in the AoA is obtained. Combining these two main ideas, Design 4 is the one that provided the best performance/stability balance among others. As also seen in the C_p comparison of all designs given in Figure 5-18, Design 4 provides the best performance both in terms of reconstruction of the vortical structure and provision of stability also at higher AoA. While the humped structure of the C_p curve shows that the vortical structure is able to form, the difference between the maximum and minimum values in the curve shows the strength of the vortical structure, in other words, the performance of the bleeding flow control method. The large difference between the maximum and minimum $-C_p$ values means that the pressure in the core of the resulting vortical structure is lower. Naturally, the contribution to the lift force increases with the increase in the difference between the maximum and minimum $-\mathrm{C_p}$. In Figure 5-17, the top surface $-C_p$ contours at an angle of attack 16°, 17° and 18° are shared for all designs. At α = 16 ° AoA, the minimum $-C_p$ values are observed in the regions of Design 1 and Design 2 close to the wing symmetry axis. However, the maximum $-C_p$ region covers a wider area than other designs. This shows that reattachment occurs stronger than in other designs. However, in Design 3 and 4, the minimum $-C_p$ contours were found to be closer to the apex. This indicates that the reattachment starts in the regions of the wing that are closer to the apex. Although the difference between the maximum/minimum contour levels decreases as the angle of attack increases, there is no major change in the reattachment location between the designs. Design 4, as in other comparisons, is the best design at which the reattachment at angle of attack 18° is strong and far from the axis of symmetry.

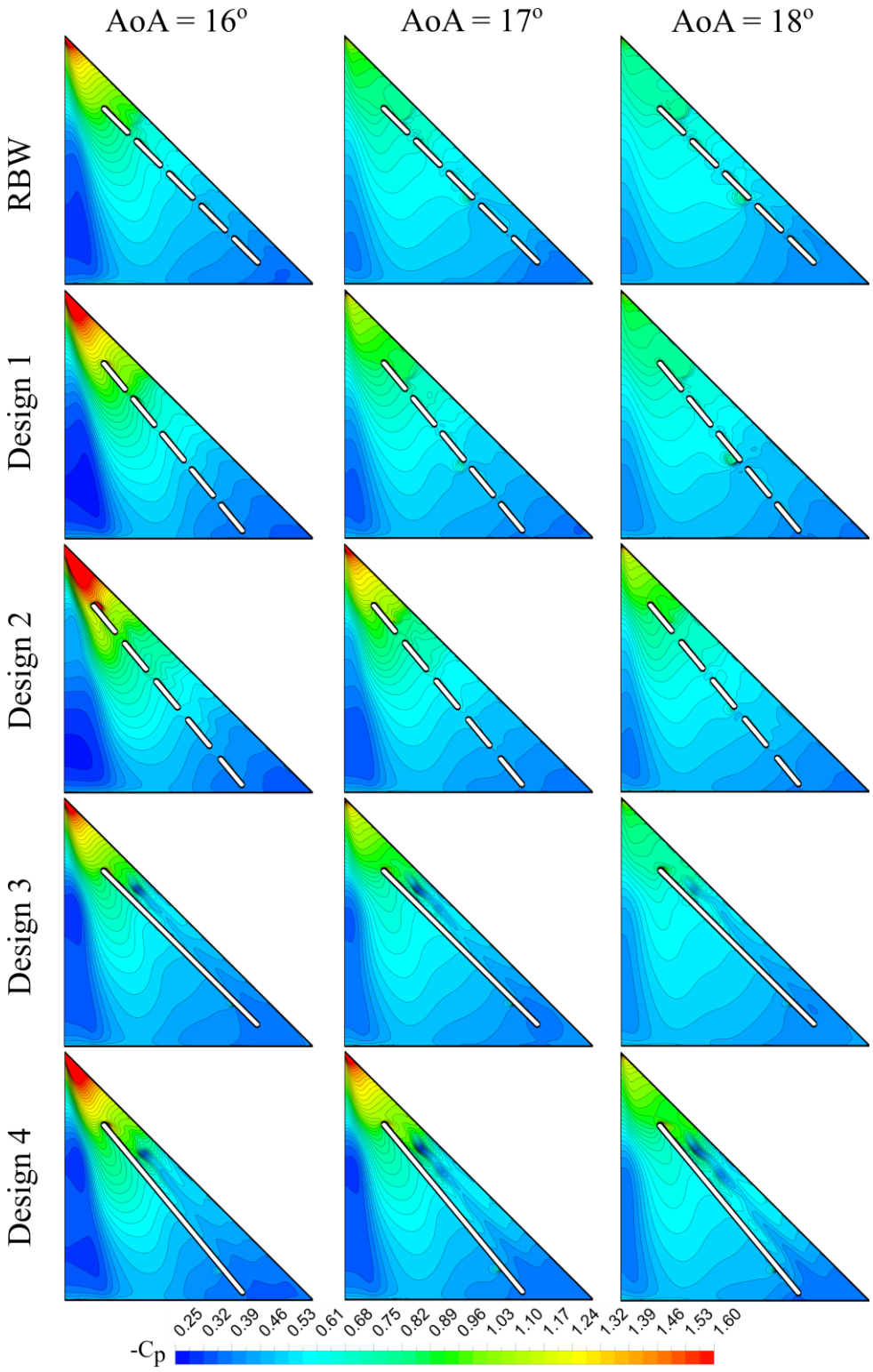

Figure 5-17. Pressure Coefficient Distribution on Wing Surface

In Table 5-2, the minimum and maximum $-C_p$ values of all cases are examined and the differences between these values are reported. The difference between the minimum and maximum $-C_p$ is close to zero since the base wing has an almost flat C_p curve. This means that the vortical structure is lost, with no contribution to the lift force. When the values of RBW and new designs in the table are compared, it can be said that all designs create vortical structures which are about twice or 3 times as strong, especially at higher AoA. When the values at $\alpha = 16^{o}$is examined, it is seen that Design 1 has the best performance. Design 4 also performs similar to Design 1. These findings are also in line with the earlier observations. When $\alpha = 17^{o}$ and 18^{o} cases are examined, it is seen that the effect of Design 1 decreases gradually but the performance of Design 4 is keeps better than the other designs. This shows that Design 4 is an overall more robust design that can maintain its impact even at higher AoA, which is again parallel to previous observations. Additionally, when the spanwise locations at which the curves reach their maximums are examined, it is seen that in Design 4, the vortex is formed at the farthest point from the wing's centerline. This shows that the reattachment line also moves away from the axis of symmetry due to the vortex location moving away from the wing's symmetry axis.

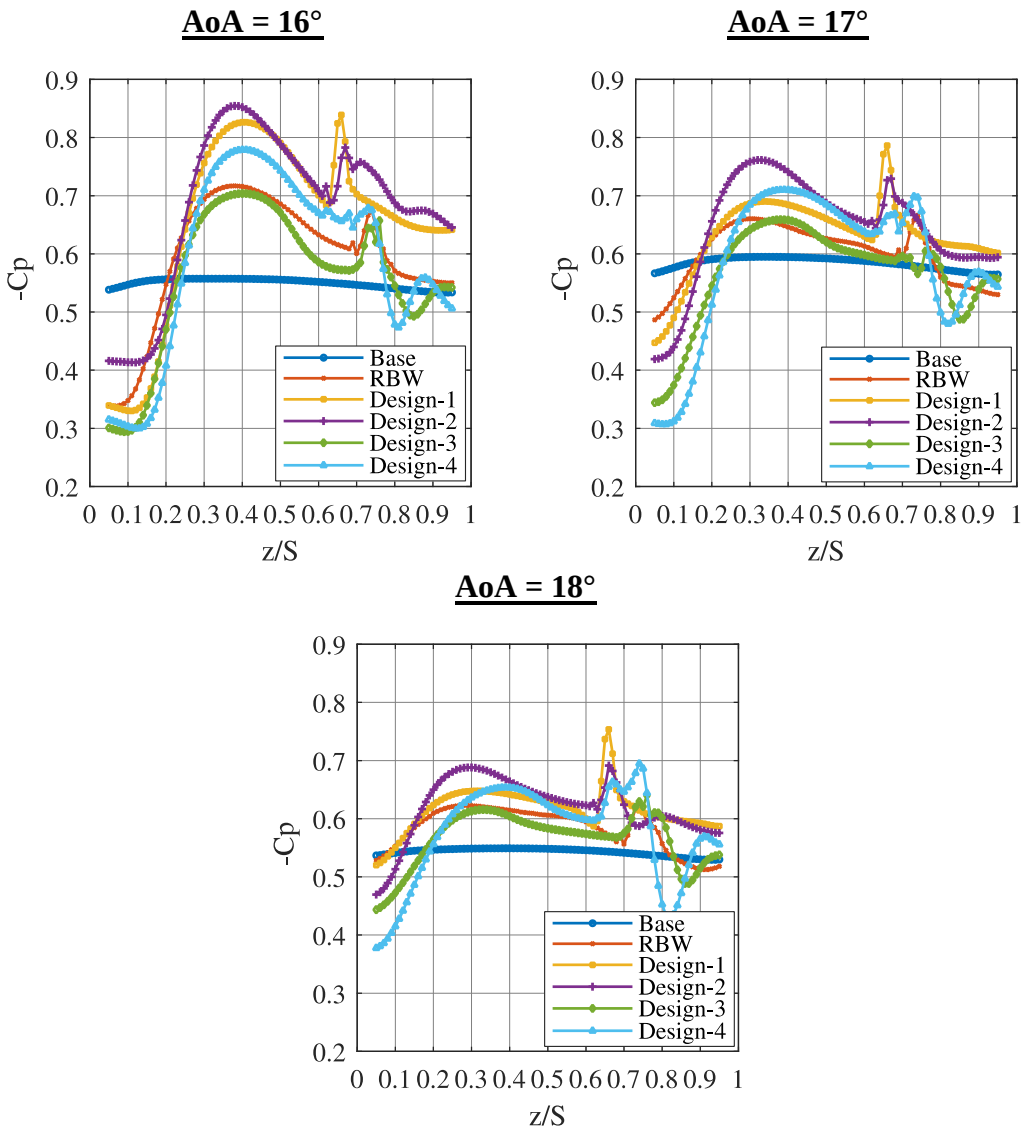

Figure 5-18. Comparison of -C_p Distribution of All Designs

Table 5-2. min/max -C_p Values

	Cases	$C_{p_{min}}$	$C_{p_{max}}$	$-\Delta C_p$
AoA = 16º	Base	0.53	0.56	0.02
	RBW	0.34	0.72	0.38
	Design-1	0.33	0.83	0.50
	Design-2	0.41	0.85	0.44
	Design-3	0.29	0.70	0.41
	Design-4	0.30	0.78	0.48
AoA = 17º	Base	0.56	0.59	0.03
	RBW	0.48	0.66	0.18
	Design-1	0.44	0.77	0.33
	Design-2	0.42	0.76	0.34
	Design-3	0.34	0.66	0.32
	Design-4	0.31	0.71	0.40
AoA = 18º	Base	0.54	0.55	0.01
	RBW	0.52	0.62	0.10
	Design-1	0.51	0.74	0.22
	Design-2	0.47	0.69	0.22
	Design-3	0.44	0.62	0.18
	Design-4	0.38	0.65	0.28

Another way to evaluate the wing performance is to compare the forces on the wing. At this point, drag and lift forces formed on the wing should be compared. Drag and lift forces are calculated using the following formula:

$$C_{l,}C_d = \frac{F}{\frac{1}{2}\rho U_\infty^2 A} \tag{5.1}$$

Here, F is the drag or the lift force; ρ is the density, U_∞ is the free stream velocity, and A is the top surface area of the base wing, which is considered to be the reference area for all calculations. In addition, holes opening ratio, HOR, calculated as follows. HOR is a value that expresses the size of the hole on the top surface of the wing. This is a parameter that must be taken into account when calculating the forces acting on the wing as the air flow transferred from the pressure side to the top surface increases with the increase in the size of the hole.

$$HOR = \frac{Total\ Hole\ Area}{Base\ Wing\ Suction\ Side\ Area} \quad (5.2)$$

In Table 5-3, the drag and lift forces, hole opening ratios and total air flow rates passing through the bleed holes of all cases are compared. When C_l/C_d values are compared, it is seen that Designs 1 and 2 exhibit the C_l/C_d highest. Lift forces generated by Designs 3 and 4 are lower than those of the other two designs. Higher flow rates through the bleeding holescause the wings to lose lift force. Despite the lower lift forces calculated in Designs 3 and 4, the ΔC_p values observed earlier show that the vortex lift contribution is higher in these designs. At this point, it can be said that the increase in HOR reduces the potential lift force of the wing, but increases the vortex lift contribution due to a stronger vortical structure. Vortex liftis known to increase with the increase of AoA. When the relationship between AoA and C_l is examined, it is seen that the lift force tends to decrease with the increase of AoA in Designs 1 and 2, and it does not change much with the increase of AoA in Designs 3 and 4. The main reason for this is that Design 4 is able to form a vortical structure in all AoAs examined. Thus, while the other designs lose the lift force with the increase of AoA, Design 4 is able to maintain the vortex lift.

Table 5-3. Comparison of drag/lift forces of all designs

	AoA	Drag Force [N]	C_d	Lift Force [N]	C_l	C_l/C_d	Q_{Holes} [m^3/s]*10^{-4}	HOR
Base Wing	16°	0.116	0.27	0.239	0.56	2.06	-	0
	17°	0.127	0.30	0.256	0.60	2.02	-	
	18°	0.130	0.30	0.238	0.55	1.83	-	
RBW	16°	0.126	0.29	0.260	0.60	2.07	7.17	0.0335
	17°	0.134	0.31	0.270	0.63	2.01	7.14	
	18°	0.139	0.32	0.262	0.61	1.88	7.12	
Design-1	16°	0.133	0.31	0.278	0.65	2.10	7.36	0.0335
	17°	0.135	0.31	0.273	0.63	2.02	7.23	
	18°	0.140	0.33	0.271	0.63	1.93	7.20	
Design-2	16°	0.134	0.31	0.285	0.66	2.13	9.69	0.0335
	17°	0.139	0.32	0.279	0.65	2.01	9.58	
	18°	0.142	0.33	0.274	0.64	1.93	9.43	
Design-3	16°	0.129	0.30	0.250	0.58	1.94	14.98	0.0396
	17°	0.131	0.30	0.253	0.59	1.93	15.20	
	18°	0.139	0.32	0.251	0.58	1.80	15.31	
Design-4	16°	0.133	0.31	0.260	0.60	1.95	15.79	0.0396
	17°	0.138	0.32	0.264	0.61	1.90	16.04	
	18°	0.143	0.33	0.263	0.61	1.83	16.04	

Finally, in Figure 5-19, the streamlines of Designs 1 and 4 are compared at 16° and 18° AoA. While Designs 1 and 4 show a similar character at 16° AoA, Design 1 does not have the ability to create a vortical structure when the angle of attack is increased to 18° and it is observed that the flow lines reach the symmetry axis of the wing and the features of 3D separation are started to be seen. However, in Design 4, the shift of the flow lines towards the wing centreline is less and the vortical structure is still preserved. This, as in all other findings, shows that Design 4 provides vortical structure even at higher angle of compared to other designs.

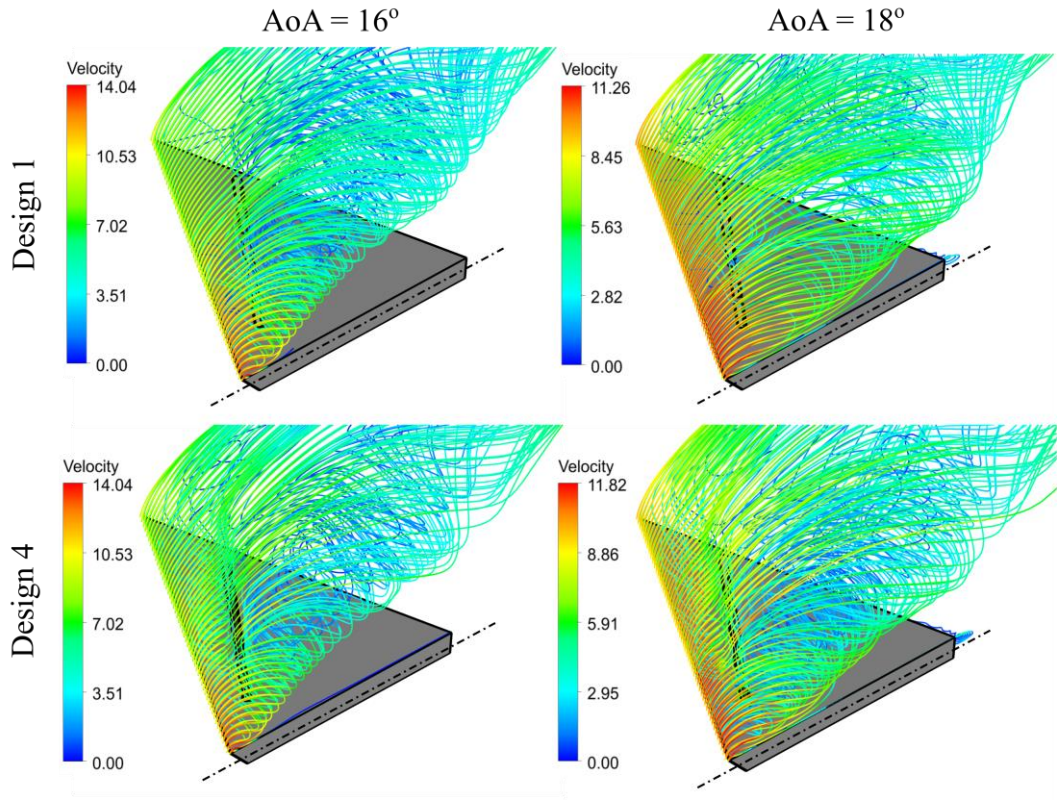

Figure 5-19. Comparison of 3D Streamlines

When visual and numerical results are evaluated, it is seen that the designs with 5 bleeding holes perform better in terms of lift force and rebuild the vortical structure at 16° AoA, but their performance degrades with increasing AoA. On the other hand, fully open designs show a more robust character and they are less sensitive to AoA changes. In evaluating a wing's performance, not only the generation of high lift force, but also the capability of maintaining the lift at high AoAs is important. Considering these results, although the total lift force is lower than other designs, it can be said that Design 4 has the highest performance and stability due to the fact that the vortical structure can be generated more strongly and the vortical lift contribution can also be provided at high AoAs.

CHAPTER 6

CONCLUSION

6.1. Summary and Conclusion

The flow around delta wings consists of complex vortex structures. They are formed as a result of the flow separation from the sharp leading edge. Leading edge vortices contribute to the lift force by creating a suction zone on the upper surface of the wing, however, this vortical structure may weaken, disappear or become unstable as the angle of attack increases. As this situation causes the vortex contributed lift to weaken or disappear, it adversely affects the performance of the wing and may even cause the wing to enter the stall regime. Delaying and controlling instabilities is possible through flow control methods. In this study, one of the passive flow control techniques known as bleeding is considered, whose potential was already demonstrated experimentally by Karagöz [18] and Çelik [19] and the effects of changes in the position, size and orientation of the bleed holes are examined in detail.

A non-slender delta wing with 45° sweep angle is examined numerically using ANSYS Fluent software. First, the optimal mesh generation model is determined and then the mesh independence study is performed. As a result, the mesh consisting of approximately 9.5 M (for base wing) – 11 M (for bleeding wings) polyhedral elements is selected for the simulations to be made. In the simulations, the $k-\omega$ SST Curvature Correction turbulence model is used. In the validation of the simulation model, the results are compared with the experimental results of Karagöz [18] and Çelik [19].

After validating the model, flows over wings with four different bleed hole designs, some of which are novel, are simulated. The first of the designs examined is a 5-hole bleeding wing with the newly introduced yaw angle between the bleeding holes and the leading edge. In the second design, the holes are brought closer to the apex of the

wing by changing the back angle gradually from the apex to the trailing edge. In the third design, the holes are combined into a single one, and finally in the fourth design, the yaw angle modification is used for the single hole case.

According to the results of the study, the following conclusions can be reached:

- In the comparisons made in the validation study, it is seen that the simulation model is able to capture the vortical structure around the wing and the effects of the bleeding application. However, deviations from the experiments are also observed. Surface pressures calculated at high angles of attack showed differences up to 25%. The deviations are attributed to the use of RANS turbulence modeling.
- At 16° AoA, all designs are able to recreate the vortical structure. Designs 1 and 2 show higher performance than others and are the designs where the vortex core is farthest away from the wing's symmetry axis, with the strongest vortical structure. Although Design 4 has a flow character that is very close to Design 1, it stays slightly behind Design 1 in terms of lift force and vortex structure strength. And Design 3 achieves almost the same performance as the reference bleeding wing and is not as successful as other designs.
- At higher AoA (17° and 18°) simulations of Design 1 and Design 2, it is observed that the vortex core approaches the wing's symmetry axis and the reattachment weakens. This shows that these designs lose the ability to form a strong vortical structure at higher AoAs. In particular, it is seen that the results of Design 1 become similar to the reference bleeding wing results with the increase of AoA. This shows that the 5-hole designs begin to lose flow control capability with an increase in angle of attack. However, fully open Design 3 and Design 4 are more resistant to increased angle of attack. Especially Design 4 is able to create a stronger vortical structure at higher AoAs compared to all other designs and it displays a more robust character.
- The strength of the vortical structure is naturally examined by comparing ΔC_p values. In this examination at 16 AoA, Design 1 creates the most powerful

vortical structure and Design 4 performs close to Design 1. However, at higher AoA, Design 4 can create vortical structure more powerful compared to all other designs.

- 5-hole designs have higher lift force compared to fully open designs. This is associated to the increased hole opening ratio of single hole designs. However, fully open hole designs are able to maintain vortical lift force contribution at higher AoAs.
- Overall, it is observed that the passive bleeding flow control method is highly sensitive to hole sizes, placement and orientation. The newly introduced yaw angle is found to be effective in regaining the desired vortical structure. On the other hand, the increase in the size of the bleeding holes is found to be effective in making the designs robust by decreasing the sensitivity to AoA.

6.2. Future Work

The current study can be improved and extended in the following ways.

- The yaw angle applied in Designs 1, 2 and 4 is determined based on the reference bleeding wing results by roughly estimating the value of the angle that would be the most effective. In this study, simulations are performed with a single yaw angle and the potential of this design is demonstrated. A further study can be performed with different yaw angles to examine its effect.
- The study is carried out at 75000 Reynolds number. The sensitivity of the designs to the Reynolds number can be examined.
- The hole opening ratio is increased by joining the 5 holes longitudinally. The effect of the increase in hole size can also be examined by enlarging them in the transverse direction.
- Advanced turbulence models such as DES and LES can be used to see especially their effect on the surface pressure results.

- The performance of the designs can be examined for delta wings with other sweep angles.
- Three different high angles of attack close to each other are examined. The main reason for the examination at high AoAs and in a narrow range is to create design alternatives to the reference bleeding wing, which begins to lose its effect at these angles. After seeing the performance of different design is this study, desired ones can be studied in a broader AoA range.

REFERENCES

[1] Earnshaw, P. B., and Lawford, J. A., 1964, "Low-Speed Wind-Tunnel Experiments on a Series of Sharp-Edged Delta Wings," Minist. Aviat. Aeronaut. Res. Counc. Reports Memo. 3424, (3424).

[2] Gursul, I., Wang, Z., and Vardaki, E., 2007, "Review of Flow Control Mechanisms of Leading-Edge Vortices," Prog. Aerosp. Sci., **43**(7–8), pp. 246–270.

[3] Pirzadeh, S. Z., 2001, "Vortical Flow Prediction Using an Adaptive Unstructured Grid Method," RTO AVT Symp. Adv. Flow Manag., **Part A** – **V**.

[4] Gursul, I., Gordnier, R., and Visbal, M., 2005, "Unsteady Aerodynamics of Nonslender Delta Wings," Prog. Aerosp. Sci., **41**(7), pp. 515–557.

[5] Gursul, I., and Xie, W., 1999, "Buffeting Flows over DeltaWings," **37**(1).

[6] Taylor, G. S., and Gursul, I., 2004, "Buffeting Flows over a Low-Sweep Delta Wing," AIAA J., **42**(9), pp. 1737–1745.

[7] Taylor, G. S., Schnorbus, T., and Gursul, I., 2003, "An Investigation of Vortex Flows Over Low Sweep Delta Wings," 33rd AIAA Fluid Dyn. Conf. Exhib., (June), pp. 1–13.

[8] Yaniktepe, B., and Rockwell, D., 2004, "Flow Structure on a Delta Wing of Low Sweep Angle," AIAA J., **42**(3), pp. 513–523.

[9] Wang, J. J., and Zhang, W., 2008, "Experimental Investigations on Leading-Edge Vortex Structures for Flow over Non-Slender Delta Wings," Chinese Phys. Lett., **25**(7), pp. 2550–2553.

[10] Ol, M. V., and Gharib, M., 2003, "Leading-Edge Vortex Structure of Nonslender Delta Wings at Low Reynolds Number," AIAA J., **41**(1), pp. 16–26.

[11] Gursul, I., and Xie, W., 1999, "Origin of Vortex Wandering over Delta Wings," J. Aircr., **37**(2), pp. 348–350.

[12] POLHAMUS, E. C., 1971, "Predictions of Vortex-Lift Characteristics by a Leading- Edge Suction Analogy," J. Aircr., **8**(4), pp. 193–199.

[13] PAYNE, F. M., NG, T., NELSON, R. C., and SCHIFF, L. B., 1988, "Visualization and Wake Surveys of Vortical Flow over a Delta Wing," AIAA J., **26**(2), pp. 137–143.

[14] Lowson, M. V., and Riley, A. J., 1995, "Vortex Breakdown Control by Delta Wing Geometry," J. Aircr., **32**(4), pp. 832–838.

[15] Yavuz, M. M., Elkhoury, M., and Rockwell, D., 2004, "Near-Surface Topology and Flow Structure on a Delta Wing," AIAA J., **42**(2), pp. 332–340.

[16] Nelson, R. C., and Pelletier, A., 2003, "The Unsteady Aerodynamics of Slender Wings and Aircraft Undergoing Large Amplitude Maneuvers," Prog. Aerosp. Sci., **39**(2–3), pp. 185–248.

[17] Gursul, I., 2003, "Review of Unsteady Vortex Flows over Slender Delta Wings," J. Aircr., **42**(2), pp. 299–319.

[18] Karagoz, B., 2017, "Control Of Flow Structure On 45 Degree Swept Delta Wing Using Passive Bleeding, MSc Thesis," METU.

[19] Çelik, A., 2017, "Development and Implementation of Novel Flow Control Techniques for Nonslender Delta Wings," METU.

[20] Verhaagen, N. G., 2012, "Leading-Edge Radius Effects on Aerodynamic Characteristics of 50-Degree Delta Wings," J. Aircr., **49**(2), pp. 521–531.

[21] Yaniktepe, B., and Rockwell, D., 2008, "Flow Structure on Diamond and Lambda Planforms: Trailing-Edge Region," AIAA J., **43**(7), pp. 1490–1500.

[22] Yayla, S., Canpolat, C., Sahin, B., and Akilli, H., 2013, "The Effect of Angle of Attack on the Flow Structure over the Nonslender Lambda Wing," Aerosp. Sci. Technol., **28**(1), pp. 417–430.

[23] Greenwell, D. I., 2010, "Gurney Flaps on Slender and Nonslender Delta Wings," J. Aircr., **47**(2), pp. 675–681.

[24] Cai, J., Pan, S., Li, W., and Zhang, Z., 2014, "Numerical and Experimental Investigations of a Nonslender Delta Wing with Leading-Edge Vortex Flap," Comput. Fluids, **99**, pp. 1–17.

[25] Taylor, G., Wang, Z., Vardaki, E., and Gursul, I., 2007, "Lift Enhancement over Flexible Nonslender Delta Wings," AIAA J., **45**(12), pp. 2979–2993.

[26] Wang, Z.-J., Jiang, P., and Gursul, I., 2007, "Effect of Thrust-Vectoring Jets on Delta Wing Aerodynamics," J. Aircr., **44**(6), pp. 1877–1888.

[27] Mccormick, S., and Gursulf, I., 1996, "Effect of Shear-Layer Control on Leading-Edge Vortices," J. Aircr., **33**(6).

[28] Şençan, G., 2016, "Effect of Wing Heating on Flow Structure of Low Swept Delta Wing, MSc Thesis," METU.

[29] Kestel, K., 2019, "Effect Of Bleed Opening Ratio On Flow Structure Of A Nonslender Delta Wing," METU.

[30] 1931, “New Triangle Plane Is Tailless,” Pop. Sci., p. 65.

[31] Rizzi, A., and Eriksson, L, E., 1982, “Computations of Vortex Flow around Wings Using the Euler Equations.Pdf,” Notes Numer. Fluid Mech., **5**, pp. 87–105.

[32] Rizzi, A., and Eriksson, Lars, E., 1984, “Computation of Flow around Wings Based on the Euler Equations,” J. ofFluid Mech., **148**, pp. 45–71.

[33] Rizzi, A., Eriksson, Lars, E., Schmidt, W., and Hitzel, S., 1983, “Numerical Solutions of the Euler Equations Simulating Vortex Flows around Wings,” AGARD CP-342, Aerodyn. Vor. Type Flows Three Dimens.

[34] Rizzi, A., and Purcell, C. J., 1987, “On the Computation of Transonic Leading-Edge Vortices Using the Euler Equations,” J. Fluid Mech., **181**, pp. 163–195.

[35] Eriksson, L. E., 1985, “Computation of Inviscid Incompressible Flow with Rotation,” J. Fluid Mech., **153**, pp. 275–312.

[36] Scherr, S., and Das, A., 1988, “Basic Analysis of the Flow Fields of Slender Delta Wings Using the Euler Equations.Pdf,” AIAA J.

[37] Fujii, K., and Schiff, L. B., 1989, “Numerical Simulation of Vortical Flows over a Strake-Delta Wing,” AIAA J., **27**(9), pp. 1153–1162.

[38] Visbal, M. R., 1996, “Computed Unsteady Structure of Spiral Vortex Breakdown on Delta Wings,” 1996 Fluid Dyn. Conf., (June), pp. 1–31.

[39] Visbal, M. R., and Gaitonde, D. V., 1999, “High-Order-Accurate Methods for Complex Unsteady Subsonic Flows,” AIAA J., **37**(10), pp. 1231–1239.

[40] Müller, J., and Hummel, D., 2000, “Numerical Analysis of the Unsteady Flow Above a Slender Delta Wing At Large Angles of Attack,” pp. 1–12.

[41] Son, M. S., Sa, J. H., Park, S. H., Byun, Y. H., and Cho, K. W., 2015, “Delayed Detached-Eddy Simulation of Vortex Breakdown over a 70° Delta Wing,” J. Mech. Sci. Technol., **29**(8), pp. 3205–3213.

[42] Cummings, R. M., and Schütte, A., 2012, “Detached-Eddy Simulation of the Vortical Flow Field about the VFE-2 Delta Wing,” Aerosp. Sci. Technol., **24**(1), pp. 66–76.

[43] Vlahostergios, Z., Komnos, D., and Yakinthos, K., 2018, “Modelling of Vortex Breakdown and Calculation of Large-Scale Kinetic Energy on a Slender Delta Wing Using URANS and Reynolds-Stress Modelling,” Prog. Comput. Fluid Dyn. An Int. J., **18**(6), p. 347.

[44] Chen, L., and Wang, J., 2009, “Numerical Simulations of Leading-Edge Vortex Core Axial Velocity for Flow over Delta Wings,” Sci. China, Ser. E Technol. Sci., **52**(7), pp. 2029–2036.

[45] Cooper, J. M., and Girimaji, S. S., 2015, “Progress in Hybrid RANS-LES Modelling,” **117**, pp. 445–455.

[46] Schiavetta, L., Badcock, K., and Cummings, R., 2007, “Comparison of DES and URANS for Unsteady Vortical Flows over Delta Wings,” AIAA J., (January).

[47] Gortz, S., 2005, “Realistic Simulations of Delta Wing Aerodynamics Using Novel CFD Methods,” Royal Institute of Technology.

[48] Mitchell, A. M., Morton, S. A., Forsythe, J. R., and Cummings, R. M., 2006, “Analysis of Delta-Wing Vortical Substructures Using Detached-Eddy Simulation,” AIAA J., **44**(5), pp. 964–972.

[49] Küçükyılmaz, İ, C., 2016, “Control Of Flow Structure On 70° Swept Delta Wing With Along-The-Core Blowing Using Numerical Modeling, MSc Thesis,” METU.

[50] Sayılır, S. E., 2018, “Control of Flow Structure on Vfe-2 Delta Wing with Passive Bleeding Using CFD, MSc Thesis,” METU.

[51] Jo, Y. H., Chang, K., Sheen, D. J., and Park, S. H., 2015, “Numerical Simulation of Aerodynamic Characteristics of a BWB UCAV Configuration with Transition Models,” Int. J. Aeronaut. Sp. Sci., **16**(1), pp. 8–18.

[52] Huang, X. Z., Mébarki, Y., Benmeddour, A., and Brown, T., 2004, “Experimental and Numerical Studies of Geometry Effects on UCAV’s Aerodynamics,” AIAA Pap., (January), pp. 403–418.

[53] Hsu, C. H., and Liu, C. H., 1988, “Navier-Stokes Computation of Flow around a Round-Edged Double-Delta Wing,” AIAA 6th Appl. Aerodyn. Conf. 1988, **28**(6), pp. 665–673.

[54] Hamizi, I. B., and Khan, S. A., 2019, “Aerodynamics Investigation of Delta Wing at Low Reynold’s Number,” CFD Lett., **11**(2), pp. 32–41.

[55] Schütte, A., Einarsson, G., Raichle, A., BrittaSchöning, Mönnich, W., Orlt, M., Neumann, J., Arnold, J., and Forkert, T., 2009, “Numerical Simulation of Maneuvering Aircraft by Aerodynamic, Flight-Mechanics, and Structural-Mechanics Coupling,” J. Aircr., **46**(1), pp. 53–64.

[56] Qu, Q., Lu, Z., Liu, P., and Agarwal, R. K., 2014, “Numerical Study of Aerodynamics of a Wing-in-Ground-Effect Craft,” J. Aircr., **51**(3), pp. 913–924.

[57] Liu, W., Zhang, H., and Zhao, H., 2005, “Numerical Simulation and Physical Characteristics Analysis for Slender Wing Rock,” Collect. Tech. Pap. - AIAA Appl. Aerodyn. Conf., **1**(June), pp. 266–272.

[58] Cai, J., Tsai, H. M., Luo, S., and Liu, F., 2008, “Stability of Vortex Pairs over

Slender Conical Bodies: Analysis and Numerical Computation," AIAA J., **46**(3), pp. 712–722.

[59] Schiavetta, L. A., Boelens, O. J., and Fritz, W., 2006, "Analysis of Transonic Flow on a Slender Delta Wing Using CFD," Collect. Tech. Pap. - AIAA Appl. Aerodyn. Conf., **2**(June), pp. 995–1016.

[60] Schütte, A., and Lüdeke, H., 2013, "Numerical Investigations on the VFE-2 65-Degree Rounded Leading Edge Delta Wing Using the Unstructured DLR TAU-Code," Aerosp. Sci. Technol., **24**(1), pp. 56–65.

[61] Allan, M. R., Badcock, K. J., Barakos, G. N., and Richards, B. E., 2005, "Wind-Tunnel Interference Effects on Delta Wing Aerodynamics Computational Fluid Dynamics Investigation," J. Aircr., **42**(1), pp. 189–198.

[62] Cummings, R. M., Forsythe, J. R., Morton, S. A., and Squires, K. D., 2003, "Computational Challenges in High Angle of Attack Flow Prediction," Prog. Aerosp. Sci., **39**(5), pp. 369–384.

[63] Lv, M., Fang, S., and Zhang, Y., 2015, "Numerical Simulation of Unsteady Separated Flow over a Delta Wing Using Cartesian Grids and DES/DDES," Procedia Eng., **99**, pp. 423–427.

[64] Morton, S. a, Forsythe, J. R., Mitchell, A. M., and Hajek, D., 2002, "DES And RANS Simulations Of Delta Wing Vortical Flows 40 Th Aerospace Sciences Meeting & Exhibit Reno , Nevada," Simulation, (c).

[65] Buzica, A., Biswanger, M., and Breitsamter, C., 2018, "Detached Eddy-Simulation of Delta-Wing Post-Stall Flow Control," Transp. Res. Procedia, **29**, pp. 46–57.

[66] Crippa, S., and Rizzi, A., 2006, "Numerical Investigation of Reynolds Number Effects on a Blunt Leading-Edge Delta Wing," Test, (June), pp. 1–19.

[67] Qin, Y., Qu, Q., Liu, P., Tian, Y., and Lu, Z., 2015, "DDES Study of the Aerodynamic Forces and Flow Physics of a Delta Wing in Static Ground Effect," Aerosp. Sci. Technol., **43**, pp. 423–436.

[68] M.R.Allan, 2003, "A CFD Investigation of Wind Tunnel Interference on Delta Wing Aerodynamics," Aiaa-2003-4214, p. 219.

[69] Gursul, I., and Wang, Z., 2018, "Flow Control of Tip/Edge Vortices," AIAA J., (1), pp. 1–19.

[70] MAGNESS, C., ROBINSON, O., and ROCKWELL, D., 1993, "Control of Vortices on a Delta Wing by Leading-Edge Injection," AIAA J., **31**(7).

[71] WOOD, N. J., ROBERTS, L., and CELIK, Z., 1990, "Control of Asymmetric Vortical Flows over Delta Wings at High Anglesof Attack," J. Aircr., **27**(5), pp. 429–435.

[72] Greenwell, D. I., and Wood, N. J., 1994, “Roll Moment Characteristics of Asymmetric Tangential Leading-Edge Blowing on a Delta Wing,” J. Aircr., **31**(1), pp. 161–168.

[73] Ferman, M. A., Huttsell, L. J., and Turner, E. W., 2004, “Experiments with Tangential Blowing to Reduce Buffet Response on an F-15 Model,” J. Aircr., **41**(4), pp. 903–910.

[74] Williams, N. M., Wang, Z., and Gursul, I., 2008, “Active Flow Control on a Nonslender Delta Wing,” J. Aircr., **45**(6), pp. 2100–2110.

[75] Kölzsch, A., and Breitsamter, C., 2014, “Vortex-Flow Manipulation on a Generic Delta-Wing Configuration,” J. Aircr., **51**(5), pp. 1380–1390.

[76] Vorobieff, P. V., and Rockwell, D. O., 1998, “Vortex Breakdown on a Pitching Delta Wing - Control by Intermittent Trailing-Edge Blowing,” AIAA J., **36**(4), pp. 585–589.

[77] Yavuz, M. M., and Rockwell, D., 2006, “Control of Flow Structure on Delta Wing with Steady Trailing-Edge Blow,” AIAA J., **44**(3), pp. 493–501.

[78] Jiang, P., Wang, Z., and Gursul, I., 2010, “Effects of Unsteady Trailing-Edge Blowing on Delta Wing Aerodynamics,” J. Aircr., **47**(2), pp. 591–602.

[79] Johari, H., Olinger, D. J., and Fitzpatrick, K. C., 1995, “Delta Wing Vortex Control via Recessed Angled Spanwise Blowing,” J. Aircr., **32**(4), pp. 804–810.

[80] Sreenatha, A. G., and Ong, T. K., 2002, “Wing Rock Suppression Using Recessed Angle Spanwise Blowing,” J. Aircr., **39**(5), pp. 900–903.

[81] Johari, H., and Moreira, J., 1996, “Delta Wing Vortex Manipulation Using Pulsed and Steady Blowing during Ramp-Pitching,” J. Aircr., **33**(2), pp. 304–310.

[82] Kuo, C.-H., and Lu, N.-Y., 1998, “Unsteady Vortex Structure over Delta-Wing Subject to Transient along-Core Blowing,” AIAA J., **36**(9), pp. 1658–1664.

[83] Vlahostergios, Z., Missirlis, D., Yakinthos, K., and Goulas, A., 2013, “Computational Modeling of Vortex Breakdown Control on a Delta Wing,” Int. J. Heat Fluid Flow, **39**, pp. 64–77.

[84] Kyriakou, M., Missirlis, D., and Yakinthos Kyros, K., 2010, “Numerical Modeling of the Vortex Breakdown Phenomenon on a Delta Wing with Trailing-Edge Jet-Flap,” Int. J. Heat Fluid Flow, **31**(6), pp. 1087–1095.

[85] Guy, Y., Morrov, J, A., and McLaughlin, T., 1999, “Control of Vortex Breakdown on a Delta Wing by Periodic Blowing and Suction,” AIAA J., (c).

[86] Guy, Y., Morrow, J., and McLaughlin, T., 1999, “Pressure Measurements and

Flow Field Visualization on a Delta Wing with Periodic Blowing and Suction," (c).

[87] Gad-El-Hak, M., and Blackwelder, R. F., 1987, "Control of the Discrete Vortices from a Delta Wing," AIAA J., **25**(8), pp. 1042–1049.

[88] Zharfa, M., 2015, "Control of Flow Structure on Low Swept Delta Wing With Steady Leading Edge Blowing, MSc Thesis," METU.

[89] Yavuz, M. M., and Rockwell, D., 2006, "Identification and Control of Three-Dimensional Separation on Low Swept Delta Wing," AIAA J., **44**(11), pp. 2805–2811.

[90] Sibilski, K., Żyluk, A., and Wróblewski, W., 2018, "Experimental Studies of Leading Edge Vortex Control of Delta Wing Micro Aerial Vehicle," J. KONES, **25**(3), pp. 393–402.

[91] Shen, L., and Wen, C., 2016, "Fedsm2016-7532 Leading Edge Vortex Control on a Delta Wing With Dielectric," pp. 1–8.

[92] Deng, Q., and Gursul, I., 1996, "Effect of Leading-Edge Flaps on Vortices and Vortex Breakdown," J. Aircr., **33**(6), pp. 1079–1086.

[93] Mitchell, A. M., and Délery, J., 2001, "Research into Vortex Breakdown Control," Prog. Aerosp. Sci., **37**(4), pp. 385–418.

[94] Lee, T., and Ko, L. S., 2017, "Aerodynamics and Vortex Flowfield of a Slender Delta Wing With Apex Flap and Tip Flap," J. Fluids Eng., **139**(5), p. 051106.

[95] Tormalm, M., Le Roy, J.-F., and Morgand, S., 2016, "Numerical Assessment of Leading- and Trailing-Edge Control on a Swept Lambda Wing," J. Aircr., **55**(2), pp. 603–622.

[96] Hitzel, S., and Zimper, D., 2016, "Wind Tunnel, Simulation, and 'Real' Flight of Advanced Combat Aircraft: Industrial Perspective," J. Aircr., **55**(2), pp. 587–602.

[97] Lofthouse, A. J., and Cotton, K., 2017, "Computational Simulation of a Generic UCAV Configuration with Moveable Control Surfaces," (June), pp. 1–24.

[98] Schütte, A., Huber, K. C., Frink, N. T., and Boelens, O. J., 2016, "Stability and Control Investigations of Generic 53 Degree Swept Wing with Control Surfaces," J. Aircr., **55**(2), pp. 502–533.

[99] Ali, U., and Chadwick, E., 2016, "Flow Control and High-Lift Performance for Flying-Wing Unmanned Combat Air Vehicle Configurations by Inserting Slots," Int. J. Multiphys., **10**(2).

[100] Vardaki, E., Gursul, I., and Taylor, G., 2005, "Physical Mechanisms of Lift Enhancement for Flexible Delta Wings," (January), pp. 1–13.

[101] Lachmann, G., 1924, “Results of Experiments with Slotted Wings,” NACA TM 282.

[102] Hunter, C., Viken, S., Wood, R., and Bauer, S., 2001, “Advanced Aerodynamic Design of Passive Porosity Control Effectors,” AIAA Pap., (January).

[103] Carpenter, P. W., and Porter, L. J., 2001, “Effects of Passive Porous Walls on Boundary-Layer Instability,” AIAA J., **39**(4), pp. 597–604.

[104] Kearney, J., and Glezer, A., 2012, “Aerodynamic Control Using Distributed Bleed,” (June), pp. 1–17.

[105] Ramazanl, B., Kestel, K., Do, O., Bu, Z. E. T., Ara, H., and Ara, M. H., 2018, “Düşük Ve Orta Ok Açili Delta Kanatlar Üzerindeki Akişin Pasif,” UHUK, pp. 1–9.

[106] Çelik, A., Çetin, C., and Yavuz, M. M., 2016, “Düşük Ok Açili Delta Kanat Üzerindeki Akişin Pasif Akitma Yöntemiyle,” UHUK, pp. 1–7.